

Localization of Surgical Instruments in 3D Ultrasound Images

Doctoral Thesis under Co-supervision

CTU–CMP–2007–12

presented on the 30th of August 2007 in Lyon to

the Czech Technical University in Prague in partial fulfillment of the requirements for the Ph.D. degree in Study Programme No. P 2612—Electrical Engineering and Information Technology, branch No. 3902V035—Artificial Intelligence and Biocybernetics

and to

the University of Claude Bernard Lyon 1 in partial fulfillment of the requirements for the degree Docteur de l'Université Claude Bernard Lyon 1,

by

Ing. Martin BARVA

Panel:

Advisor	M. Christian CACHARD	Professor, Université Claude Bernard Lyon 1
Advisor	M. Václav HLAVÁČ	Professor, Czech Technical University
Advisor	M. Jan KYBIC	Research Assistant, Czech Technical University
Reviewer	M. Pascal HAIGRON	Associate Professor, Université de Rennes 1
Reviewer	M. Petr POLLÁK	Associate Professor, Czech Technical University
Reviewer	M. Jean SEQUEIRA	Professor, Université de la Méditerranée
	M. Petr BERKA	Professor, Prague School of Economics
	M. Cyril LAFON	Associate Professor, INSERM U556
	M. Vladimír MAŘÍK	Professor, Czech Technical University
	M. Petr VAVŘÍN	Professor, Brno University of Technology

Abstract

The medical interventions involving surgical instruments are frequently combined with ultrasound based imaging systems to safely navigate instruments into a pre-defined place inside the body. To facilitate visual tracking of the instrument in acquired images, we propose robust techniques that automatically determine the position of an electrode-like object in a 3D ultrasound image.

The task is decomposed into the localization of the electrode axis and the detection of its tip. We show that the axis can be found by maximizing the parallel projection which we describe by a Parallel Integral Projection transform. The maximization is accelerated by a hierarchical mesh-grid method. A second algorithm based on the model fitting paradigm is introduced to identify the axis of a curved electrode. Three distinct models are suggested to describe the geometrical shape and the prior information about the intensity distribution. Their parameters are robustly estimated by the R-RANSAC algorithm. The electrode position is optimized using the simplex method. The electrode tip is detected by analyzing the intensity along the axis with a priori calculated parameters.

3D ultrasound images were simulated to test the influence of various conditions such as the electrode orientation, depth of penetration, curvature and the effect of changing the signal-to-noise ratio on the localization accuracy. The algorithms were also experimentally verified on real ultrasound images acquired by a 3D scanner scanning a portion of a cryogel phantom that contained a thin metallic electrode. The experiments show that the algorithms are capable of detecting a curved electrode with the accuracy of 0.2 mm. The computational time of the order of seconds permits fast electrode localization.

Résumé (Abstract in French)

Des interventions médicales qui utilisent des outils chirurgicaux sont souvent accompagnées par des systèmes d'imagerie échographiques pour guider l'outil dans un endroit préfixe à l'intérieur du corps. Afin de faciliter la tâche de localisation de l'outil dans des images acquises, on propose des approches nouvelles pour trouver la position d'un objet de la forme d'électrode dans une image échographique 3D.

Le problème est décomposé à la localisation de l'axe et à la détection de l'extrémité de l'électrode. On montre que l'axe d'une électrode droite peut être estimé par une maximisation de la projection parallèle que l'on décrit par une transformée de la Projection Intégrale Parallèle. La maximisation est accélérée par une approche multi-échelle, hiérarchique. Deuxième algorithme basé sur le recalage de modèle permet d'identifier l'axe d'une électrode courbée. Trois modèles différents décrivent la forme géométrique de l'électrode et la densité d'intensité. Ses paramètres sont établis par l'estimateur R-RANSAC. La position de l'électrode est optimisée par la méthode simplex. L'extrémité de l'électrode est cherchée par une analyse des intensités le long de l'axe dont les paramètres ont été calculés a priori.

Des images échographiques 3D ont été simulées pour vérifier l'influence des conditions différentes telles que l'orientation de l'électrode, la profondeur d'insertion, la courbure et le rapport signal-bruit, sur la précision de la localisation. Les méthodes ont été testées sur des images acquises par un échographe 3D qui scannait un morceau de fantôme comprenant une électrode. Les résultats montrent que les algorithmes sont capables de localiser une électrode courbée avec une précision de 0.2 mm. Le temps de calcul de l'ordre de seconds permet une localisation rapide.

Resumé (Abstract in Czech)

Během lékařských zákroků, při kterých je do těla zaváděn miniaturní chirurgický nástroj, jsou často používány ultrazvukové zobrazovací metody, které usnadňují umístění tohoto nástroje do předem stanoveného místa. S cílem usnadnit vizuální identifikaci nástroje v získaných intra-operativních snímcích, byly navrženy a otestovány robustní algoritmy, které umožňují automaticky určit pozici objektu ve tvaru elektrody ve 3D ultrazvukovém snímku.

Lokalizace elektrody se skládá z identifikace osy a nalezení hrotu. První z metod používá pro určení pozice osy maximalizaci paralelní projekce, kterou jsme formalizovali pomocí tzv. transformace Paralelní Integrovaní Projekce (PIP). Nalezení maxima PIP transformace je zrychleno pomocí sekvence mřížek s hierarchicky uspořádaným rozlišením. Druhý algoritmus, založený na odhadu parametrů modelu, umožňuje identifikaci osy zakřivené elektrody. V této práci popisujeme tři různé modely popisující geometrický tvar elektrody a distribuci intenzit. Parametry těchto modelů jsou hledány pomocí R-RANSAC estimátoru a na závěr optimalizovány Nelder-Mead simplexovou metodou. Hrot elektrody je určen z intenzity podél odhadnuté osy.

V experimentální části jsme nasimulovali 3D ultrazvukové snímky, které sloužili k otestování chování navržených algoritmů v různých konfiguracích, např. různá orientace elektrody, délka elektrody, zakřivení elektrody, poměr signálu k šumu snímku. Metody byly také testovány na reálných ultrazvukových datech, které byly získány 3D ultrazvukovým přístrojem snímající fantom s akustickými vlastnostmi měkké tkáně, ve kterém byla umístěna tenká kovová elektroda. Výsledky ukazují, že dané algoritmy jsou schopny nalézt zakřivenou osu s přesností až 0.2 mm. Rychlost zpracování dat, která se pohybuje v řádu sekund, umožňuje lokalizovat elektrodu téměř v reálném čase.

Acknowledgments

I am grateful to a number of people and organizations that helped me to pursue this research. First and foremost, my profound thanks and appreciation are addressed to my advisor Dr. Jan Kybic for his encouragement, help and kind support. His invaluable technical and editorial advice, discussions and guidance were a real support to complete this work.

I would like to thank Prof. Václav Hlaváč, the head of the Center for Machine Perception, who was actively interested in my work. Prof. Hlaváč's skills and uncompromising quest for excellence create in CMP an inspiring working atmosphere. His numerous comments and suggestions significantly improved the readability of the manuscript.

My sincere thanks belong to Prof. Christian Cachard from the french research center CREATIS in Lyon, who was my advisor in France. His extensive knowledge and patient guidance helped me to quickly gain insight into the domain of ultrasound imaging, which contributed to the quality of the work.

The research presented in this thesis was supported by the French Embassy in the Czech Republic under the project of doctoral studies under co-supervision (doctorat en cotutelle), by the Czech Ministry of Education under project 1M0567 and by the Grant Agency of the Czech Academy of Sciences under project 1ET101050403.

Contents

1	Introduction	1
2	Problem description	5
2.1	Motivation	5
2.2	Problem formulation	6
2.3	Issues specific to processing ultrasound data	8
3	Technical Background	9
3.1	Ultrasound imaging	9
3.1.1	Sound propagation in medium	10
3.1.2	Imaging instrumentation	15
3.1.3	Pulse-echo imaging	18
3.1.4	Image formation	20
3.1.5	Spatial resolution of the ultrasound system	24
3.2	FIELD II	25
3.2.1	Simulation of RF signal	26
3.2.2	Transducer settings	26
3.2.3	Phantom definition	26
3.3	Estimator RANSAC	28
3.3.1	Randomized RANSAC	29

4	State of the art	33
4.1	Methods modeling ultrasound physics	33
4.1.1	Radio-frequency data	34
4.1.2	Envelope data	34
4.1.3	Log-compressed images	35
4.2	Features and priors in object detection	35
4.2.1	Edge features	36
4.2.2	Shape priors	36
4.2.3	Temporal priors	37
4.3	Existing electrode localization techniques	37
4.3.1	PCA applied to a 2D variance image	37
4.3.2	PCA applied to a 3D image	39
4.3.3	Minimization of parallel image projections	40
4.3.4	Segmentation in two orthogonal image projections	41
4.3.5	Superquadric fitting with RANSAC	41
5	Description of input data	45
5.1	Region of interest	45
5.2	Assumptions	45
5.3	Decomposition of the localization task	48
6	Axis localization with PIP transform	49
6.1	Parallel Integral Projection transform	49
6.2	Discretization of the PIP transformation	50
6.3	Maximizing the PIP transformation	51
6.3.1	Exhaustive search	53
6.3.2	Hierarchical mesh-grid search	54

6.3.3	Comparison of the exhaustive and the hierarchical search . .	55
6.4	Discretization parameters vs. accuracy	57
6.4.1	Influence of the final angular steps $\Delta_{\alpha}^{final}, \Delta_{\beta}^{final}$	58
6.4.2	Influence of the displacement steps Δ_u, Δ_v	58
7	Axis localization with model fitting	63
7.1	Segmentation	63
7.1.1	Estimating optimal threshold T_I	64
7.2	Shape and intensity models of the electrode	66
7.2.1	Model I – Axis shape	67
7.2.2	Model II – Axis shape and intensity priors	71
7.2.3	Model III – Axis shape and intensity profile	74
7.3	Estimating model with R-RANSAC	77
7.4	Improving axis position estimate	83
8	Tip localization	87
8.1	Estimating the threshold T_t	88
8.2	Estimating the maximum break length b_{max}	90
9	Experiments	95
9.1	Localization accuracy measures	95
9.1.1	Axis accuracy	96
9.1.2	Tip accuracy	96
9.2	Simulated 3D ultrasound images	97
9.2.1	Numerical simulation of 3D ultrasound images	98
9.2.2	Electrode distance from the probe	101
9.2.3	Electrode orientation	104
9.2.4	Electrode length	107

9.2.5	Background noise	108
9.2.6	Curved electrode	111
9.3	Real 3D ultrasound images	112
9.3.1	Acquisition of ultrasound images	112
9.3.2	Localization results	118
9.4	Implementation and computational time	121
10	Conclusions	123
A	Author's publications	125

List of abbreviations

CAD	computer aided diagnostic
CAS	computer aided surgery
CT	computed tomography
FWHM	full width at the half maximum
FOV	field of view
LMS	least mean squares
LZT	lead zirconate titanium
MF	model fitting
MF1	model fitting algorithm with the axis shape model
MF2	model fitting algorithm with the intensity priors
MF3	model fitting algorithm with the intensity profile
MISE	mean integrated squared error
MR	magnetic resonance
PIP	parallel integral projection
PSF	point spread function
PVA	polyvinyl alcohol
RANSAC	random sample consensus
R-RANSAC	randomized random sample consensus
RF	radio-frequency
ROI	region of interest
SNR	signal to noise ratio
US	ultrasound

Chapter 1

Introduction

Many medical interventions involve using specially designed surgical instruments. Thin needles, electrodes and probes are commonly employed for extracting cell samples, introducing substances into the tissue and measuring the electric activity in the cortex.

The small dimensions of the instruments make it difficult to accurately determine their position inside the body. A number of techniques have been proposed to solve this problem. Horsley and Clark, in 1908, pioneered the stereotactic surgery [1]. This approach makes use of a stereotactic frame, which is a mechanical device equipped with a three-axis targeting system that is registered to the internal organ structure via external bodily landmarks [2]. However, the high variability of the spatial relation between the outer landmarks and inside organs decreases the localization accuracy. To surmount this problem, the stereotactic frame is nowadays combined with pre-operative images acquired by the MR or CT imaging modalities. This has significantly improved the accuracy that was reported be of the order of 0.1 millimeter [3]. To avoid the limitations and patient discomfort associated with the stereotactic frame, frame-less techniques are employed. One of them is the electromagnetic tracking [4]. Three orthogonal coils attached to the operating theatre generate electromagnetic waves that are picked up by small coils fixed to the tracked instrument. Its position is estimated from the phase shift of the received signals. An optical tracking [5] with two calibrated cameras is also used in the trans-cranial magnetic stimulation [6]. The 3D position of a marker attached to the tracked tool is determined from its projection in both images.

In the last few decades, the medical imaging systems became an integral part

of the intra-operative procedures, since they allow the physicians to simultaneously display the surgical instrument and the surrounding tissue. The ultrasound modality is particularly suitable for such applications because: (i) short acquisition time permits real-time imaging, (ii) no ionizing radiation is involved, (iii) it is compatible with metal objects, (iv) the resolution of modern ultrasound scanners is sufficiently good, (v) the purchase and the operational cost is low compared to other imaging modalities. In order to determine the position of the tracked tool, the region of tissue is scanned by an ultrasound scanner providing 2D images in a real-time. The instrument is identified visually by the physician.

Observing a 3D object using conventional 2D images, however, presents inherent limitations. In general, only a cross section is observable, unless the electrode axis is aligned with the scan plane. This requires from the operator not only the skill to recognize significant tissue structures, but also the ability to position the ultrasound probe so that the whole surgical instrument and the region of interest are visible in the acquired images.

To facilitate this task, we have been developing a new system that exploits the potential of 3D ultrasound imaging to automatically determine the position of a thin metallic electrode inside the body [7]. A 3D ultrasound scanner acquires images of a portion of the tissue which surrounds the electrode. In order to automatically locate the electrode inside the tissue, its position within the image coordinates must be found.

The objective of this thesis is to solve this problem by proposing a robust algorithm that automatically detects the electrode inside the 3D ultrasound image. We provide a concise summary of existing localization algorithms together with an introduction to the fundamentals of ultrasound imaging. Our principal contributions are three novel methods that permit to identify the electrode axis and its tip. In order to compare the algorithms with existing methods, we performed a number of tests on both simulated and real ultrasound images with the aim of quantifying the localization accuracy and speed.

The text of the thesis is organized as follows. We start with an introduction of the research context and describe medical applications where a precise localization of a thin electrode inside the body is required. This is followed by a brief description of the developed localization system and a discussion of the thesis objectives. In Chapter 3, we briefly explain the fundamentals of ultrasound imaging, image formation and discuss various aspects that influence the quality of acquired images.

Chapter 4 contains the state of the art of algorithms for object localization and processing ultrasound data. The classification of the methods is based on the type of input data, the features and prior knowledge which the algorithms use. The core of the thesis consists of Chapters 6-8. First method, which finds the axis by maximizing the Parallel Integral Projection transformation is described in Chapter 6. Chapter 7 deals with the second axis localization method that is based on the model fitting paradigm and the R-RANSAC estimator. Once the electrode axis is known, the tip is determined using a procedure discussed in Chapter 8. The results of experiments can be found in Chapter 9. The text concludes with Chapter 10, where the work and future prospective are summarized.

Chapter 2

Problem description

This chapter gives the research context of the thesis. We start with summarizing the potential medical applications for electrode localization techniques. We describe the developed ultrasound based localization system and state the principal objective of the work. This chapter concludes with a list of research problems related to the given task.

2.1 Motivation

In the course of clinical interventions, the physicians make use of specially designed instruments to perform specific surgical tasks. The surgical instruments are classified according to their purpose into several groups [8]. One of them includes the metallic electrodes, injection needles and miniature tips that serve for sampling tissue cells, introducing fluids into body, measuring cell activities, etc. Needles are routinely employed in aspiration biopsy which is used to diagnose medical conditions of a suspected tissue region in the breast or other organs. It involves inserting a thin needle into the mass or lump, which is followed by the extraction of cells that are examined under a microscope [9, 10]. Another example is the brachytherapy also known as the sealed source radiotherapy, which is used to treat the prostate cancer. Small radioactive rods are inserted inside the treated tissue by means of a hollow shaft [11]. Thin surgical tools are also used in the laparoscopy, which is a minimally invasive surgery performed inside the body cavities via small incisions in the abdominal wall [12]. Lastly, metallic electrodes are used in the domain of neuronal cortical recording to measure or to stimulate the electric activity of a specific group of neurons [13, 14].

In order to minimize the amount of bodily disruption and tissue trauma, it is advantageous to minimize the instrument dimensions. Instrument miniaturization, however, makes the accurate tool placement more challenging. A needle with the diameter of the order of hundreds of μm may bend while being introduced into tissue which results in an inaccurate placement of the tip, leading to failure of the treatment or post-operative complications. The precise navigation of surgical instruments is also vital in the intra-cranial surgery, where there is a risk of damaging major blood vessel. For this reason, the intra-operative imaging [15] is frequently used to allow the surgeon to find a safe surgical corridor through which the instrument is guided into the target place.

The navigation of electrodes using intra-operative imaging is predominantly visual. Consequently, the accuracy of tool placement depends greatly on the surgeon's ability to interpret the acquired images. With the aim of improving the speed, accuracy, reproducibility and repeatability of the electrode localization, we propose a procedure that permits to automatically determine the tool position from ultrasound images. Given an intra-operative image, the system automatically identifies the electrode position. This approach offers several advantages:

Defined accuracy. As the localization is done by a system, the accuracy can be determined and experimentally verified. This reduces the influence of the operator.

Robotic assisted surgery. A robotic system can be employed to automatically introduce the instrument into a particular location in the tissue [16, 17].

Improved visualization. With the known electrode position and geometry, it is feasible to combine this information with image data to render and enhance graphical representation of the tool. Recent advances in the intra-operative imaging proposed techniques of augmented reality which combine simultaneous visualization of real images and computer generated data such as a pre-planned trajectory of the surgical instrument [18].

2.2 Problem formulation

Figure 2.1 depicts the configuration of the localization system that is being developed at the CREATIS laboratory in Lyon in conjunction with the Center for Machine Perception (CMP) in Prague. The central unit is an ultrasound scanner

with 3D imaging capabilities that is equipped with a dedicated card providing sampled radio-frequency (RF) signal from the probe. The processing workstation connected to the scanner stores the RF data and processes them.

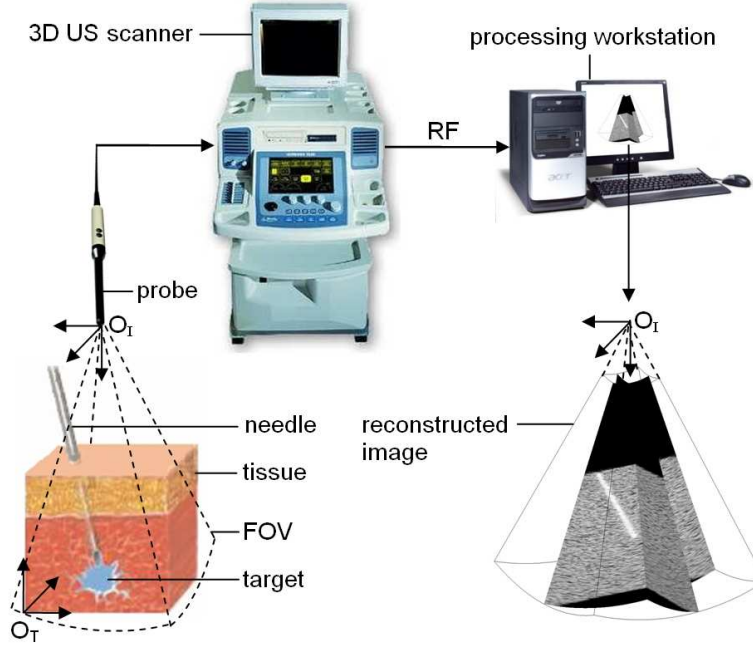


Figure 2.1: *Schematic illustration of the experimental system. The portion of the tissue containing the needle/electrode is scanned by a 3D ultrasound system. Acquired RF data are processed on a computer connected to the scanner to determine the instrument position within the image.*

The process of automatic electrode localization is comprised of two steps. First, the tissue containing the electrode is scanned by the ultrasound scanner and the radio-frequency data are transferred to the computer and stored on the disk. In the second phase, a 3D image is reconstructed and the position of the electrode is determined with respect to the probe/image coordinates system O_I . Assuming that the affine transformation between O_I and O_T is known, the electrode position with respect to the tissue is found.

The principal objective of our work is to propose an algorithm that permits to automatically determine the electrode position within the image coordinate system O_I . The algorithm shall be verified on a number of test images in order to determine the localization accuracy and computational cost.

2.3 Issues specific to processing ultrasound data

The problem of electrode localization from a 3D ultrasound image is challenging due to the inherent properties of ultrasound data and the required localization performance. More specifically, automatic object detection in an ultrasound image is made difficult by the following factors which are discussed in more details in Chapter 3:

Acquisition anisotropy. The strength of the object boundary is a function of the relative orientation between the transducer and the boundary. Consequently, some parts of the boundary are very bright, whereas some edges are missing which results in an apparent disruption of the object shape.

Shape changes. The resolution of an ultrasound system is anisotropic and varies with the distance from the foci, which influences the object dimensions.

Attenuation. The intensity of deeper located media structures decreases due to the attenuation of the ultrasound wave. This reduces the visibility of objects located further from the probe.

Noise. Medical ultrasound images are characteristic by its granular noise pattern called speckle, reducing the signal-to-noise ratio.

Artifacts. A number of artifacts such as the reverberation and refraction can be observed in an ultrasound images which distort the object appearance.

The electrode localization itself brings along some important issues that must be taken into account as well:

Accuracy. In this work, we deal with the localization of an electrode whose diameter is of the order of several hundreds of microns and hence the electrode dimension is comparable to the axial resolution of the ultrasound system.

Curved axis. A thin electrode is prone to bend as it is introduced into the tissue. The localization algorithm should be therefore designed to cope with the detection of an electrode with a curvilinear axis.

Processing time. The proposed method is intended for intra-operative applications. Hence the localization must be performed in near real-time despite large datasets represented by input 3D images.

Chapter 3

Technical Background

The aim of this chapter is to provide the reader with fundamental information that are needed to understand the text in consecutive chapters. Three topics are covered. First, the basics of ultrasound imaging are summarized including sound propagation, instrumentation and image formation. To test the proposed algorithms, numerical phantoms were generated using a software simulator FIELD II. The description of its use along with an example are given in Section 3.2. Section 3.3 is focused on the estimator RANSAC that is used in one of the proposed methods (Section 7).

3.1 Ultrasound imaging

Medical ultrasound is a diagnostic modality permitting to view anatomical structure of organs. It exploits the backscattering of acoustic energy on the boundaries between tissues. A number of pressure pulses are transmitted into the body along pre-determined trajectories, each of them forming a narrow ultrasound beam. Images are produced from backscattered signals received for each beam. Typically, the frequencies used in medical practice are in the range from 1 to 20 MHz.

The ultrasound imaging modality is capable of real-time imaging with a frame rate from 5 to 80 frames per second. No ionizing radiation is involved and the tissue is not mechanically altered in any way. An ultrasound scanner is portable and relatively easy to use. The purchase and operational cost are relatively modest compared to other medical imaging modalities. However, some parts of the body such as bones or lungs can not be properly imaged using medical ultrasound, since they impede the wave propagation.

Major applications of medical ultrasound can be found in the obstetrics to assess fetal health, in the cardiology to diagnose heart function and in general diagnostics to investigate inner organs such as the liver, kidney and spleen.

3.1.1 Sound propagation in medium

The propagation of sound is caused by a continuous interchange between the kinetic energy and the potential energy of medium particles, which is related to the density and the elastic properties of the medium [19]. In water and biological tissues the waves are primarily longitudinal, see Figure 3.1.

The propagation of the sound wave in a medium is governed by the acoustic wave equation that describes the evolution of pressure $p(x, t)$, which is function of the position x and time t . Let us consider a longitudinal wave with a planar wave front in a 1D case. Let us further assume that the medium is homogeneous and does not attenuate the wave. The pressure $p(x, t)$ is related to the sound velocity c in the medium by a second-order differential equation called the 1D linearized loss-less wave equation,

$$\frac{\partial^2 p(x, t)}{\partial x^2} - \frac{1}{c^2} \frac{\partial^2 p(x, t)}{\partial t^2} = 0. \quad (3.1)$$

Using the medium compressibility κ [Pa^{-1}], the sound velocity c can be expressed in terms of medium density ρ ,

$$c = \frac{1}{\sqrt{\kappa\rho}}. \quad (3.2)$$

The sound velocity for some materials is summarized in Table 3.1. In the case of a harmonic sound wave with frequency f , the propagation velocity is given by

$$c = \lambda \cdot f, \quad (3.3)$$

where λ is the sound wavelength in the medium. This relation is used to determine the resolution of an ultrasound system in the direction of sound propagation (Section 3.1.5).

Let $p(t)$, resp., $v(t)$ be the acoustic pressure, resp., the particle velocity for a fixed position x . Given a sinusoidal source of sound with the frequency f , both $p(t)$ and $v(t)$ are periodic with the period $T = \frac{1}{f}$ and the peak values p_0 , v_0 . In clinical imaging, the maximum amount of sound energy safely absorbed by the

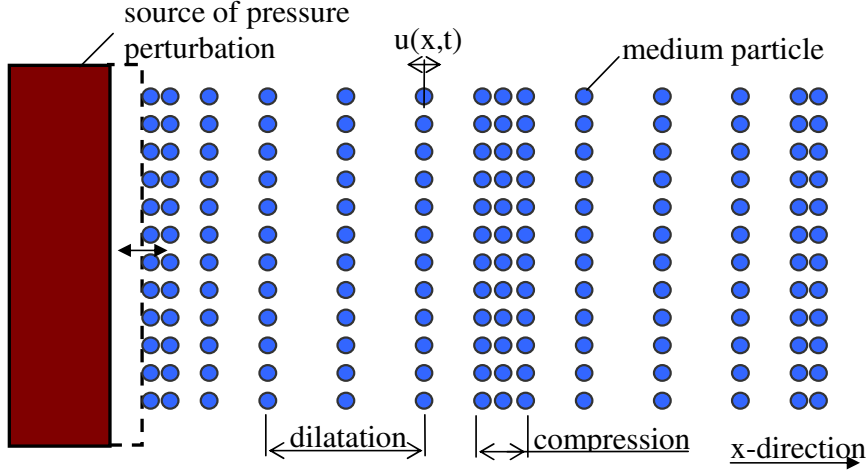


Figure 3.1: *Illustration of the propagation of a 1D longitudinal wave in homogeneous, loss-less medium.*

body is limited. It is measured using the average intensity I [$\text{W}\cdot\text{m}^{-2}$] defined as the integral of instantaneous intensity $i(t) = p(t)v(t)$ over the period T ,

$$I = \frac{1}{T} \int_0^T p(t)v(t)dt, \quad (3.4)$$

which is in the case of a harmonic wave equal to $\frac{1}{2}p_0v_0$.

The acoustic properties of the medium are expressed in terms of the acoustic impedance Z , which is the product of the medium density ρ and sound velocity c ,

$$Z = \rho \cdot c. \quad (3.5)$$

The acoustic impedance Z is a material constant and can be also expressed in terms of the density ρ and the medium compressibility κ ,

$$Z = \sqrt{\frac{\rho}{\kappa}}. \quad (3.6)$$

The unit rayl defined as $1 \text{ [rayl]} = 1 \text{ [kg}\cdot\text{m}^{-2}\cdot\text{s}^{-1}]$ is commonly used to quantify the acoustic impedance. The acoustic impedance of selected materials and biological tissues is listed in Table 3.1.

Reflection, transmission and refraction of sound wave

The acoustic impedance (Equation (3.6)) is used in modeling the interaction of sound wave with a boundary between two homogeneous media. Assuming a planar boundary with dimensions much greater than the wavelength λ , a certain

	sound velocity [m·s ⁻¹]	acoustic impedance × 10 ⁻⁶ [kg·m ⁻² ·s ⁻¹]
Water	1484	1.48
Aluminium	6420	17.00
Air	343	0.0004
Blood	1550	1.61
Fat	1450	1.38
Liver	1570	1.65
Kidney	1560	1.62
Skull bone	3360	6.00

Table 3.1: *Sound velocity and acoustic impedance for selected materials and biological tissues.*

portion of the incident energy is reflected while the remaining portion is transmitted (Figure 3.2). To quantify the portion of reflected and transmitted energy, intensity reflection coefficient R_I and intensity transmission coefficient T_I are used. They are defined as the ratio of reflected intensity I_r , resp., transmitted intensity I_t to the intensity of incident wave I_i ,

$$R_I = \frac{I_r}{I_i} = \frac{(Z_2 \cos \theta_i - Z_1 \cos \theta_t)^2}{(Z_2 \cos \theta_i + Z_1 \cos \theta_t)^2}, \quad (3.7)$$

$$T_I = \frac{I_t}{I_i} = \frac{4Z_2Z_1 \cos^2 \theta_i}{(Z_2 \cos \theta_i + Z_1 \cos \theta_t)^2}, \quad (3.8)$$

where Z_1 , resp., Z_2 is the acoustic impedance of the first, resp., the second medium. The equations governing the angles of incidence θ_i , reflection θ_r and transmission θ_t are given by,

$$\theta_i = \theta_r, \quad (3.9)$$

$$\frac{\sin \theta_i}{\sin \theta_t} = \frac{c_1}{c_2}, \quad (3.10)$$

where c_1 , resp., c_2 is the sound velocity in the first, resp., the second medium. In the case of different c_1 , c_2 , the transmitted wave is deviated from the direction of incident wave leading to misregistration artifacts in an image. This phenomenon is known as refraction.

The amount of reflected energy depends on the ratio between Z_1 , Z_2 , see Equations (3.7), (3.8). For example, on the boundary soft tissue/bone, the intensity

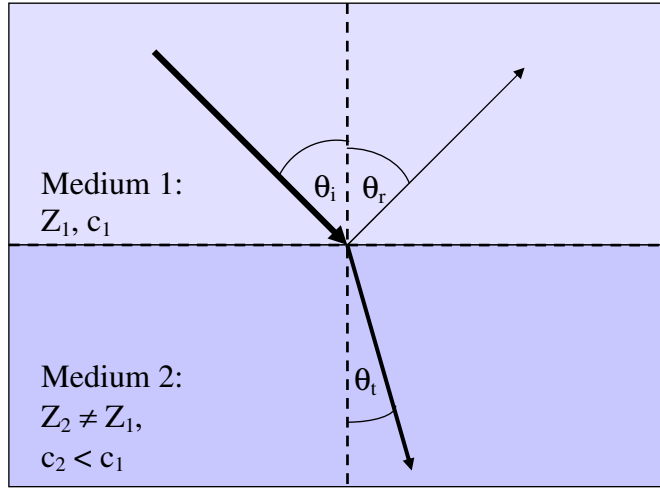


Figure 3.2: *Transmission and reflection of a sound wave on a planar boundary between two media with distinct acoustic properties. The intensity of the reflected and transmitted wave together with the angles of reflection and transmission depend on acoustic impedances Z_1 , Z_2 and sound velocities c_1 , c_2 .*

of reflected wave is approximately 40% of the intensity of incident wave, which strongly attenuates the transmitted sound wave, making the structures behind the interface difficult to perceive. Using values of acoustic impedance listed in Table 3.1, we can show that the intensity of the reflected sound wave from an interface within soft tissue is typically around 0.1% of the incident intensity.

Scattering

When an incident wave encounters medium particles or surface irregularities with the size smaller or comparable to the wavelength, its energy is reflected into many directions in the form of a spherical wave, see Figure 3.3.

The angular dependence and the magnitude of reflected energy depends on many factors including the shape, the size and the acoustic properties of scatterers. This makes expressing scattering properties in the analytic form difficult. Instead, some approximations were proposed. The Born approximation [19, 20] characterizes the scattering in terms of the so-called scattering cross section defined as the scattered power per unit of the incident wave intensity.

During the scanning process, spherical waves generated by a very large number of small particles interact through positive and destructive interferences, which

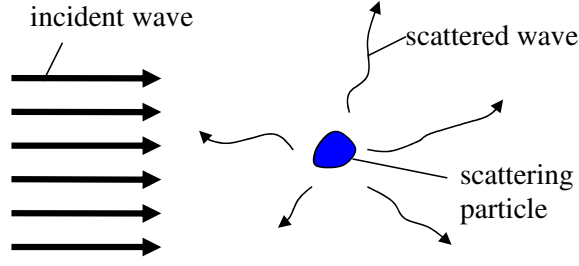


Figure 3.3: *The energy of a sound wave is dissipated in all directions when the wave encounters a medium inhomogeneity smaller than the wavelength. The scattered sound wave propagating along the path of original wave is called backscattered wave.*

results in a typical “speckle” noise pattern of ultrasound images. Although scattering has a negative effect on the signal-to-ratio of ultrasound images, it has the potential to characterize the tissue [21, 22, 23].

Absorption

As a sound wave propagates through the medium, some of its energy is converted into heat. This kind of energy loss is referred to as the absorption. Two major mechanisms are involved: (i) viscosity of medium particles, (ii) relaxation phenomenon linked to relaxation time needed for particles to return to neutral positions. It becomes important when the relaxation time is comparable to the period of a sound wave.

Attenuation

Attenuation designates the loss of wave energy in a heterogeneous medium due to the reflection, refraction, scattering and the absorption. It is approximated by an exponential decrease of the intensity $I(x)$ of the sound with the propagation distance x ,

$$I(x) = I(0) \cdot e^{-\mu x}, \quad (3.11)$$

where μ [cm^{-1}] is the intensity attenuation coefficient. Its value is often given in units of decibels per centimeter μ [$\text{dB} \cdot \text{cm}^{-1}$]. The conversion factor between μ [$\text{dB} \cdot \text{cm}^{-1}$] and μ [cm^{-1}] is given by

$$\mu [\text{dB} \cdot \text{cm}^{-1}] = \frac{1}{x} 10 \log_{10} \frac{I(0)}{I(x)} = 10(\log_{10} e) \mu [\text{cm}^{-1}] = 4.343 \mu [\text{cm}^{-1}]. \quad (3.12)$$

As both the scattering and the absorption depend on the frequency f , μ is also a function of f . In a biological tissue, this relationship is approximately linear,

$$\mu [\text{dB} \cdot \text{cm}^{-1}] = \alpha [\text{dB} \cdot \text{cm}^{-1} \cdot \text{MHz}^{-1}] \times f [\text{MHz}], \quad (3.13)$$

with a typical value of frequency dependent intensity attenuation coefficient α between 0.5 and $1 \text{ dB} \cdot \text{cm}^{-1} \cdot \text{MHz}^{-1}$. Assuming a single frequency sound wave at 7 MHz propagating in a tissue, the intensity attenuation in the depth 5 cm is 35 dB . Decreasing the frequency permits to investigate deeper located parts of a body at the price of deterioration of the axial resolution which is inversely proportional to the frequency, see Section 3.1.5.

3.1.2 Imaging instrumentation

The transducer is a key component of an ultrasound system. It acts as a converter of the electrical signal to the mechanical energy and vice versa. In transmission, the transducer excited by a short electric pulse generates mechanical vibrations, which are transmitted into the body as a sound wave. Subsequently, the transducer operating in a reception mode converts the received sound waves into electrical signals which are processed and displayed as an ultrasound image, see Section 3.1.4.

The core of a transducer is a piezoelectric crystal, which exhibits the piezoelectric phenomenon (Figure 3.4). The most common frequently used piezoelectric material is the lead zirconate titanium (LZT). The crystal is shaped into the form of plate with a flat (unfocused transducer) or a concaved (focused transducer) surface.

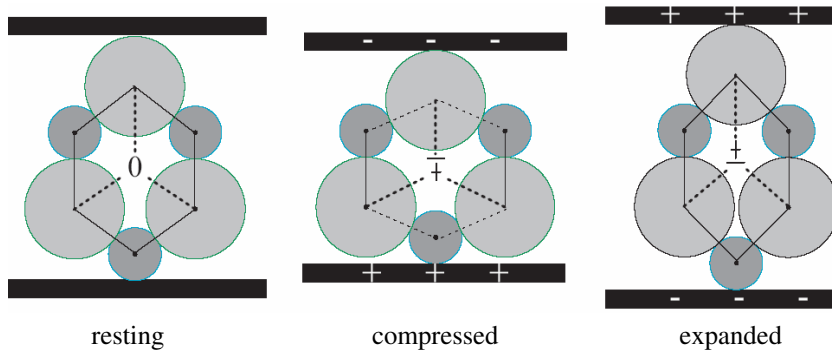


Figure 3.4: *Piezoelectric phenomenon. Applying the harmonic voltage across LZT crystal electrodes results in periodical change of its physical dimensions and vice versa.*

Applying the harmonic voltage across its surface, the thickness of the crystal periodically changes at the same frequency. The natural resonance frequency f_0 of a LZT crystal is given by

$$f_0 = \frac{c_{cryst}}{2d}, \quad (3.14)$$

where c_{cryst} [m·s⁻¹] is the sound velocity in the crystal and d is the crystal thickness; typical value of c_{cryst} for a LZT crystal is 4000 m·s⁻¹. The crystal is tuned to a particular frequency by changing its thickness. At the end of a voltage pulse, the crystal continues to oscillate before it stops. A backing material behind the crystal is used to damp these free oscillations, leading to a shorter emitted sound pulse, which improves the axial resolution, see Section 3.1.5. In addition, reducing the width of emitted pulse broadens the frequency bandwidth of a sound wave which is exploited for subharmonic [24, 25] and harmonic imaging [26].

Transducers

Most commercial imaging transducers are composed of an array of small piezoelectric crystals. This configuration is used for electronic beam forming and dynamic focusing with multiple focal points. The physical layout of crystals on the transducer determines the size of the field of view (FOV) and its dimensionality (2D or 3D). Basic types of ultrasound transducers for 2D and 3D scanning are discussed in the following paragraphs.

Transducers with a 2D field of view

Linear scanning. A linear transducer consists of a large number (64 – 512) of rectangular piezoelectric crystals (Figure 3.5). Applying a voltage pulse to a small number of adjacent crystals, a thin sound beam is produced. After all the backscattered echoes have been received by the same subgroup of crystals, a second voltage pulse is applied to the neighbouring elements, creating a beam displaced laterally with respect to the first beam. Sequential excitations of subgroups of crystals continue until all such groups have been excited. This type of imaging provides 2D images with rectangular field of view (Figure 3.7). Its advantage is a large FOV close to the transducer surface.

Sector scanning. The physical layout of a sector transducer is the same as the layout of a linear transducer. The difference is in the mode of operation. The

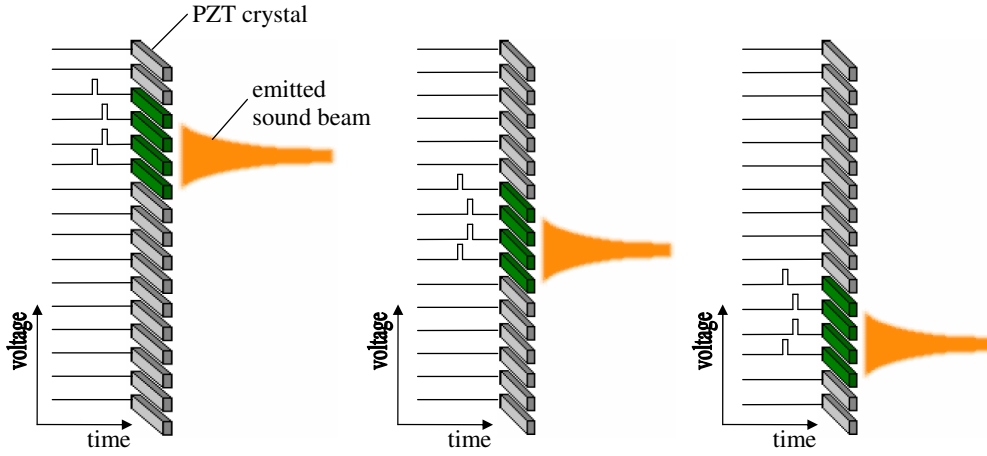


Figure 3.5: *Physical layout of multi-element transducer with a 2D FOV and linear scanning. In sequence, a small number of adjacent crystals is excited with electrical pulses to produce a series of parallel sound beams.*

voltage pulse exciting each piezoelectric crystal of sector transducer is delayed in time with respect to each other (Figure 3.6). The sound waves from all piezoelectric elements interact with each other creating a thin, focused beam. Its direction and the position of the focal point are electronically controlled through time-delayed excitation pulses.

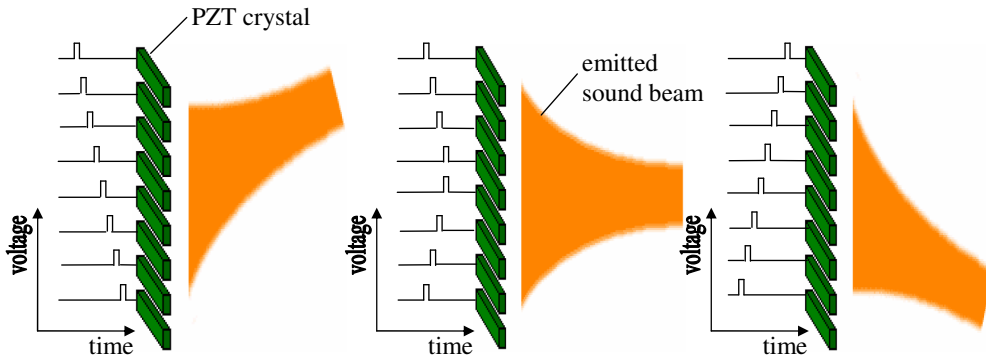


Figure 3.6: *Physical layout of multi-element transducer with 2D FOV and sector scanning. Electric pulses applied to crystals are time-delayed to steer and focus emitted sound beams.*

There is a number of other 2D transducers such as the switched linear arrays, circular arrays and annular arrays [19, 27].

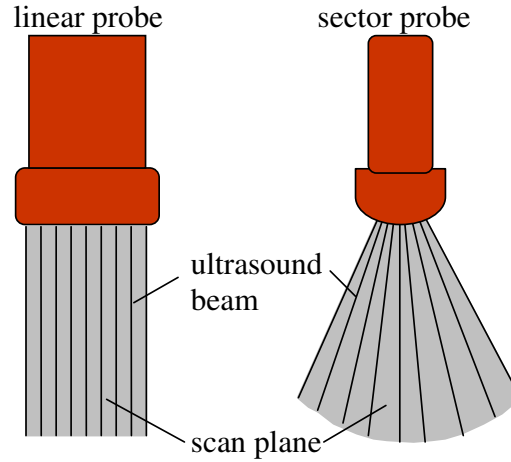


Figure 3.7: *Illustration of the FOV of 2D probes with linear and sector scanning.*

Transducers with a 3D field of view

Matrix transducers. The transducer can be arranged to form a matrix of piezo-electric elements. Such transducer permits to steer and focus the ultrasound beam electronically in the lateral and azimuthal direction, creating a 3D field of view. Due to beam focusing in both dimensions, lateral and azimuthal resolutions are better compared to other types of transducers with 3D FOV.

Multiple scan plane transducers. Since the matrix transducers are at the stage of development, most 3D imaging systems acquire volume data by scanning the FOV with several scan planes. The probe connected to the scanner is equipped with a linear (Figure 3.8) or a sector transducer (Figure 3.9) with a 2D FOV, which is shifted or tilted by a mechanical device to acquire data along a different direction of the 3D FOV.

3.1.3 Pulse-echo imaging

A conventional ultrasound scanner is composed of a transducer, transmitter/receiver switching circuit and a computer for data processing (Figure 3.10).

The ultrasound scanner operates in a pulse-echo mode. First, in transmission mode, the transducer is excited by a short electric pulse and generates a short sound impulse that is transmitted into the body in a narrow beam. At boundaries between organs and at tissue inhomogeneities, a small portion of the wave energy is backscattered in the direction of the transducer. Received waves are converted

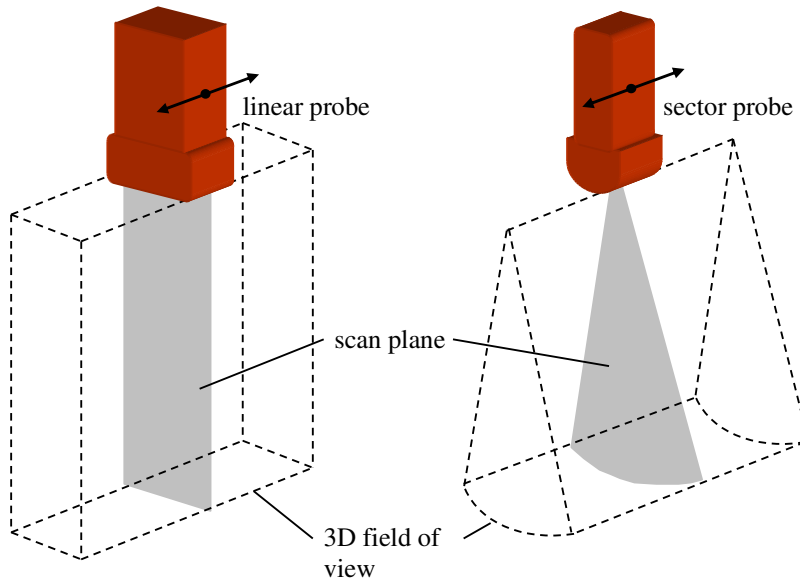


Figure 3.8: *Linear or sector transducer with 2D FOV is translated to acquire a series of parallel 2D images.*

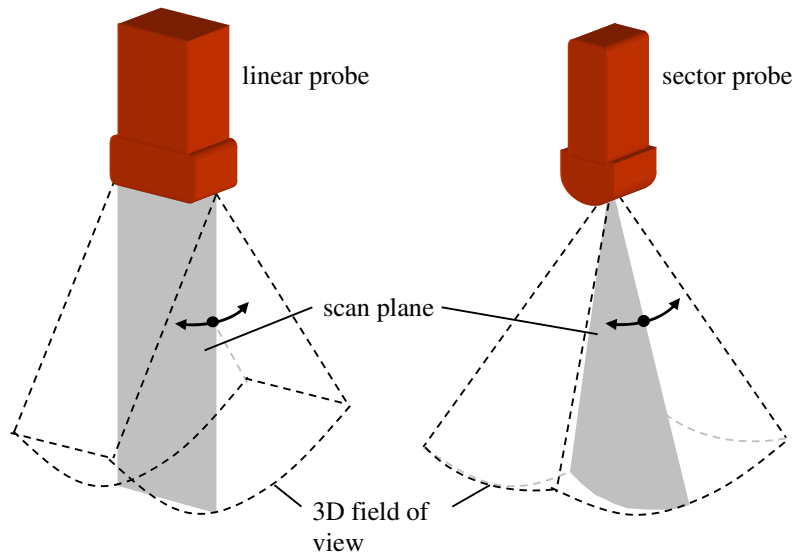


Figure 3.9: *The scan plane of a linear or sector probe is tilted while 2D images are acquired with a predetermined angular step.*

into electrical signal by transducer that has been switched into reception mode. From approximately known sound velocity in a tissue ($1540 \text{ m}\cdot\text{s}^{-1}$) and the time elapsed from transmission of a sound wave to the reception of its backscattered

counterpart, the distance of the boundary from the transducer can be determined. After all echoes have been received along one scan line, the beam is steered to acquire data along another direction. For a transducer with a 2D FOV, the number of scan lines varies from 128 to 512.

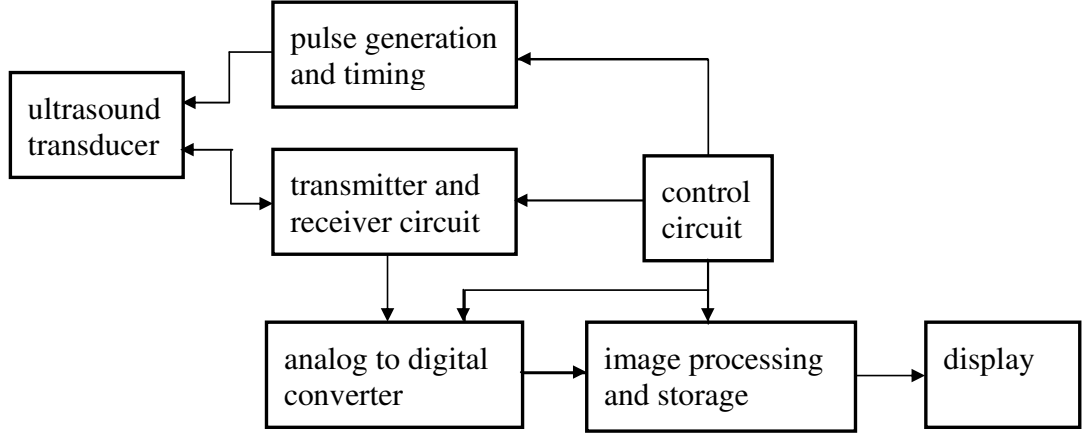


Figure 3.10: A schematic diagram of a conventional ultrasound imaging system.

3.1.4 Image formation

Let us assume a 3D ultrasound scanner with a radio-frequency output and a sector probe with mechanically tilted scan plane. Figure 3.11 illustrates the shape and the spatial discretization of the FOV. It is composed of N_{sp} scan planes, each containing N_b ultrasound beams. Let θ be the total tilt angle of the scan planes and φ the sector angle of one scan plane.

The scanner provides for each ultrasound beam a discrete 1D signal that corresponds to the signal received from the particular direction. These signals are often referred to as radio-frequency signals, since their frequency in medical diagnostics is of the order of MHz. Let us denote by $r_{i,j}[n]$ the RF signal sampled at frequency f_s that was acquired along the i -th ultrasound beam on the j -th scan plane; in this notation $n = 1, \dots, N_{smp}$ stands for the index of the n -th sample. Before constructing image, the RF signals $r_{i,j}[n]$ are processed by a sequence of signal processing algorithms to determine correspondent intensity values. This procedure is schematically depicted in Figure 3.12 and explained in following paragraphs.

Band-pass filtering. Received RF signals have the frequency components outside the frequency band of the transducer. These components correspond

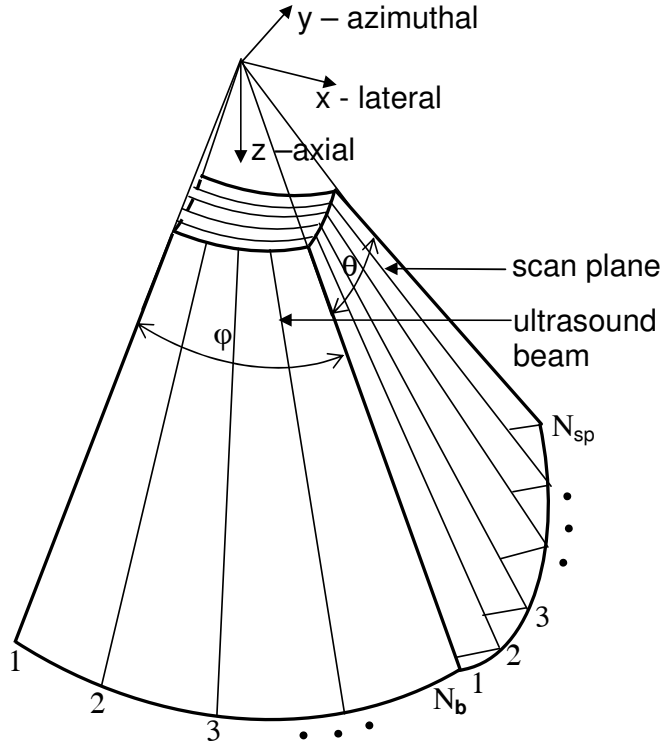


Figure 3.11: *Field of view of a sector transducer with a mechanically tilted scan plane. The FOV is sampled with N_{sp} planes each composed of N_b ultrasound beams.*

to noise. To suppress them, RF signals are filtered with a band-pass filter whose parameters are deduced from the frequency band of the transducer. Let us denote the filtered RF signals by $f_{i,j}[n]$.

Envelope detection. Image intensities shown on the ultrasound screen are derived from the amplitude envelope of filtered RF signals. The most common way of computing the RF signal envelope is via the Hilbert transform $\mathcal{H}\{\cdot\}$, which is for a continuous real-valued signal $x(t)$ given by

$$\hat{x}(t) = \mathcal{H}\{x(t)\} = \frac{1}{\pi} \int_{-\infty}^{\infty} \frac{x(\tau)}{t - \tau} d\tau. \quad (3.15)$$

The Hilbert transformation can be interpreted as the output of $\frac{\pi}{2}$ phase shifter with input $x(t)$ and the impulse response $h(t) = \frac{1}{\pi t}$. The amplitude envelope $e(t)$ of a signal $x(t)$ is computed as the complex module of the sum of the original signal and its Hilbert transformation,

$$e(t) = |x(t) + j\hat{x}(t)| = |x(t) + j(h(t) * x(t))|, \quad (3.16)$$

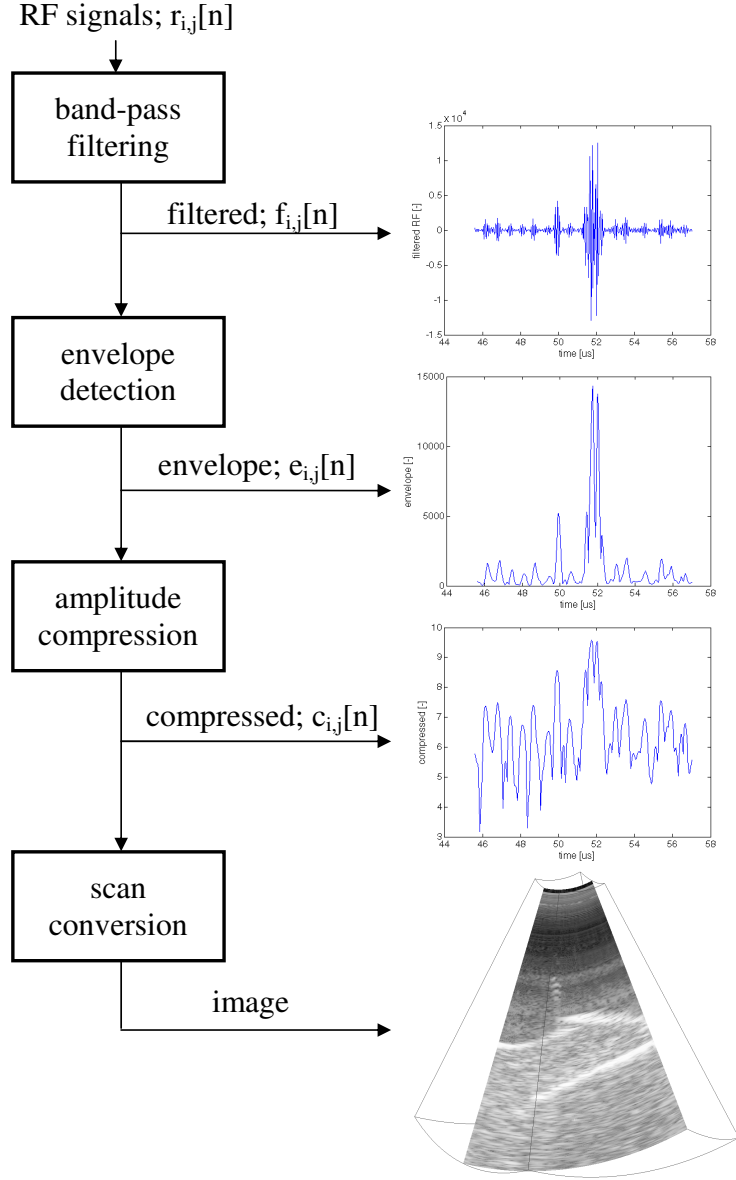


Figure 3.12: Block diagram illustrating the reconstruction of an ultrasound image from acquired RF signals. Intermediate data are shown on the right side.

where $*$ denotes a convolution. To obtain envelope signals $e_{i,j}[n]$, the envelope detection is applied to the filtered RF signals $f_{i,j}[n]$,

$$e_{i,j}[n] = |f_{i,j}[n] + j(h[n] * f_{i,j}[n])|; \quad \forall i, j = \langle 1, \dots, N_b \rangle \times \langle 1, \dots, N_{sp} \rangle, \quad (3.17)$$

where $h[n]$ is the impulse response of a discrete $\frac{\pi}{2}$ phase shifter,

$$h[n] = \begin{cases} 0, & \text{for even } n, \\ \frac{2}{\pi n}, & \text{for odd } n. \end{cases} \quad (3.18)$$

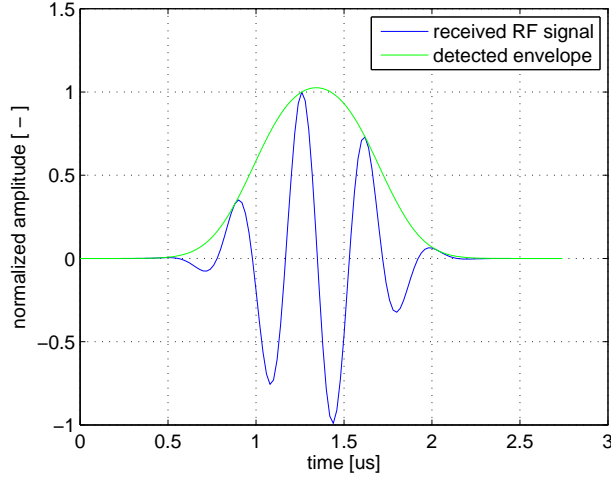


Figure 3.13: An example of a received RF signal with the frequency band of 2.5 MHz and the central frequency 3 MHz. The green curve depicts its amplitude envelope calculated via the Hilbert transform.

Logarithmic amplitude compression. The intensity of a backscattered sound wave from a boundary between two different tissues is much larger than the intensity of the backscattered sound wave from the tissue parenchyma. As a result, the dynamic range of RF signals and inherently of the envelope signals $e_{i,j}[n]$ can be as high as 80 dB impeding simultaneous display of highly and weakly reflecting tissue structures on a conventional ultrasound screen. In most ultrasound imaging systems, the amplitude of envelope signals is logarithmically compressed before displaying,

$$c_{i,j}[n] = n_1 \log(e_{i,j}[n] + n_2); \quad \forall i, j = \langle 1, \dots, N_b \rangle \times \langle 1, \dots, N_{sp} \rangle, \quad (3.19)$$

where n_1, n_2 are parameters that influence the degree of amplitude compression. Jensen [28] proposes for the purpose of visualization to set both parameters n_1, n_2 to 1.

Scan conversion. The values in $c_{i,j}[n]$ specify the intensity of voxels aligned along the i -th ultrasound beam on the j -th scan plane. To display the acquired image, we must determine for each $c_{i,j}[n]$ its coordinates in a defined coordinate system. In case the FOV is oriented in the coordinate system as is depicted in Figure 3.11, we define a discrete image function $V: \mathcal{X} \rightarrow \mathcal{I}$ by

$$V \begin{pmatrix} x(i, j, n) \\ y(i, j, n) \\ z(i, j, n) \end{pmatrix} = V \left(\frac{n \cdot c_{med}}{2f_s} \begin{pmatrix} \sin(\varphi_i) \\ \cos(\varphi_i) \cdot \sin(\theta_j) \\ \cos(\varphi_i) \cdot \cos(\theta_j) \end{pmatrix} \right) = c_{i,j}[n];$$

$$\forall i, j, n = \langle 1, \dots, N_b \rangle \times \langle 1, \dots, N_{sp} \rangle \times \langle 1, \dots, N_{smp} \rangle, \quad (3.20)$$

where

$$\varphi_i = \frac{\varphi}{N_b - 1}(i - 1) - \frac{\varphi}{2}, \text{ resp.} \quad (3.21)$$

$$\theta_j = \frac{\theta}{N_{sp} - 1}(j - 1) - \frac{\theta}{2}, \quad (3.22)$$

is the scan angle of the ultrasound beam, resp., the tilt angle of the scan plane; c_{med} is the sound velocity in the medium (in biological tissue, c_{med} is typically $1540 \text{ m}\cdot\text{s}^{-1}$). To display a planar section of the ultrasound image, the values of the image function $V: \mathcal{X} \rightarrow \mathcal{I}$ are interpolated on the rectangular grid using the trilinear or the nearest neighbour interpolation. The image can be further processed through filtering, thresholding and gray scale mapping to enhance the visual information.

3.1.5 Spatial resolution of the ultrasound system

The image of a point target is called the point spread function (PSF). PSF is used to describe the spatial resolution of an ultrasound imaging system by measuring the dimensions of the contour of the PSF where the intensity falls by 6 dB. In the case of 3D imaging system, we distinguish three types of spatial resolutions:

Axial resolution is defined as the spatial resolution along the direction of sound propagation. It is determined by the time duration of the transmitted pulse T_p and sound velocity c in the medium,

$$\Delta_{axial} = \frac{1}{2}T_p c. \quad (3.23)$$

Given a transducer operating at the central frequency 7.5 MHz, the axial resolution in the tissue is approximately 0.4 mm. Increasing the transducer

damping and the frequency of sound improves the axial resolution. However, increasing the frequency also reduces the depth of penetration due to higher attenuation (Section 3.1.1).

Lateral resolution is the spatial resolution in the scan plane that is in the direction transverse to the beam. It is determined by the cross-section of the wave intensity profile that is approximated by a Gaussian function. The full width at half maximum (FWHM) of this function quantifies the lateral resolution $\Delta_{lateral}$,

$$\Delta_{lateral}(z) = 2\sigma(z)\sqrt{2\ln 2}, \quad (3.24)$$

where $\sigma(z)$ is a function of propagating distance z along the beam. The lateral resolution is usually inferior to the axial resolution and is of the order of 1 mm. To improve it, beam focusing is used. This is achieved through mechanic focusing using an acoustic lens (single-crystal transducers) or electronically by dynamic focusing with several foci in transmission and reception (multi-crystal transducers).

Azimuthal resolution is measured in the direction orthogonal to the scan plane and is influenced by the width of the ultrasound beam. In contrast to the lateral resolution that can be electronically controlled by dynamic focusing and can be sharply focus over a considerable distance, the azimuthal resolution is mechanically determined by the curvature of the crystals that comprise the transducer. Thus, the beam is focused only in a narrow range of axial distance z . Its shape is independent of the beam profile in the scan (lateral) plane, see Figure 3.14. The lateral resolution is typically worse than the axial resolution and in the focal point is about 1 mm. A number of methods were proposed for estimating the width of the beam in the azimuthal direction [29, 30]

3.2 FIELD II

The software simulator FIELD II was developed by Jørgen Jensen [31, 32, 33] at the Technical university of Denmark. Composed of a set of MATLAB functions, it permits to create realistic 2D and 3D ultrasound images. In addition, it is capable of calculating transmitted and received pressure field for particular probe settings

allowing to display the energy distribution of a beam and to calculate a spatial resolution as a function of the axial distance.

3.2.1 Simulation of RF signal

The concept of the simulator is based on the spatial impulse response introduced by Tupholme and Stepanishen [34], which relies on a linear system theory. Given a single piezoelectric crystal emitting a spherical wave, the spatial impulse response determines at a particular point the pressure as a function of time. The analytic form of the spatial impulse response is found by the Rayleigh integral [33]. In case of a multi-crystal transducer, the spatial impulse response of transmitting transducer $h_t(t, \mathbf{x}_i)$ at the point \mathbf{x}_i is given by the sum of spatial impulse responses of individual crystals. Conversely, the spatial impulse response of the receiving transducer $h_r(t, \mathbf{x}_i)$ equals to the response to a spherical wave emitted by a point at the point \mathbf{x}_i . FIELD II calculates received RF signal by finding $h_t(t, \mathbf{x}_i)$, $h_r(t, \mathbf{x}_i)$ and convolving them with the electro-mechanical transfer function to yield the received voltage trace. Formally, the received RF signal $r_i(t)$ is given by

$$r_i(t) = v_{pe}(t) * h_t(t, \mathbf{x}_i) * f_m(\mathbf{x}_i) * h_r(t, \mathbf{x}_i), \quad (3.25)$$

where $*$ denotes spatial-time convolution, $v_{pe}(t)$ stands for the electro-mechanical pulse echo transfer function and $f_m(\mathbf{x}_i)$ accounts for the inhomogeneities in the density and sound velocity at the point \mathbf{x}_i .

3.2.2 Transducer settings

The form of functions $h_t(t, \mathbf{x}_i)$, $h_r(t, \mathbf{x}_i)$ depends on the transducer used and its parameters. Wide range of single and multi-crystal transducers (linear, sector) is supported and their parameters (number of crystals, physical dimensions, resonance frequency, electrical-mechanical transfer function) are fully configurable. For a given settings, FIELD II permits to trace the energy profile of a beam, see Figure 3.14.

3.2.3 Phantom definition

RF signal corresponding to one scan line is calculated by summing the RF signals over all scatter points \mathbf{x}_i , see Equation (3.25). Tissue structure to be simulated is described by a number of points with random spatial distribution. A value is

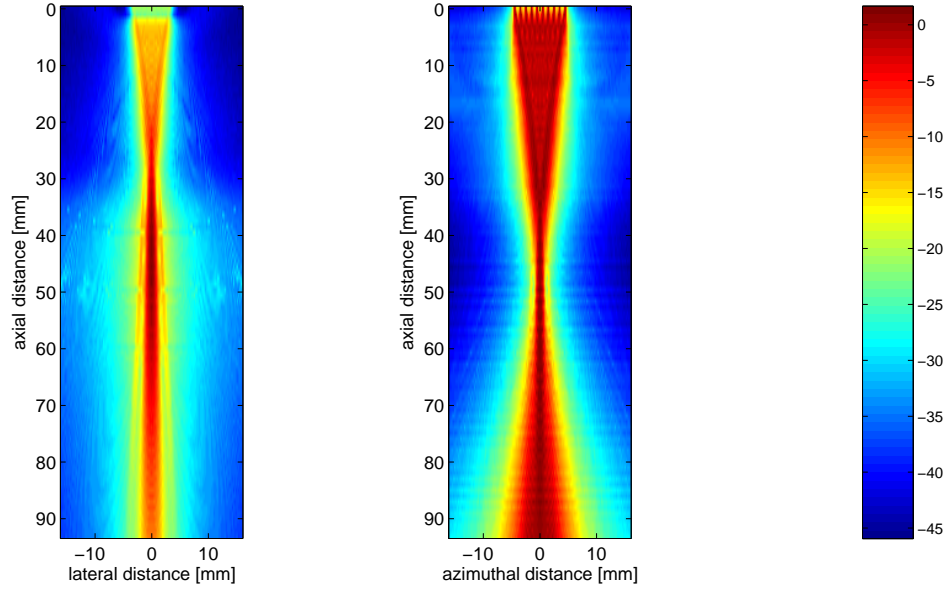


Figure 3.14: *Example of energy distribution (in dB) of a beam for transmission simulated with FIELD II for a linear transducer with three lateral focal points (at the axial distance 36, 50 and 60 mm) and one azimuthal focal point at 50 mm.*

assigned to each point to quantify the strength of backscattering at this point. An example of a simulated 2D ultrasound image comprising four types of tissue regions is shown in Figure 3.15. 100000 points were randomly distributed inside a cube of 60x45x15 mm with an uniform distribution. To each point, a random value with the zero-mean normal distribution and standard deviation 1 was assigned. If the point was inside the cyst region, its scattering coefficient was set to zero; it was multiplied by 10 within highly scattering region; and the point targets had scattering coefficients fixed to 100. The image was reconstructed from 128 RF signals simulated for a linear 192 crystal element transducer operating at 3 MHz with a transmission focus at 60 mm and two reception foci at 20 mm and 30 mm. The source code that generates such image can be found in the references [31, 28].

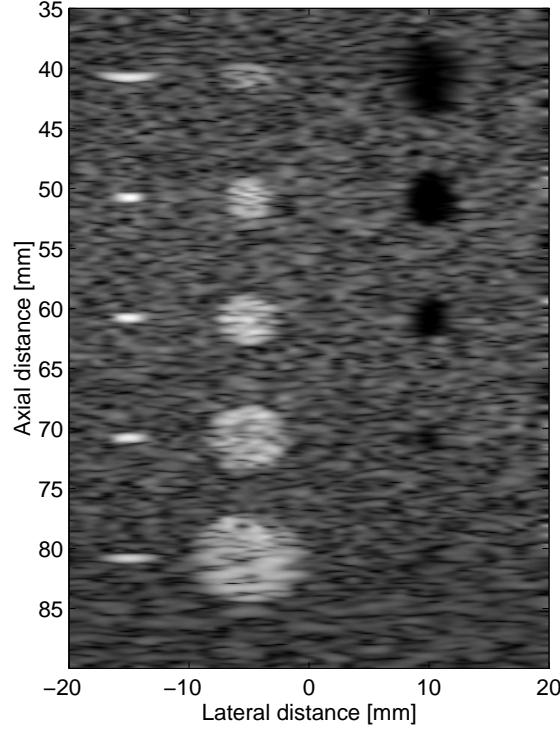


Figure 3.15: *Simulated ultrasound image in FIELD II representing a biological tissue with three distinct regions: (from left to right) (i) point targets, (ii) strongly reflecting regions, (iii) cyst regions.*

3.3 Estimator RANSAC

In signal and image processing applications, we often face the problem of estimating model parameters given a data containing a large portion of noise. **RAN**dom **SAM**ple **C**onsensus (RANSAC) algorithm is frequently used, because it gives robust results and makes very little assumption about the data. Since its introduction by Fishler and Bolles [35] in 1981, RANSAC has been implemented in the field of object fitting, stereo matching, motion segmentation and mosaicing.

In the context of parameters estimation, the term inliers denotes the points from input data set that are consistent with the best model (model quality is characterized using a cost function). The other points are referred to as the outliers or simply as noise. Given an input data set model and a cost function, RANSAC provides, with a certain predetermined probability, the model parameters that maximize the cost function and all inliers consistent with the corresponding model.

RANSAC is an iterative algorithm. Each iteration is composed of several steps.

First, a small subset of points is randomly selected from input data set and the model parameters are calculated. The size of the sample is the smallest sufficient for determining the model parameters. This maximizes the probability of finding an uncontaminated sample, i.e., a sample that contains solely inliers. In the second step, the quality of the estimated model parameters is evaluated using a cost function. A variety of functions have been proposed [36], the most common being the number of points consistent with the model. The stopping criterion is derived from the probability η of finding a better model. It is determined as the probability of missing an uncontaminated sample in the course of k consecutive iterations,

$$\eta = (1 - P_I)^k, \quad (3.26)$$

where P_I stands for the probability that an uncontaminated sample of size m is randomly selected from N data points containing I inliers,

$$P_I = \frac{\binom{I}{m}}{\binom{N}{m}} = \prod_{j=0}^{m-1} \frac{I-j}{N-j} \approx \varepsilon^m, \quad (3.27)$$

where ε is the fraction of inliers $\varepsilon = \frac{I}{N}$. The number of iterations that has to be drawn is

$$k = \frac{\ln \eta}{\ln(1 - P_I)}. \quad (3.28)$$

3.3.1 Randomized RANSAC

The speed of RANSAC depends on two factors. First, the percentage of outliers determines the number of random samples needed to guarantee the $1 - \eta$ confidence in the optimality of the solution. Second, the time needed to assess the quality of a hypothesized model parameters is proportional to the number N of the input data points. The total running time t of RANSAC can be expressed as

$$t = k(t_M + t_V), \quad (3.29)$$

where k is the number of samples drawn, t_M is time needed to instantiate a model hypotheses given a sample and t_V is an average time needed to evaluate the quality of the sample which is proportional to N .

Chum [37, 38] proposed an improvement of the standard RANSAC estimator by introducing a randomization of the hypothesis evaluation step, see Table 3.2. The principle of R-RANSAC is based on the observation that most model hypotheses

evaluated are influenced by outliers. To reject such erroneous models, it is sufficient to perform a statistical test on only a small number of data points. This can be formulated as follows. The hypothesis generation step proposes a model; it is either “good”, i.e. it leads to the optimal solution (the solution with the maximal support); or it is “bad”, i.e. one of the data points in the sample is an outlier. The property “good” is a hidden state that is not directly observable but is statistically linked to observable events. The observable event is the consistency of data points with the generated hypothesis.

In:	$U = \{x_i\}$	set of data points, $ U = N$
	$f : S \rightarrow p$	model parameters from a point sample
	$\rho(p, x)$	the cost function for a single data point
Out:	p^*	optimum model parameters
$k := 0$		
Repeat until $P\{\text{better solution exists}\} < \eta$ (a function of C^* and no. of steps k)		
$k := k + 1$		
I. Hypothesis		
	(1)	Select randomly set $S_k \subset U$, $ S_k = m$.
	(2)	Compute parameters $p_k = f(S_k)$.
II. Preliminary test		
	(3)	Perform $T_{d,d}$ test based on $d \ll N$ data points.
	(4)	Continue verification only if the test is passed.
III. Evaluation		
	(5)	Compute cost $C_k = \sum_{x \in U} \rho(p_k, x)$.
	(6)	If $C^* < C_k$ then $C^* := C_k$, $p^* := p_k$.

Table 3.2: Summary of RANSAC and R-RANSAC algorithms. The step II is added to RANSAC to randomize its evaluation.

The computational time is reduced by introducing a $T_{d,d}$ test into the model verification step of the standard RANSAC algorithm, see Table 3.2. The $T_{d,d}$ test is defined as follows:

$T_{d,d}$ is passed if all d data points out of d randomly selected are consistent with the hypothesized model.

The statistical test reduces the number of verified correspondences (and thus time complexity of the verification step), but it also increases a probability α of rejection of a good sample. Typically, the more data points are processed by the test the lower probability that a “good” model will be rejected. The task is to find the balance between the number of points d processed by the test and the increase in the number of samples, so that the total running time t is minimized. In [37, 38] Chum proved both theoretically and experimentally, that it is sufficient to test only a small number of data points compared to the total number of points in the dataset, that is $d \ll N$.

Chapter 4

State of the art

The complexity of the object localization task is primarily determined by the quality of input data. In the case of ultrasound images, this problem is particularly difficult because of numerous artifacts such as the speckle noise, attenuation, orientation dependent visibility of object boundaries, etc. In spite of recent advances in the transducer design, spatial/temporal resolution and signal processing algorithms which significantly increased the quality of acquired data, the automatic processing of ultrasound data still remains challenging. This chapter attempts to provide a brief review of the approaches that were proposed to solve the task of object localization and segmentation in ultrasound data. Due to the large number of publications, we first classify algorithms by the level of modeling the underlying physics of ultrasound imaging, see Section 4.1. Section 4.2 summarizes published methods according to the features and prior information which they employ. Finally, Section 4.3 is dedicated to the techniques that were specifically developed for detection of electrode-like objects in ultrasound data.

4.1 Methods modeling ultrasound physics

In Section 3.1.4, we illustrated the processing pipeline used to create an ultrasound image. The raw radio-frequency signal is processed through a number of numerical operations to produce an image suitable for visual examination by the physician. However, the processing can also remove information useful for object detection algorithms. A number of authors published object detection techniques that take into account the physics of ultrasound imaging and make use of only partially processed RF signals.

4.1.1 Radio-frequency data

The RF signal from the ultrasound transducer contains the information about the tissue scatterers. The RF data can be used to determine the mechanical and geometrical properties of scanned tissue. For instance, Bijmens [39] showed that the spectral components of the RF signal varies with the type and the density of scatterers in the tissue. Very little research was, however, carried out in the domain of RF based object localization. Bijmens and Boukerroui [40, 41] solve the segmentation problem using the mean central frequency, together with the backscatter power and a tissue measure derived from the envelope. Dydenko [42] proposed different measures of the RF signal (the envelope signal power, spectral autoregressive parameters and velocity parameters) to detect discontinuities and thus detect borders that define distinct objects in the image. The most recent technique that exploits RF signal to segment ultrasound data was proposed by Bernard [43, 44]. He models the RF signal with the generalized Gaussian distribution which is used in the maximum likelihood framework to segment cardiac images.

4.1.2 Envelope data

The envelope data are obtained from the RF signals by detecting the envelope using the Hilbert transform, see Section 3.1.4. The envelope images are known for its granular noise pattern (speckle), which is a phenomenon that exists in all systems that use coherent waves. Although the texture generated by the speckle does not directly depend on the characteristics of the scanned media, the mean of the local brightness does reflect the echogenicity of the underlying tissue [45]. The majority of published works consider the speckle noise as a random process and a number of distributions was proposed to describe the statistics of the envelope data. In case the number of randomly located scatterers is large (fully developed speckle), e.g., a tissue containing blood cells, the envelope of the echo signal is commonly modeled using the Rayleigh distribution [46]. For the case of special scattering conditions, two main classes of distributions were investigated: (i) the K -distribution is used if the effective density of the scatterers is low (partially developed speckle) [47], (ii) the Rice distribution models the coherent components of an echo signal due to the presence of a regular structure of scatters in the tissue [48]. More general models have been proposed in the literature as well, e.g., the

homodyned K -distribution [49]. However, they are noted for a high computational cost. Although some algorithms for the effective estimation of their parameters were published [50], more simple models are currently implemented such as the Nakagami distribution [51] or the generalized Gaussian distribution [52].

In terms of the image processing methods, the speckle pattern can be regarded as a signal that conveys some information about the tissue or as a noise that should be reduced. Among the most successful algorithms that make use of speckle as a feature are the methods for tissue characterization. Insana [48] used the speckle texture modeled by the generalized Rice distribution to distinguish between healthy and abnormal tissue samples. Other speckle distribution models such as the K -distribution [51, 53] and Nakagami [54, 53] have been tested as well. In the field of object detection, the algorithms, however, tend to treat the speckle as a noise, which disturbs the object contours. A pre-processing step is often applied to reduce the speckle. There is a number of existing algorithms that address the speckle suppression; for instance median filtering [55], morphological smoothing [56] and wavelet-based methods [57, 58].

4.1.3 Log-compressed images

The algorithms presented in the previous text use as a feature the parameters computed from the RF signal or from the envelope signal. In many cases, ultrasound scanners do not provide the access to the RF signals. Instead, they display an image of the envelope signal whose dynamic range has been compressed by a logarithmic operation [59, 19]. Techniques were developed to reconstruct the envelope data from the intensity values of the log-compressed data [60]. However, algorithms often process log-compress data directly without computing the corresponding envelope image. A variety of log-compressed intensity models [61] have been suggested in the literature such as the the Gaussian [62], exponential [63] and Gamma distribution [64]. These statistical models were implemented in conjunction with another methods such as the level sets segmentation [65] or active contour shape models [66].

4.2 Features and priors in object detection

In order to increase the robustness of the segmentation, the detection algorithms make use of a number of prior information about the sought object. In this section,

we review published works that are classified according to the employed features and constraints.

4.2.1 Edge features

Edges play an important role in the problem of the image-based localization, since they permit to delineate the object boundary. Consequently, many low-level methods for object localization consider edges as features [67].

Edges are often detected using the intensity gradient [68]. However, the detection of edges in ultrasound data by intensity gradient is challenging due to strong speckle noise which generates many false edges and thus makes the successive boundary delineation more difficult. To compensate for the speckle noise, some algorithms make simplified assumptions about the speckle statistics to develop computationally tractable algorithms. For instance, Donohue [69] proposed an edge detection algorithm that assumes a multiplicative model of the speckle noise. A survey of algorithms that make use of speckle models for estimating edges was published by Czerwinski [70].

Aside from the speckle noise, the estimation of object position based on the edge detection is limited by other phenomena connected to the ultrasound physics such as the dependence of the boundary strength on the object orientation or increasing attenuation with depth.

4.2.2 Shape priors

Edge features are often used in conjunction with priors such as the shape. This prior information may be incorporated into the algorithms in several ways. One class of techniques includes the active contours, where the shape prior is introduced as a boundary smoothness [71]. The object shape can be described as well by a family of parametric shapes [72]. The model parameters are estimated by fitting the model to data [73, 74]. The advantage of this approach is the simultaneous segmentation of an object and a retrieval of model parameters that describe its shape. An alternative way of introducing the geometrical constraint is by using a point distribution model which describes a typical shape derived from a training data using the principal component analysis [75]. The review of segmentation methods comprising shape priors that are classified according to medical applications was published by Noble [76].

4.2.3 Temporal priors

The ultrasound is a real-time imaging modality that is capable of acquiring a sequence of images with a high frame rate. This permits to improve the object detection by adding temporal priors that describe the motion of the target. Most methods that implement temporal priors can be found in the domain of echocardiography imaging where the goal is to segment the heart walls such as the ventricles [77]. In case of non-periodic motion, the segmentation result may be used as an initial solution for the segmentation in the next frame [78].

4.3 Existing electrode localization techniques

In this section, algorithms that were specifically designed to localize an electrode-like object in an ultrasound image are presented. We summarize the principle of each technique, discuss experimental setup and state achieved results in terms of localization accuracy.

4.3.1 PCA applied to a 2D variance image

Drapper [79] developed an image-based approach to track a breast biopsy needle in tissue. The input to the algorithm is a 2D ultrasound image showing a needle contained in the scan plane. The algorithm automatically identifies the needle axis, the location of intercept and tip point and delineates the needle position with a line-segment. Tests were performed on a tissue mimicking phantom containing a breast biopsy needle.

The algorithm is based on a hypothesis about electrode appearance in a 2D ultrasound image. The electrode voxels are assumed to be brighter than background voxels and the electrode axis to be straight. The estimation of electrode position consists of several steps:

- The variance of the region surrounding each pixel in the original ultrasound image I_0 is used to create a new variance image I_1 ,

$$I_1(i, j) = \frac{\sum_{k=-N/2}^{N/2} \sum_{l=-N/2}^{N/2} [I_0(i-k, j-l) - \bar{I}_0]^2}{N^2}, \quad (4.1)$$

where

$$\bar{I}_0 = \frac{\sum_{i=1}^N \sum_{j=1}^N I_0(i, j)}{N^2}. \quad (4.2)$$

This operation enhances the electrode voxels while reducing background noise. The kernel size N is a balance of needle enhancement and computational time. While larger kernels increase to some degree the intensity of electrode pixels, they cause increase in computational time. The optimal value of N is set experimentally.

- A binary image is created by thresholding the variance image to approximately classify electrode and background pixels. As the intensity of pixels vary across ultrasound images, a threshold T is chosen adaptively. The intensity of all pixels is modeled as a single normal distribution with the mean value μ and variance σ^2 , that are estimated from the data. This distribution is used to determine an appropriate threshold T as

$$T = \mu + k\sigma. \quad (4.3)$$

The value of $k > 0$ is found experimentally.

- To smooth the needle contour, a binary closing operation is used. A 3x3 symmetrical structuring element is chosen to eliminate small intrusions and to reduce the possibility of joining clusters of different image structures.
- Distinct clusters C_i , $i = 1, \dots, N$, of bright pixels are identified after the binary closing. A cluster C_i is defined as a group of pixels connected within the 8-pixel neighbourhood. Each cluster of pixels is processed using the principal component analysis to determine the best fitting straight line in terms of the least mean squares criterion. Let us denote by \mathbf{R}_i the covariance matrix of pixel coordinates in the cluster C_i ,

$$\mathbf{R}_i = \begin{pmatrix} \sigma_{xx}^2 & \sigma_{xy}^2 \\ \sigma_{yx}^2 & \sigma_{yy}^2 \end{pmatrix}. \quad (4.4)$$

The elements in the matrix, which are sample variances of pixel coordinates are given by,

$$\sigma_{xy}^2 = \frac{1}{|C_i|} \sum_{j=1}^{|C_i|} (x_j - \bar{x})(y_j - \bar{y}) \quad (4.5)$$

where \bar{x} , resp., \bar{y} are the mean x , resp., y coordinate of pixels in cluster C_i . Eigenvectors $\mathbf{v}_{i,1}$, $\mathbf{v}_{i,2}$ and corresponding eigenvalues $\lambda_{i,1}$, $\lambda_{i,2}$ are determined. The line approximating cluster C_i is defined by the eigenvector corresponding

to the largest eigenvalue. Its position is given by the mean (\bar{x}, \bar{y}) . The needle is then identified among the needle candidates as the cluster with the largest eigenvalue.

- The needle tip is found by masking the estimated needle line with the thresholded image. Clusters along the line separated by a gap smaller than the electrode diameter are joined together and considered to be a part of the same cluster. The tip is found as the endpoint of the largest cluster.

The algorithm was tested on a tissue-mimicking cryogel phantom with a breast biopsy needle of 2.1 mm in diameter. The phantom was scanned with a 2D ultrasound scanner operating at 5.5 MHz. The results show that the intercept and the needle tip can be determined by the algorithm with an accuracy of 1 mm for a depth of insertion greater than 15 mm.

4.3.2 PCA applied to a 3D image

Novotny enhanced the algorithm developed by Drapper [79] (Section 4.3.1) to a needle localization in a 3D image [80]. The volume data is initially segmented by thresholding. Using a 26-voxel neighborhood, adjacent voxels are grouped into mutually disjoint clusters. As in [79], the PCA is computed on each voxel cluster to determine the eigenvectors. The cluster that is the longest and the straightest, i.e., with the largest ratio of the first and second eigenvalue, is considered to be the needle. The needle orientation is given by the largest eigenvector. To find its position, the voxels of the selected cluster are projected on the plane orthogonal to the axis and a circle of a known radius is determined. The circle center defines a point incident with the needle axis. In the last step, the needle tip is simply found as the endpoint of the selected cluster along the direction of the needle axis.

This technique was implemented in a real-time 3D ultrasound-guided robotic system that autonomously navigates a surgical instrument into a specific target point [17]. The tests were performed on a 1.5 mm steel cannula submerged in a water tank and scanned with 3D ultrasound scanner Philips SONOS 7500. The experiments included measures of localization performance as a function of the instrument orientation and position. They indicate that the accuracy is approximately 0.8 mm.

4.3.3 Minimization of parallel image projections

The electrode segmentation algorithm proposed by Ding [81] is based on the observation that the electrode is more conspicuous in a 2D projection of the 3D image. The electrode area in the projection is minimized when the image is projected in the direction parallel to the electrode axis.

Initially, a region of interest (ROI) which contains the electrode is selected in the 3D image with the aim of cutting out background structures that might be considered as a part of the electrode. The ROI selection is based on a priori information about the electrode position that is determined by an approximate knowledge of the orientation and the entry point in the tissue.

Next, a 2D projection image of the ROI is formed by the ray-casting process [82] that accumulates voxel intensities I processed by a transfer function $f(I)$. The purpose of processing the intensity with a transfer function is to enhance electrode intensity while reducing the intensity of background. Ding proposed to use the Gaussian function,

$$f(I) = e^{-\frac{(I-\bar{I})^2}{2\sigma^2}}, \quad (4.6)$$

where that parameters \bar{I} , resp., σ^2 are set as the mean, resp., the variance of electrode voxel intensities. In order to identify the electrode in the 2D projection, the projected images is rescaled to a 0-255 range and thresholded with a constant threshold set to 25. The projected electrode position is defined by a LMS line fitted to the pixel above the threshold. Let us denote the line directional vector by \mathbf{p} and the direction of the projection by \mathbf{s} .

In general, the projection direction \mathbf{p} and the true electrode axis are not parallel and consequently the number of pixels in the thresholded image that defines the projection area A is not minimized. However, the true electrode axis is incident with the plane σ defined by \mathbf{p} and \mathbf{s} . To improve the estimate of the electrode axis, the projections are restricted to the plane σ

$$\mathbf{p}_0 = \mathbf{p} \cos \theta + \mathbf{s} \sin \theta. \quad (4.7)$$

One dimensional optimization over θ is performed to find θ^* that defines \mathbf{p}^* minimizing the projection A . Finally, the electrode orientation is defined by the \mathbf{p}^* and the mass center of the minimized projection area.

The localization performance was tested on volume images acquired by a 3D ultrasound system scanning a cryogel and a turkey breast phantom containing an electrode. The mean axis localization accuracy was 0.4 mm for the cryogel

and 0.6 mm for the turkey breast phantom. The processing time on a computer equipped with a volume rendering graphics card was 4 s for a 3D image of 40x40x40 voxels.

4.3.4 Segmentation in two orthogonal image projections

The correct segmentation of the previous method depends on the choice of the initial projection direction \mathbf{p}_0 , see Equation (4.7). If the initial projection direction is too far from the actual needle direction, the iterative process that minimizes the projection area A may become trapped in a local optimum.

To avoid this problem and further decrease the processing time, Ding published a localization technique that is based on two orthogonal image projections [83, 84]. The 3D image is projected along two mutually orthogonal directions $\mathbf{p}_1, \mathbf{p}_2$ and the electrode position is detected in both projections using Hough transform [85]; let us denote the directional vector of the electrode projection by \mathbf{s}_1 , resp., \mathbf{s}_2 . Assuming that the electrode axis is linear, the true electrode is located in both planes σ_1 , resp., σ_2 with normal vectors $\mathbf{p}_1 \times \mathbf{s}_1$, resp., $\mathbf{p}_2 \times \mathbf{s}_2$. Hence, the electrode axis position is found as the intersection of the planes σ_1, σ_2 . To improve the robustness and the accuracy, the projection directions $\mathbf{p}_1, \mathbf{p}_2$ are both set orthogonal to a priori known estimate of the electrode location. Similarly to the algorithm [81], only a small ROI is considered and the intensity are prior to the ray-casting operation processed by the Gaussian transfer function (Equation (4.6)).

Using the same experimental setup as in [81], the results indicate that the localization accuracy of this algorithm is 0.6 mm. The processing time on a standard computer equipped with a volume rendering card is approximately 70 ms for a 3D image of dimensions 81x81x312 voxels.

4.3.5 Superquadric fitting with RANSAC

Tao [73] proposed a method for segmentation of objects in 3D acoustic images that is based on a recover and select paradigm. This approach solves the segmentation task as a model fitting which is followed by grouping points that likely belong to the model. In this way, the segmentation also leads to the recovery of a parametric representation of the sought object.

The superquadric family of functions was selected as the template to model the geometry of the sought object, because it has as the ability to describe a wide

range of forms [86]. A superquadric surface $Q(x, y, z; \Lambda)$ is defined by an implicit equation:

$$Q(x, y, z; \Lambda) = \left(\left(\frac{x}{a_1} \right)^{\frac{2}{\varepsilon_2}} + \left(\frac{y}{a_2} \right)^{\frac{2}{\varepsilon_1}} \right)^{\frac{\varepsilon_2}{\varepsilon_1}} + \left(\frac{z}{a_3} \right)^{\frac{2}{\varepsilon_1}} = 1, \quad (4.8)$$

where a_1, a_2, a_3 define the size and $\varepsilon_1, \varepsilon_2$ control the shape of the surface. The position of the superquadric in a 3D space is fully described by additional parameters p_x, p_y, p_z determining the location and φ, θ, ψ that describe orientation. A homogeneous coordinate transformation \mathbf{T} is used to define the 3D points expressed in the superquadric centered coordinates system $[x, y, z, 1]^\top$ into the world coordinates $[x_w, y_w, z_w, 1]^\top$,

$$\begin{pmatrix} x_w \\ y_w \\ z_w \\ 1 \end{pmatrix} = \mathbf{T} \begin{pmatrix} x \\ y \\ z \\ 1 \end{pmatrix} \quad (4.9)$$

where the transformation matrix \mathbf{T} is give by [87]

$$\mathbf{T} = \begin{pmatrix} \cos \varphi \cos \theta \cos \psi - \sin \varphi \sin \psi & -\cos \varphi \cos \theta \sin \psi - \sin \varphi \cos \psi & \cos \varphi \sin \theta & p_x \\ \sin \varphi \cos \theta \cos \psi + \cos \varphi \sin \theta & -\sin \varphi \cos \theta \sin \psi + \cos \varphi \cos \theta & \sin \varphi \sin \theta & p_y \\ -\sin \theta \cos \psi & \sin \theta \sin \psi & \cos \theta & p_z \\ 0 & 0 & 0 & 1 \end{pmatrix}.$$

A superquadrics in general position has therefore 11 parameters that comprise the parameter vector $\Lambda = \{a_1, a_2, a_3, \varepsilon_1, \varepsilon_2, \varphi, \theta, \psi, p_x, p_y, p_z\}$. Given a set of points the parameter vector Λ can be retrieved using the Levenberg-Marquardt method [88]. The Euclidean distance of a point \mathbf{x} from the superquadric surface is approximated by the point distance from the superquadric bounding box.

The segmentation processed is composed of the estimation the superquadric model parameters (recovery) followed by a growing step (selection):

Recovery. Let $X \subset \mathbb{R}^3$ be the set of input points. The algorithm starts by a selection of M subsets of points S_i randomly chosen from X with the cardinality $|S_i|$ set to 30. The parameter vectors Λ_i of the superquadrics $Q(\mathbf{x}; \Lambda_i)$ are computed to fit the model into the subsets S_i . The quality of each superquadric is evaluated by the number of consistent points C_i and their mean distance \bar{d}_i .

Selection The selection phase is composed of two steps: (i) 10% of superquadrics with the highest number of consistent points are selected, (ii) from them, N superquadrics with the least mean error \bar{d}_i are selected. In the successive step the parameter vectors Λ_i of the N remaining models are recalculated to fit the points in X and the superquadric with the least mean error \bar{d}_i is considered as the sought object.

The experiments were performed on 3D sets of data points acquired from a high resolution acoustic camera working with frequency of 500 kHz. In the paper [73], the author does not include the achieved localization accuracy. However, he claims that the computational time is several seconds on a standard PC for range images of one thousand points.

Chapter 5

Description of input data

The algorithms presented in the following chapters process 3D ultrasound images of a portion of tissue that contains a metallic electrode. An example of such image is shown in Figure 5.1. It can be described by an image function given by

$$V: \mathcal{X} \rightarrow \mathcal{I} \quad (5.1)$$

where $\mathcal{X} = \{\mathbf{x}_1, \mathbf{x}_2, \dots, \mathbf{x}_{|\mathcal{X}|}\}$ are the voxel coordinates and $\mathcal{I} = \{I_1, I_2, \dots, I_{|\mathcal{X}|}\}$ are the intensity of voxels.

5.1 Region of interest

In the course of scanning, the distance of the probe from the scanned media is approximately known. Consequently, we can identify a region of interest in the acquired image that comprise only the tissue, see Figure 5.2. Let us therefore assume that the set \mathcal{X} in Equation (5.1) is composed of only those voxels that are inside the region of interest. The principal interest in focusing on a smaller part of the image is to reduce the time necessary to carry out the localization task.

5.2 Assumptions

The principle of the presented methods relies on several hypotheses made about the appearance of the electrode in an ultrasound image. We expect that the diameter of the metallic electrode is of the order of the ultrasound wavelength and is much smaller than the electrode length visible in the field of view. Taken into account such dimensions and distinct acoustic properties of metal and tissue, we

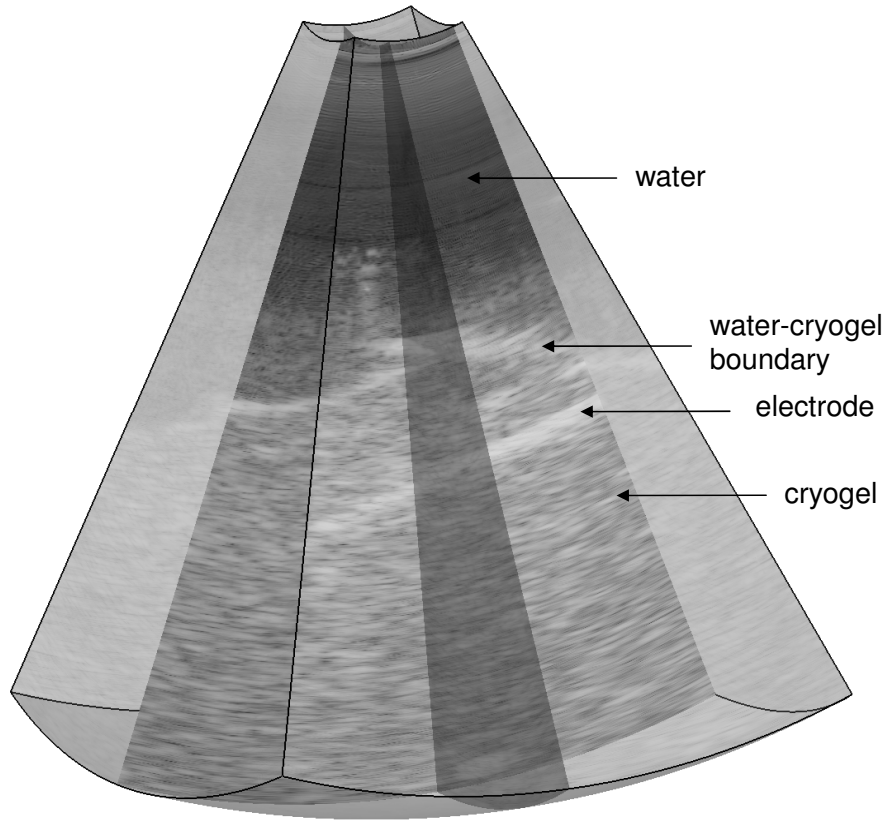


Figure 5.1: A 3D image acquired by an ultrasound scanner scanning a tissue mimicking phantom submerged in water. The image boundary is marked with black lines. To show the intensity pattern of ultrasound data, the figure includes two planar sections (one of them passes through the electrode axis).

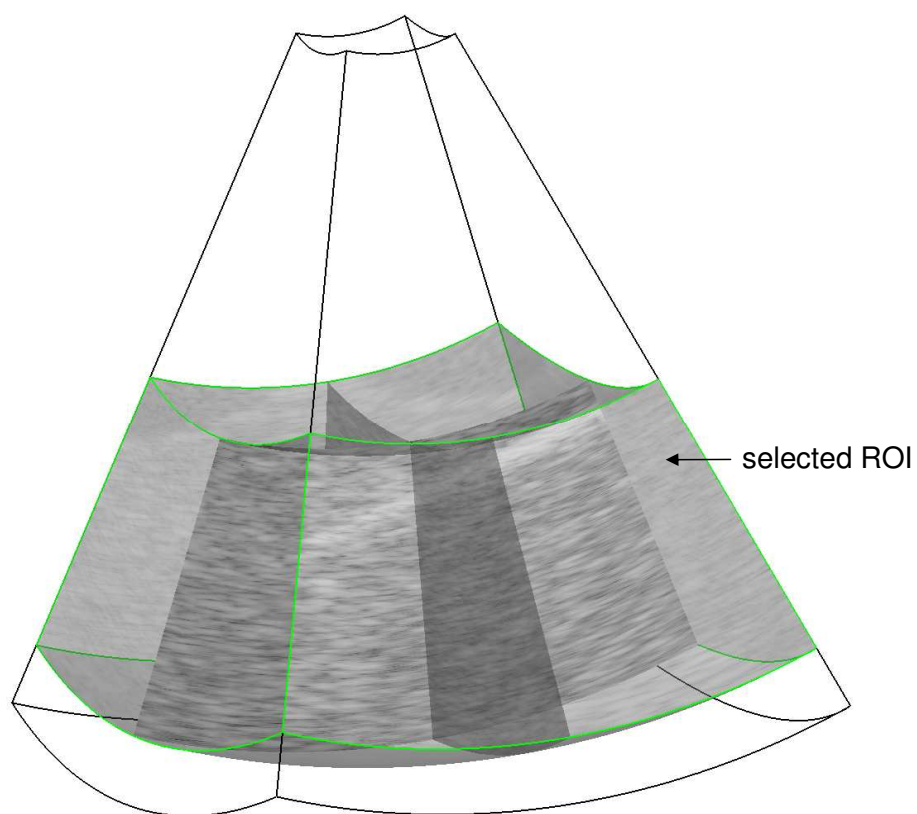


Figure 5.2: *The region of interest (delineated by green lines) is selected and processed by the localization algorithm.*

reason that the electrode is represented by a set of voxels comprised inside a thin cylinder, where the intensity is much higher compared to the intensity of tissue (background) voxels,

$$V(\mathbf{x}_e) \gg V(\mathbf{x}_b), \quad (5.2)$$

where \mathbf{x}_e , resp., \mathbf{x}_b is an electrode, resp., background voxel.

5.3 Decomposition of the localization task

The task of electrode localization is decomposed in two subtasks. First, a spatial curve that approximates the true electrode axis shall be found. To solve this problem, two approaches were implemented and experimentally verified. The principle of the first one is explained in Chapter 6. It is based on the parallel projection and assumes that the electrode axis can be approximated with a line. A more general method for localization of an electrode with a curved axis is introduced in Chapter 7. It exploits model fitting combined with the R-RANSAC estimator and downhill simplex optimization. The second subtask consists of the localization of a point that corresponds to the electrode tip, see Chapter 8.

Chapter 6

Axis localization with PIP transform

This chapter introduces an algorithm that permits to determine the axis of a thin electrode in a 3D ultrasound image [89, 90, 91]. We assume that the electrode axis is straight and the length is much greater than the diameter. Using these assumptions, the axis is found through the operation of parallel projection. Unlike the method introduced by Ding in [81], we formalize the projection into the form of a Parallel Integral Projection transform and show that the electrode axis can be found by maximizing the PIP transformation of the original image. The maximization is accelerated by means of a hierarchical mesh-grid algorithm.

6.1 Parallel Integral Projection transform

We defined the Parallel Integral Projection transform as a mapping that transforms an image function $V: \mathbb{R}^3 \rightarrow \mathbb{R}$ representing a volume image to a function $\mathcal{P}_V: \mathbb{R}^4 \rightarrow \mathbb{R}$ that describes its projections as a function of the displacement parameters u, v and angular parameters α, β , see Figure 6.1. More formally, the PIP transformation \mathcal{P}_V of $V: \mathbb{R}^3 \rightarrow \mathbb{R}$ is defined by an integral along a line with an incident point $Q = [u, v]$ and a directional vector \mathbf{w} determined by α, β :

$$\mathcal{P}_V(u, v, \alpha, \beta) = \int_{-\infty}^{\infty} V(\mathbf{R}(\alpha, \beta) \cdot (u, v, \tau)^\top) d\tau, \quad (6.1)$$

where

$$\mathbf{R}(\alpha, \beta) = \begin{pmatrix} \cos \beta & \sin \alpha \sin \beta & -\cos \alpha \sin \beta \\ 0 & \cos \alpha & \sin \alpha \\ \sin \beta & -\sin \alpha \cos \beta & \cos \alpha \cos \beta \end{pmatrix} \quad (6.2)$$

is the rotation matrix representing a rotation around the x -axis by the angle α and around the y -axis by the angle β . Note the similarity between the PIP and the Radon transform [92, 93, 94] used in Computed Tomography.

The PIP transform can be used to identify the axis of a thin electrode in a 3D image. Let $V: \mathbb{R}^3 \rightarrow \mathbb{R}$ be an image function such that

$$V(\mathbf{x}) = \begin{cases} 1; & \forall \mathbf{x} \in \mathbf{M}, \\ 0; & \forall \mathbf{x} \notin \mathbf{M}, \end{cases} \quad (6.3)$$

where $\mathbf{M} \subset \mathbb{R}^3$ is the interior of a cylinder that marks the electrode boundary, see Figure 6.2. In case the electrode diameter is infinitely small, the PIP transformation \mathcal{P}_V has the maximum

$$(u_{max}, v_{max}, \alpha_{max}, \beta_{max}) = \operatorname{argmax} \mathcal{P}_V(u, v, \alpha, \beta), \quad (6.4)$$

when the line of integration is coincident with the axis of \mathbf{M} ; \mathcal{P}_V is equal to zero elsewhere. Given the point $(u_{max}, v_{max}, \alpha_{max}, \beta_{max})$, where the PIP is maximized, the parametric equation $c(t)$ of the electrode axis is consequently given by

$$c(t) = \mathbf{R}(\alpha_{max}, \beta_{max}) \cdot (u_{max}, v_{max}, t)^\top; \quad \forall t \in \mathbb{R}. \quad (6.5)$$

6.2 Discretization of the PIP transformation

We shall maximize the PIP transformation on a discrete grid. The discretization steps $\Delta_\alpha, \Delta_\beta, \Delta_u, \Delta_v$ must be sufficiently fine not to miss the electrode. They are set such that

$$\Delta_\alpha, \Delta_\beta \leq 2 \arctan \frac{d}{2 \|\mathbf{x}_{max}\|}, \quad (6.6)$$

$$\Delta_u, \Delta_v \leq d, \quad (6.7)$$

where d is the electrode diameter and \mathbf{x}_{max} is the position of the most distant voxel from the origin. The motivation comes from the requirement that at least one integration line passes through the electrode, see Figure 6.3.

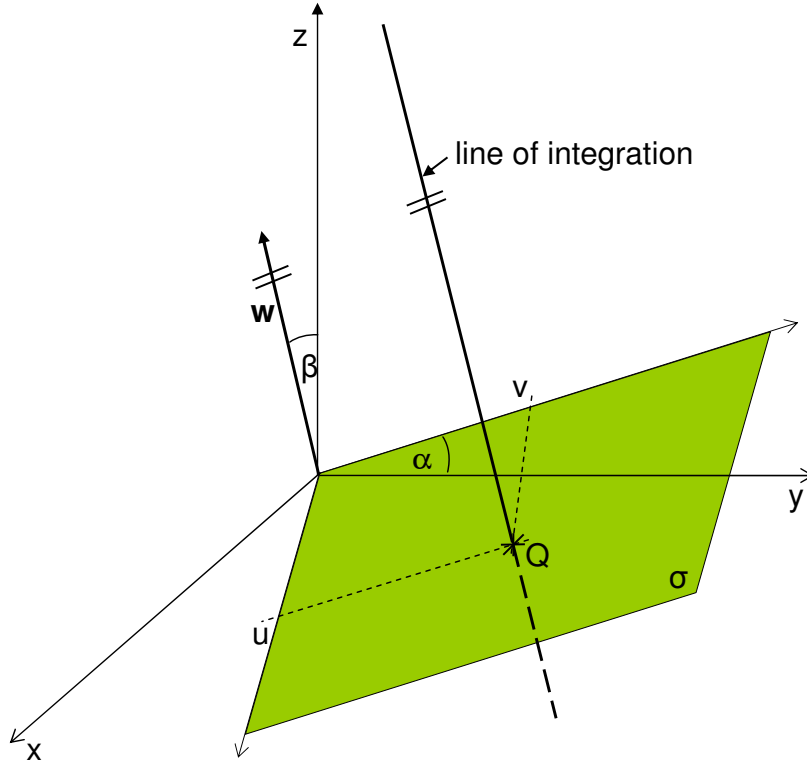


Figure 6.1: The integral of the image function $V: \mathbb{R}^3 \rightarrow \mathbb{R}$ in Equation (6.1) is calculated along a line given by the point $Q = [u, v]$ and the directional vector \mathbf{w} .

The definition integral of \mathcal{P}_V (Equation (6.1)) is evaluated numerically. Each integration line is sampled with a sampling step corresponding to the axial resolution of the ultrasound system and the integral is computed using the trapezoid rule.

6.3 Maximizing the PIP transformation

Let us define a function

$$\mathcal{A}(\alpha, \beta) = \max_{u, v} \mathcal{P}_V(u, v, \alpha, \beta), \quad (6.8)$$

that will be referred to as the angle function. Angular parameters $\alpha_{max}, \beta_{max}$ maximizing $\mathcal{A}(\alpha, \beta)$ also maximize $\mathcal{P}_V(u, v, \alpha, \beta)$ for some u_{max}, v_{max} ,

$$\exists u_{max}, v_{max} : (u_{max}, v_{max}, \alpha_{max}, \beta_{max}) = \operatorname{argmax} \mathcal{P}_V \Leftrightarrow (\alpha_{max}, \beta_{max}) = \operatorname{argmax} \mathcal{A}. \quad (6.9)$$

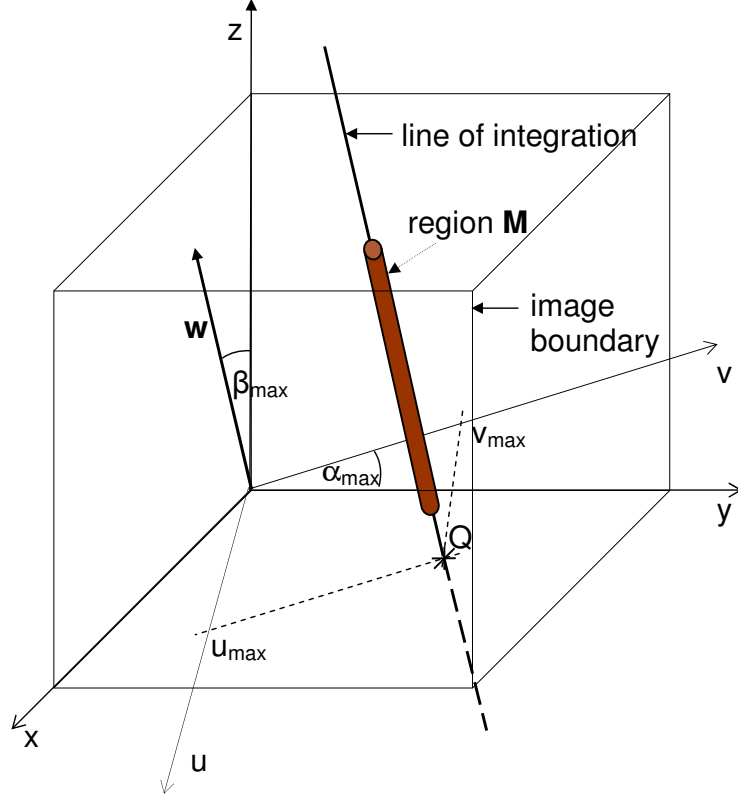


Figure 6.2: Computing the PIP transformation \mathcal{P}_V of an image function V . The electrode boundary is represented by a cylinder M . In this particular configuration, \mathcal{P}_V is maximized since the line of integration is identical with the electrode axis.

To find the value of the angle function \mathcal{A} for given α, β , we find the circumscribed rectangle $\langle u_1, u_2 \rangle \times \langle v_1, v_2 \rangle$ of the parallel projection of the image boundary on the plane σ with normal vector $\mathbf{w} = \mathbb{R}(\alpha, \beta) \cdot (1, 0, 0)^\top$ as

$$\begin{aligned} u_1 &= \min_{\mathbf{x} \in \mathcal{X}} (\mathbf{R}^{-1}(\alpha, \beta) \cdot \mathbf{x}) \cdot \mathbf{e}_x, & u_2 &= \max_{\mathbf{x} \in \mathcal{X}} (\mathbf{R}^{-1}(\alpha, \beta) \cdot \mathbf{x}) \cdot \mathbf{e}_x, \\ v_1 &= \min_{\mathbf{x} \in \mathcal{X}} (\mathbf{R}^{-1}(\alpha, \beta) \cdot \mathbf{x}) \cdot \mathbf{e}_y, & v_2 &= \max_{\mathbf{x} \in \mathcal{X}} (\mathbf{R}^{-1}(\alpha, \beta) \cdot \mathbf{x}) \cdot \mathbf{e}_y, \end{aligned}$$

where \mathcal{X} is a set of voxel coordinates and $\mathbf{e}_x, \mathbf{e}_y$ are the unit vectors in the Cartesian coordinate system, see Figure 6.4. The integral in Equation (6.1) is evaluated at a grid of points u, v uniformly distributed on the rectangle $\langle u_1, u_2 \rangle \times \langle v_1, v_2 \rangle$ with steps Δ_u, Δ_v satisfying Equation (6.7). The value of \mathcal{A} is the maximum of \mathcal{P}_V exhaustively evaluated on the grid with fixed α, β .

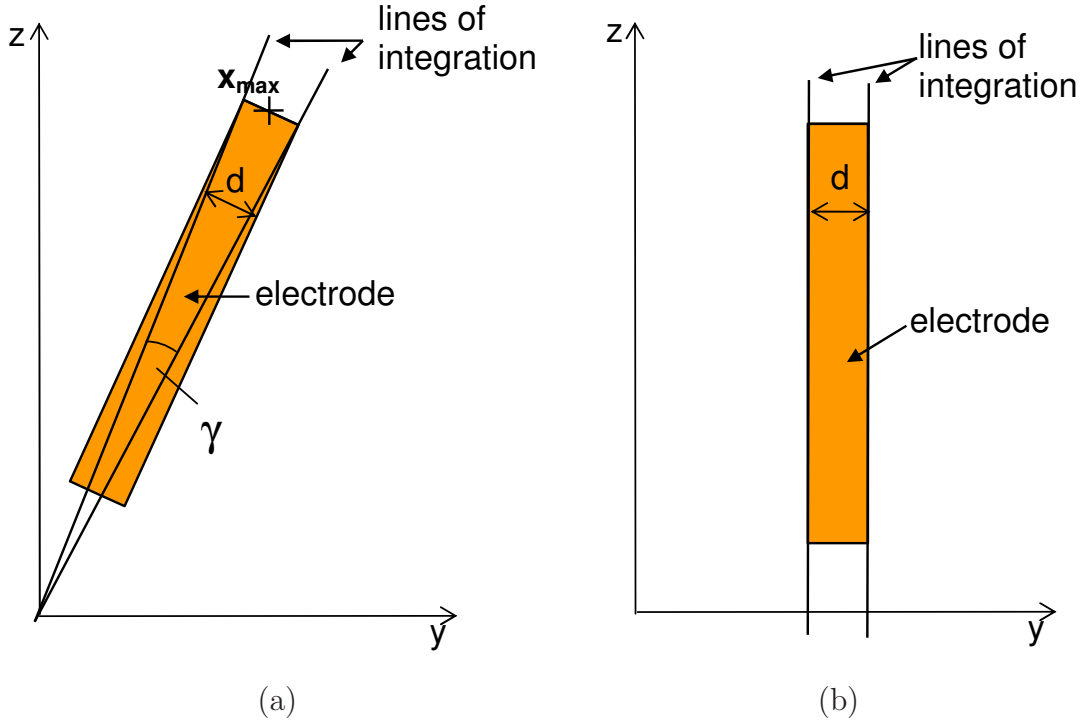


Figure 6.3: (a) Discretization of the angular parameters α , β . If two lines of integration incline at angle γ for which Equation (6.6) holds then at least one of the line intersects the electrode along the length. (b) Discretization of the displacement parameters u , v . Assuming two parallel lines of integration, the displacement must be less than the electrode diameter d , so that the electrode comprises at least one line of integration.

We shall now find values $\alpha_{\max}, \beta_{\max}$ that maximize the angle function $\mathcal{A}(\alpha, \beta)$,

$$(\alpha_{\max}, \beta_{\max}) = \operatorname{argmax} \mathcal{A}(\alpha, \beta). \quad (6.10)$$

Two approaches to the maximization have been tested: (i) the exhaustive search and (ii) the hierarchical mesh-grid search.

6.3.1 Exhaustive search

Due to the periodicity of the PIP transform in α, β , it suffices to maximize the angle function on the square grid $\langle 0, 180 \rangle \times \langle 0, 180 \rangle$. This grid is uniformly sampled with discretization steps $\Delta_\alpha, \Delta_\beta$ satisfying Equation (6.6) and the angle function \mathcal{A} is evaluated in each node of the grid, see Figure 6.6 for example.

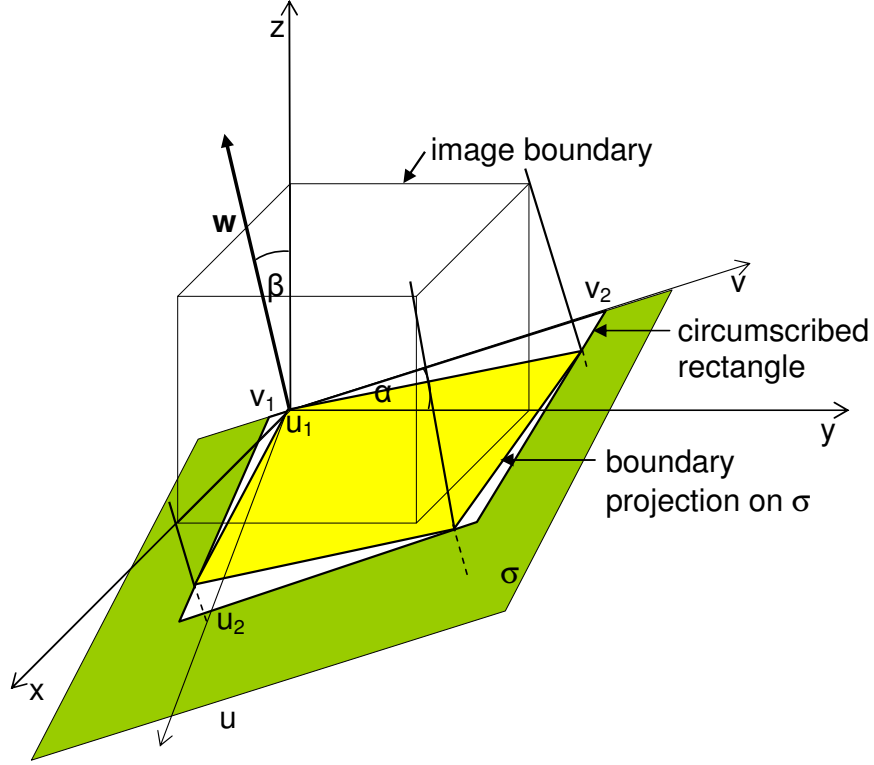


Figure 6.4: *Evaluation of the angle function \mathcal{A} . 3D image boundary is projected on the plane σ and a circumscribed rectangle comprising the projection is determined. The rectangle is uniformly sampled with Δ_u, Δ_v and the value of $\mathcal{A}(\alpha, \beta)$ is equal to the maximum of $\mathcal{P}_V(\alpha, \beta, u, v)$ evaluated on the grid with fixed α, β .*

6.3.2 Hierarchical mesh-grid search

The main drawback of the exhaustive search is its computational complexity. In order to accelerate the maximization of \mathcal{A} , we propose to use a coarse-to-fine hierarchical mesh-grid search method [95]. On the first level, \mathcal{A} is evaluated on the rectangular grid of points $\langle 0, 180 \rangle \times \langle 0, 180 \rangle$ that are uniformly sampled with the initial sampling steps $\Delta_\alpha^{init}, \Delta_\beta^{init}$, see Figure 6.5. The maximum location $\alpha_{max}^1, \beta_{max}^1$ is determined. On the second level, the angle function is evaluated on a rectangular grid $\langle \alpha_{max}^1 - 45, \alpha_{max}^1 + 45 \rangle \times \langle \beta_{max}^1 - 45, \beta_{max}^1 + 45 \rangle$ uniformly sampled with steps $\Delta_\alpha^2 = \frac{\Delta_\alpha^{init}}{2}, \Delta_\beta^2 = \frac{\Delta_\beta^{init}}{2}$. We find $\alpha_{max}^2, \beta_{max}^2$, where \mathcal{A} is maximized. On the i -th level, the angle function is evaluated on the grid $\langle \alpha_{max}^{i-1} - \frac{180}{2^i}, \alpha_{max}^{i-1} + \frac{180}{2^i} \rangle \times \langle \beta_{max}^{i-1} - \frac{180}{2^i}, \beta_{max}^{i-1} + \frac{180}{2^i} \rangle$ with discretization steps $\Delta_\alpha^i = \frac{\Delta_\alpha^{init}}{2^{i-1}}, \Delta_\beta^i = \frac{\Delta_\beta^{init}}{2^{i-1}}$. The algorithm continues until both steps $\Delta_\alpha^i, \Delta_\beta^i$ are

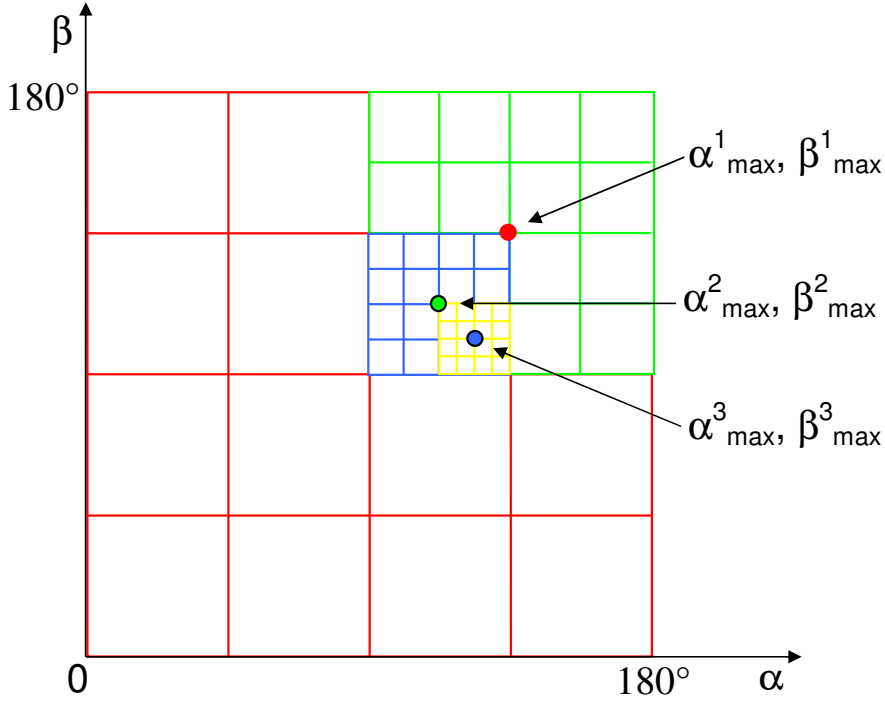


Figure 6.5: *Principle of hierarchical mesh-grid algorithm applied to the maximization of the angle function \mathcal{A} .*

equal or inferior to some predefined threshold values Δ_α^{final} , Δ_β^{final} that control the accuracy of the axis axis localization.

The hierarchical mesh-grid method was selected from existing numerical optimization methods [96], since it does not require an initial solution and can avoid to some extent getting trapped in a local extremum.

6.3.3 Comparison of the exhaustive and the hierarchical search

The main interest in using the hierarchical mesh-grid search method is to accelerate the task of the PIP maximization. Let us compare the computational efficiency of both search methods in terms of the number of evaluations of \mathcal{A} . This number is in fact influenced by the discretization parameters $\Delta_\alpha, \Delta_\beta$, resp., $\Delta_\alpha^{init}, \Delta_\beta^{init}, \Delta_\alpha^{final}, \Delta_\beta^{final}$ of the exhaustive, resp., hierarchical mesh-grid method.

Exhaustive search – To determine the maximum of the function \mathcal{A} with accuracy $\Delta_\alpha, \Delta_\beta$, the rectangle $\langle 0, 180 \rangle \times \langle 0, 180 \rangle$ is sampled along dimensions

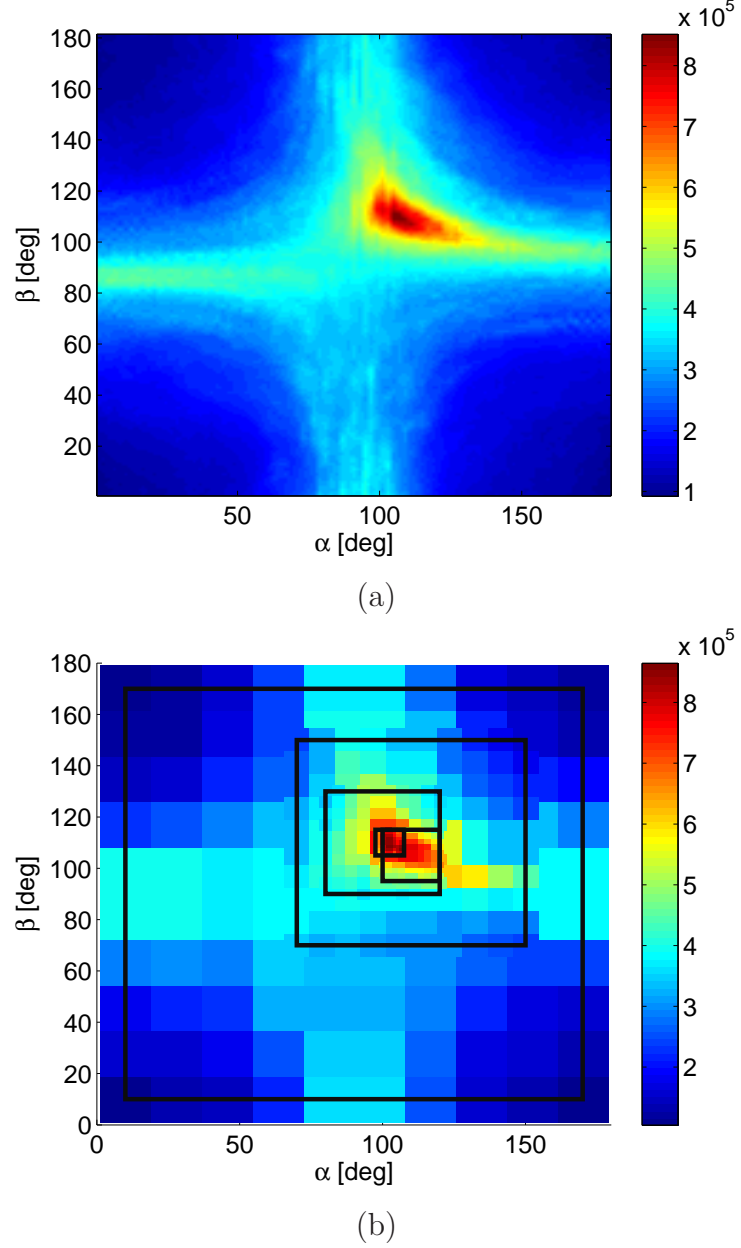


Figure 6.6: Maximization of the angle function \mathcal{A} . (a) Exhaustive search on a discrete grid $\langle 0, 180^\circ \rangle \times \langle 0, 180^\circ \rangle$ uniformly sampled with $\Delta_\alpha = \Delta_\beta = 1^\circ$; (b) five-level hierarchical mesh-grid maximization with initial $\Delta_\alpha^{init} = \Delta_\beta^{init} = 16^\circ$ and final discretization steps $\Delta_\alpha^{final} = \Delta_\beta^{final} = 1^\circ$. The region of search size and discretization steps $\Delta_\alpha, \Delta_\beta$ are gradually decreased by the factor of 2. Black rectangles in the figure delineate the region of search on each level.

α , resp., β dimension with the step Δ_α , resp., Δ_β . The total number of the angle function evaluations N_{exh} is given by

$$N_{\text{exh}} = \frac{180}{\Delta_\alpha} \cdot \frac{180}{\Delta_\beta} \quad (6.11)$$

Hierarchical mesh-grid search – On each level, the discretization steps are divided by the factor of 2. Given the initial $\Delta_\alpha^{\text{init}}$, $\Delta_\beta^{\text{init}}$ and final steps $\Delta_\alpha^{\text{final}}$, $\Delta_\beta^{\text{final}}$, the number of levels is

$$\max \left\{ \log_2 \frac{2\Delta_\alpha^{\text{init}}}{\Delta_\alpha^{\text{final}}}, \log_2 \frac{2\Delta_\beta^{\text{init}}}{\Delta_\beta^{\text{final}}} \right\}. \quad (6.12)$$

There are $\left(\frac{180}{\Delta_\alpha^{\text{init}}} \cdot \frac{180}{\Delta_\beta^{\text{init}}} \right)$ evaluations on each level, so the total number of the function \mathcal{A} evaluations performed by the hierarchical mesh-grid method is

$$N_{\text{hier}} = \left(\frac{180}{\Delta_\alpha^{\text{init}}} \cdot \frac{180}{\Delta_\beta^{\text{init}}} \right) \cdot \max \left\{ \log_2 \frac{2\Delta_\alpha^{\text{init}}}{\Delta_\alpha^{\text{final}}}, \log_2 \frac{2\Delta_\beta^{\text{init}}}{\Delta_\beta^{\text{final}}} \right\}. \quad (6.13)$$

In order to simplify the comparison, the discretization of the angular parameters of both methods are assumed to be equal: $\Delta_\alpha = \Delta_\beta = \Delta_{\text{exh}}$, $\Delta_\alpha^{\text{init}} = \Delta_\beta^{\text{init}} = \Delta^{\text{init}}$, $\Delta_\alpha^{\text{final}} = \Delta_\beta^{\text{final}} = \Delta^{\text{final}}$. Further, we let $\Delta_{\text{exh}} = \Delta^{\text{final}}$, so that the localization accuracy achieved by both methods is the same. Figure 6.7 shows the number of evaluations of \mathcal{A} as a function of $\Delta_{\text{exh}}, \Delta^{\text{final}}$, where Δ^{init} is used as a parameter. We can observe that using a hierarchical mesh-grid method leads to significant decrease in computational cost.

6.4 Discretization parameters vs. accuracy

The accuracy of the localization is controlled by the final angular $\Delta_\alpha^{\text{final}}, \Delta_\beta^{\text{final}}$ and the displacement Δ_u, Δ_v step parameters whose theoretical values are given by Equations (6.6), (6.7). The influence of their settings on the accuracy was verified empirically as well. Using the procedure describe in Section 9.2.1, we simulated a 3D image representing a tissue region of 50x50x30 mm containing an electrode with 0.3 mm in diameter and 20 mm in length. The localization accuracy was quantified with the parameter $\varepsilon_{\text{axis}}$, see Equation (9.6).

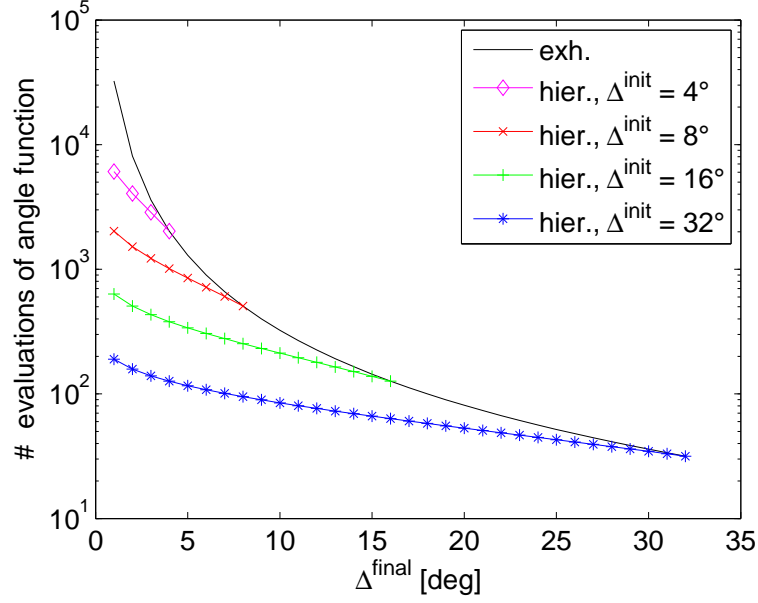


Figure 6.7: Comparison of the number of evaluations of \mathcal{A} as a function of discretization steps $\Delta_{exh} = \Delta^{final}$ for exhaustive and hierarchical mesh-grid search.

6.4.1 Influence of the final angular steps $\Delta_{\alpha}^{final}, \Delta_{\beta}^{final}$

The accuracy of the PIP method is good if the angular step parameters $\Delta_{\alpha}^{final}, \Delta_{\beta}^{final}$ are small. However, this leads to an increase in the computational time (Figure 6.8). To find the optimum values of $\Delta_{\alpha}^{final}, \Delta_{\beta}^{final}$, we performed several tests on the simulated image. The electrode axis position was estimated by the algorithm while varying $\Delta_{\alpha}^{final}, \Delta_{\beta}^{final}$ from 0.125° to 32° . Other parameters were constant: $\Delta_{\alpha}^{init} = \Delta_{\beta}^{init} = 32^{\circ}$ and $\Delta_u = \Delta_v = 0.2$ mm.

Figure 6.9 illustrates the axis localization accuracy ε_{axis} as a function of $\Delta_{\alpha}^{final}, \Delta_{\beta}^{final}$. We conclude that decreasing this parameter under 1° leads to an increase in computational time without further improvement in the axis accuracy. Therefore, we set $\Delta_{\alpha}^{final}, \Delta_{\beta}^{final}$ to 1° .

6.4.2 Influence of the displacement steps Δ_u, Δ_v

The displacement parameters Δ_u, Δ_v control the distance between adjacent lines of integration. While decreasing these parameters improves the accuracy, it increases the computational time (Figure 6.10). The same simulated image as in Section 6.4.1 was used to experimentally determine optimum values of Δ_u, Δ_v . The

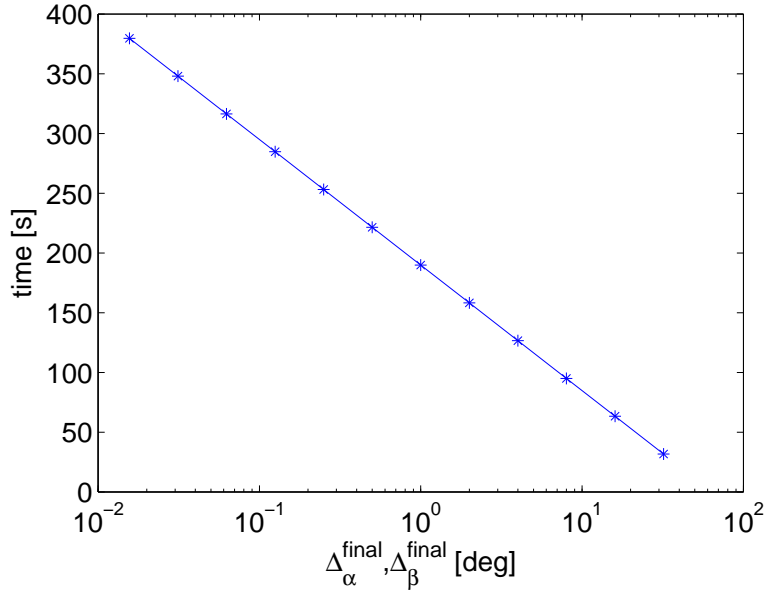


Figure 6.8: Time required to maximize the PIP transformation for various values of $\Delta_\alpha^{\text{final}}, \Delta_\beta^{\text{final}}$ with other parameters set to constant.

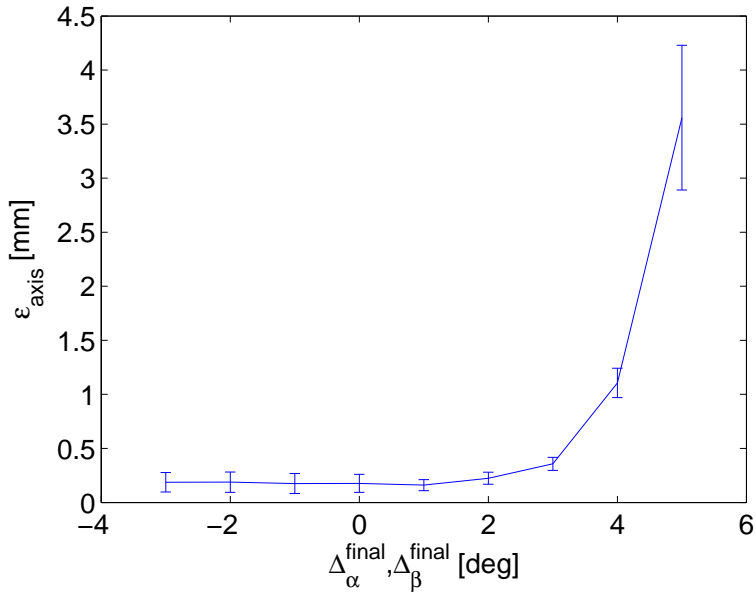


Figure 6.9: Achieved localization accuracy $\varepsilon_{\text{axis}}$ for different values of final angular steps $\Delta_\alpha^{\text{final}}, \Delta_\beta^{\text{final}}$.

localization algorithm was executed several times with fixed parameters $\Delta_\alpha^{init} = \Delta_\beta^{init} = 32^\circ$, $\Delta_\alpha^{final} = \Delta_\beta^{final} = 1^\circ$ and the displacement steps Δ_u, Δ_v were varied from 0.0625 to 2 mm.

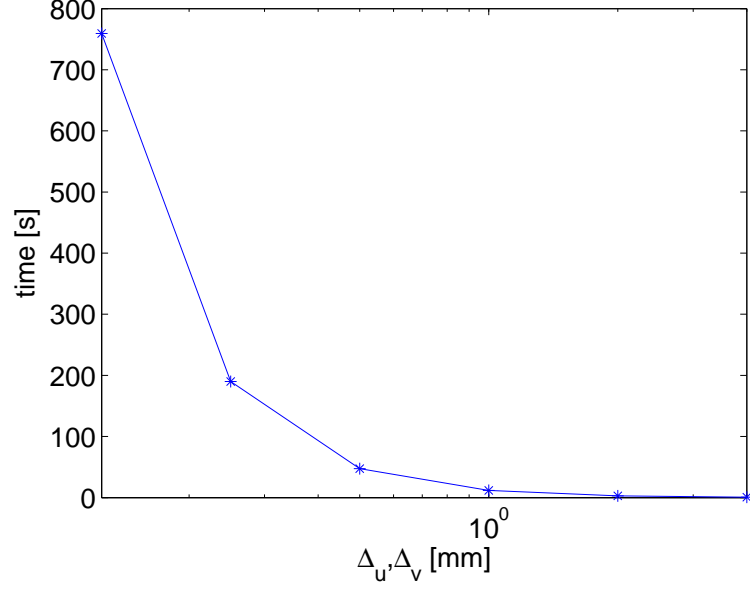


Figure 6.10: *Time required to maximize the PIP transformation for various values of Δ_u, Δ_v with other parameters set to constant.*

Figure 6.11 depicts the calculated axis accuracy ε_{axis} as a function of the displacement steps Δ_u, Δ_v . It shows that when Δ_u, Δ_v exceeds 0.25 mm, the mean and standard deviation of error in axis localization increases rapidly. We propose to set Δ_u, Δ_v to 0.2 mm.

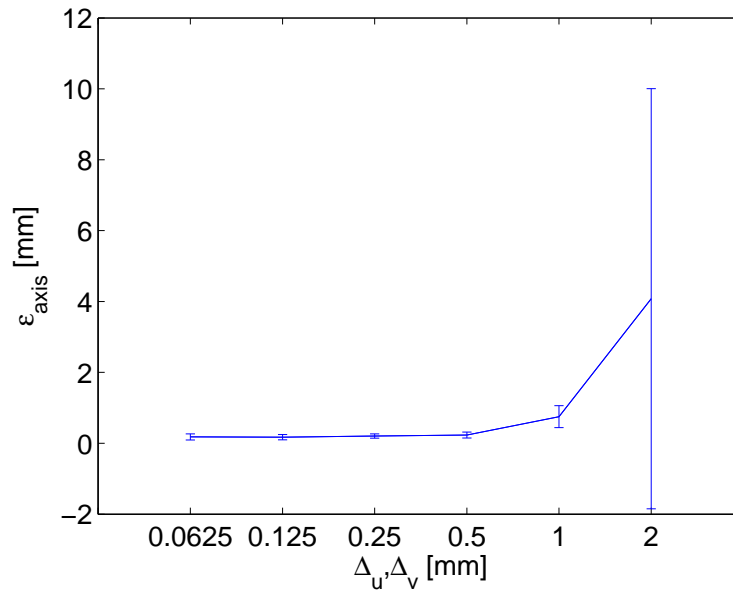


Figure 6.11: *Axis localization accuracy ε_{axis} as a function of the displacement steps Δ_u, Δ_v .*

Chapter 7

Axis localization with model fitting

This chapter presents an algorithm that permits to determine the axis of a curved electrode in a 3D image [97, 98, 91]. We assume that the axis can be approximated by a parametric cubic curve. To decrease the computational time, the voxels are initially pre-segmented using thresholding (Section 7.1). The axis localization is based on the model fitting paradigm. Three different models are proposed to describe the electrode shape and the intensity distribution (Section 7.2). Their parameters are estimated by the R-RANSAC estimator (Section 7.3). To improve the localization accuracy, an optimization step using the downhill simplex method is used (Section 7.4).

7.1 Segmentation

Because of the strong reflection of ultrasound energy on the boundary between tissue and electrode, the electrode voxels are much brighter than background voxels. We exploit this hypothesis to classify the voxels \mathcal{X} in two disjoint sets \mathcal{X}_e (electrode voxels) and \mathcal{X}_b (background voxels). The goal of this operation is to substantially reduce the number of voxels that are going to be further processed and thus to decrease the computational load of the electrode localization task.

The intensity based voxel classification is given by

$$\forall \mathbf{x} \in \mathcal{X} : \mathbf{x} \in \begin{cases} \mathcal{X}_e; & V(\mathbf{x}) \geq T_I \\ \mathcal{X}_b; & V(\mathbf{x}) < T_I \end{cases}, \quad (7.1)$$

distribution model	MISE
Normal	$7.91 \cdot 10^{-2}$
Log-normal	$2.18 \cdot 10^{-2}$
Rayleigh	$4.17 \cdot 10^{-2}$
Gamma	$4.62 \cdot 10^{-4}$

Table 7.1: *The comparison of the intensity distribution models using the MISE criterion.*

where T_I is a constant threshold that was determined by the procedure discussed in the following subsection.

7.1.1 Estimating optimal threshold T_I

The characteristics of the classification given by Equation (7.1) depend on the choice of T_I . For overly small T_I , \mathcal{X}_e would contain a large number of false positives (background voxels); whereas for exceedingly large T_I , only a small number of electrode voxels would be assigned to \mathcal{X}_e .

The optimal value of T_I was deduced from the estimated statistical model that describes the voxel intensities. The model parameters were estimated using a training set of five ultrasound images $V^i: \mathcal{X}^i \rightarrow \mathcal{I}^i; i = 1, \dots, 5$ acquired by scanning a portion of tissue containing an electrode. A number of intensity distribution models were proposed in the literature. They were summarized in Chapter 4.1. In order to select the correct statistical model, we verified four distribution models: Normal, Log-normal, Rayleigh and Gamma, see Figure 7.1.

The parameters of the intensity models were estimated to fit them into the set $\bigcup_{i=1}^5 \mathcal{I}^i$, which represents all intensity values of the training images. The selection of the best model was performed based on the mean integrated square error (MISE) that is given by

$$\text{MISE} = \int_{I \in \mathbb{R}} \left[P(I) - \hat{P}(I) \right]^2 dI, \quad (7.2)$$

where $\hat{P}(I)$ is the estimated intensity distribution and $P(I)$ is the true intensity distribution that was substituted by the histogram.

The result of the comparison is summarized in Table 7.1, which shows the MISE value of each model. We can observe that the Gamma distribution approximates the best the intensity histogram and thus it was selected as the intensity model.

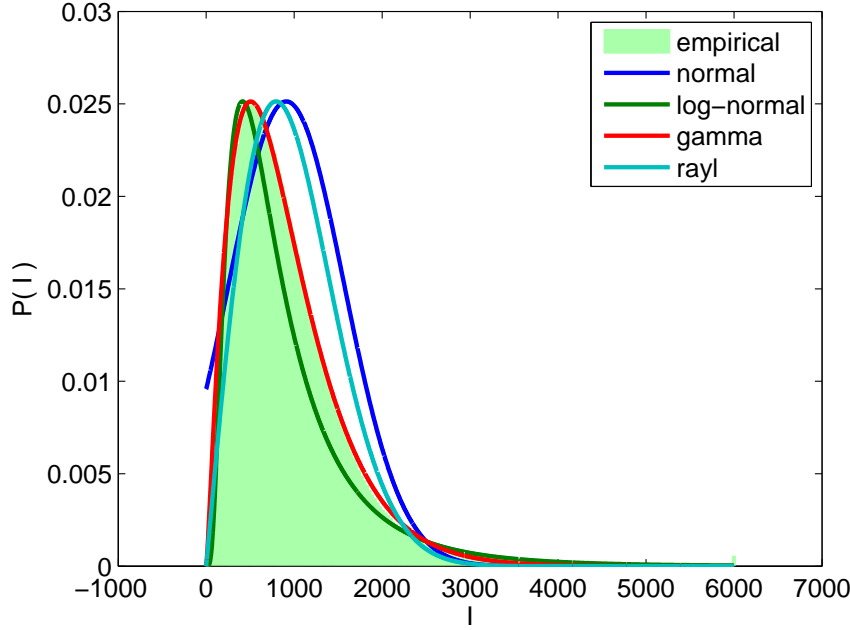


Figure 7.1: *Statistical models of the intensity distribution. The parameters of four probability distributions were estimated to fit the intensity of training images. Comparing each of them with the histogram, we note that the Gamma distribution approximates the best the probability distribution of voxel intensity.*

The Gamma distribution is defined by

$$P(I) = I^{\psi-1} \frac{e^{-\frac{I}{\xi}}}{\xi^{\psi} \Gamma(\psi)}; \quad \forall I > 0, \quad (7.3)$$

where $\psi > 0$ is the shape parameter and $\xi > 0$ is the scale parameter. They are found as the maximum likelihood estimates [99] from the intensity of voxels:

$$\tau = \ln \left(\frac{1}{|\mathcal{X}|} \sum_{\mathbf{x} \in \mathcal{X}} V(\mathbf{x}) \right) - \frac{1}{|\mathcal{X}|} \sum_{\mathbf{x} \in \mathcal{X}} \ln(V(\mathbf{x})), \quad (7.4)$$

$$\psi = \frac{3 - \tau + \sqrt{(\tau - 3)^2 + 24\tau}}{12\tau}, \quad (7.5)$$

$$\xi = \frac{1}{\psi |\mathcal{X}|} \sum_{\mathbf{x} \in \mathcal{X}} V(\mathbf{x}). \quad (7.6)$$

To determine T_I , we used the cumulative distribution $F(I)$ of the estimated

Gamma distribution (Figure 7.2) which is given by

$$F(I) = \int_0^I P_I(\tau) d\tau. \quad (7.7)$$

The electrode dimensions are much smaller than the volume corresponding to the field of view. Comparing the number of background voxels to the number of electrode voxels, we set T_I equal to the 95% quantile of $F(I)$, see Figure 7.2.

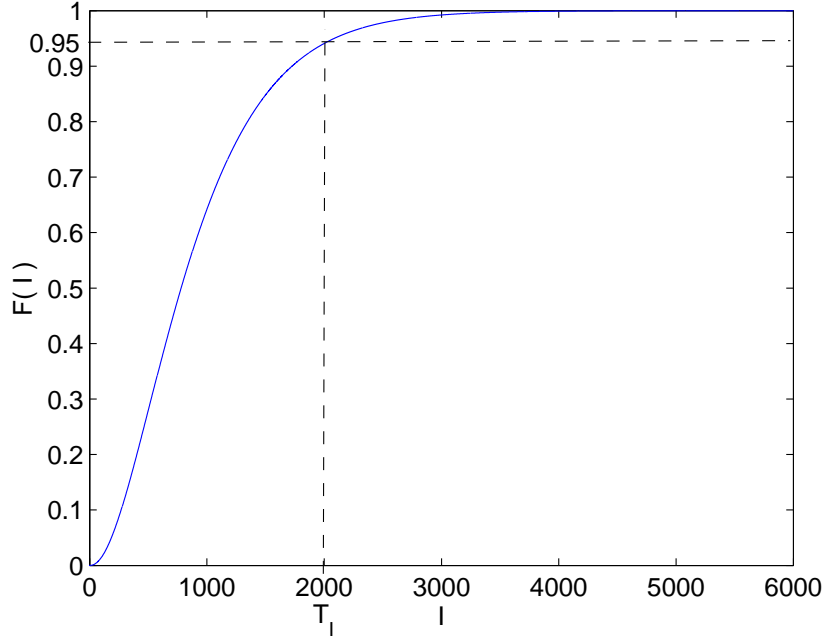


Figure 7.2: *Cumulative distribution function of the fitted Gamma distribution was used to determine the threshold T_I as the 95% quantile.*

7.2 Shape and intensity models of the electrode

Due to the speckle noise, the set of electrode voxels \mathcal{X}_e contains a small portion of voxels that belong to the background (outliers). To distinguish electrode voxels from outliers contained in \mathcal{X}_e , a model fitting is proposed. In the next subsections, we provide a description of three models that describe the characteristics (e.g., shape and intensity priors) of the electrode in 3D ultrasound images. For each model, a cost function is established to quantify how well the model of the electrode fits the voxels \mathcal{X}_e . The models are defined by a set of parameters which are

estimated to minimize the cost function, see Sections 7.3, 7.4. This approach permits to identify electrode voxels among outliers and it simultaneously finds the electrode position in a parametric form.

7.2.1 Model I – Axis shape

The diameter of electrodes used in surgical applications is small to reduce the invasiveness of the procedure. However, this makes the electrode flexible. If such electrode encounters a rigid tissue structure, it may bend slightly. As a consequence the electrode appears in the image as an elongated, symmetric, bright object with a curved axis. To allow the localization of such an object, we propose a model that describes the curved electrode axis with a curve. The model-fitting-axis-localization algorithm that makes use of this model will be referred to by MF1.

Curves can be given by an implicit or a parametric representation. While implicit curves can describe a wide range of curves, many of its important properties (e.g., parameter extraction, visualization) are difficult to compute. We shall describe the electrode axis with a spatial, parametric cubic curve $c(t; \mathbf{H}): \mathbb{R} \rightarrow \mathbb{R}^3$ given by

$$c(t; \mathbf{H}) = \underbrace{\begin{pmatrix} h_{11} & h_{12} & h_{13} & h_{14} \\ h_{21} & h_{22} & h_{23} & h_{24} \\ h_{31} & h_{32} & h_{33} & h_{34} \end{pmatrix}}_{\mathbf{H}} \cdot \begin{pmatrix} 1 \\ t \\ t^2 \\ t^3 \end{pmatrix}; \quad t \in \mathbb{R}, \quad (7.8)$$

where \mathbf{H} is a matrix of curve coefficients and t is a curve parameter. The curve order was set to 3, because curves of lower order commonly have little flexibility, whereas curves of higher order are usually overly complex and tend to introduce undesirable oscillations.

Curve defined by control points For a given matrix of curve coefficients \mathbf{H} the curve shape and its position are fully determined. We can also define the parametric cubic curve by means of four points (denoted as the control points) that lie on the curve (Figure 7.3). Formally, let $\mathcal{D} = (D_1, D_2, D_3, D_4)$ be an ordered quadruple of control points. The task is to compute the matrix of curve coefficients \mathbf{H} , so that

$$\exists t_1, t_2, t_3, t_4 \in \mathbb{R}, t_1 < t_2 < t_3 < t_4 : \quad c(t_i; \mathbf{H}) = D_i; \quad \forall i = 1, \dots, 4. \quad (7.9)$$

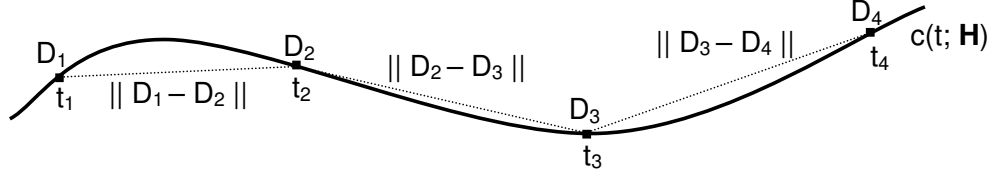


Figure 7.3: Ordered quadruple of distinct points define the coefficients of a parametric cubic curve. The curve parameter t corresponding to each point is derived from their respective Euclidean distances.

The curve parameters t_1, t_2, t_3, t_4 of the control points, which are required to determine \mathbf{H} , are not known a priori. We let $t_1 = 0$. The values of the other curve parameters t_2, t_3, t_4 are deduced from Euclidean distances between adjacent control points to approximate the true arc length parametrization,

$$t_2 = \|D_1 - D_2\|, \quad (7.10)$$

$$t_3 = t_2 + \|D_2 - D_3\|,$$

$$t_4 = t_3 + \|D_3 - D_4\|. \quad (7.11)$$

The condition imposed on the matrix \mathbf{H} can be written into the form of a matrix equation,

$$\underbrace{\begin{pmatrix} h_{11} & h_{12} & h_{13} & h_{14} \\ h_{21} & h_{22} & h_{23} & h_{24} \\ h_{31} & h_{32} & h_{33} & h_{34} \end{pmatrix}}_{\mathbf{H}} \cdot \underbrace{\begin{pmatrix} 1 & 1 & 1 & 1 \\ t_1 & t_2 & t_3 & t_4 \\ t_1^2 & t_2^2 & t_3^2 & t_4^2 \\ t_1^3 & t_2^3 & t_3^3 & t_4^3 \end{pmatrix}}_{\mathbf{T}} = \underbrace{\begin{pmatrix} D_{1,x} & D_{2,x} & D_{3,x} & D_{4,x} \\ D_{1,y} & D_{2,y} & D_{3,y} & D_{4,y} \\ D_{1,z} & D_{2,z} & D_{3,z} & D_{4,z} \end{pmatrix}}_{\mathbf{D}}, \quad (7.12)$$

where \mathbf{H} is the coefficient matrix, \mathbf{T} is the matrix of curve parameters and \mathbf{D} is composed of the coordinates of the control points. Multiplying the equation with the inverse matrix of \mathbf{T} leads to a mapping $\Omega: \mathcal{D} \rightarrow \mathbf{H}$ defined by,

$$\mathbf{H} = \mathbf{D} \cdot \mathbf{T}^{-1}, \quad (7.13)$$

which provides the sought coefficient matrix \mathbf{H} given the coordinates of control points in the matrix \mathbf{D} .

Cost function Let $V: \mathcal{X}_e \rightarrow \mathcal{I}$ be an image function restricted to the set of electrode voxels \mathcal{X}_e (Equation (7.1)). Let us further assume that \mathbf{H} is a matrix of coefficients that define a parametric cubic curve $c(t; \mathbf{H})$ approximating the electrode axis. In order to find the best model of the electrode axis, we need to establish a criterion that determines how well the curve fits the voxels \mathcal{X}_e given the curve coefficients \mathbf{H} . The implemented measure quantifying the model quality is based on the number of points consistent with the curve. We say that a point \mathbf{x} is consistent with the curve $c(t; \mathbf{H})$, if its distance to the curve $d(c(t; \mathbf{H}), \mathbf{x})$ is less than a parameter ρ (Figure 7.4),

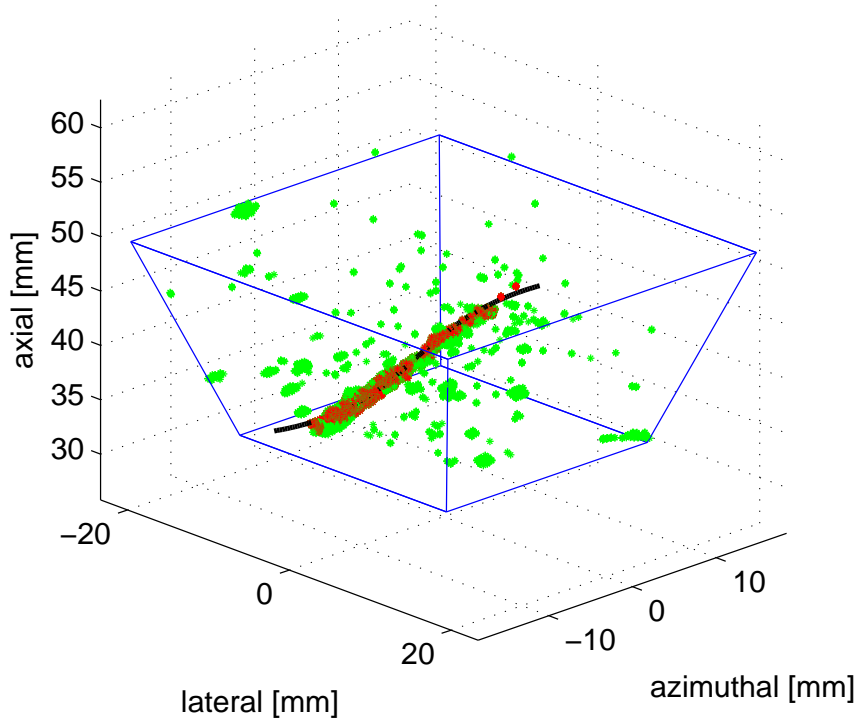


Figure 7.4: Graphical representation of points consistent with a curve. Blue line depicts the outline of selected ROI inside ultrasound image. The curve $c(t; \mathbf{H})$ that approximates the electrode axis is shown in black. The location of voxels inside the ROI is marked by points. Red points denotes voxels that are consistent with the curve for the parameter ρ set to 1 mm.

To find the model quality, the distance $d(c(t; \mathbf{H}), \mathbf{x})$ for all $\mathbf{x} \in \mathcal{X}_e$ is computed and the number of consistent voxels is determined. The quality criterion or the

model cost, $C(\mathbf{H})$ is defined as the negative of the number of consistent points,

$$C(\mathbf{H}) = -|\{\mathbf{x} \in \mathcal{X}_e : d(c(t; \mathbf{H}), \mathbf{x}) \leq \rho\}|. \quad (7.14)$$

The curve $c(t; \mathbf{H}^*)$ that minimizes $C(\mathbf{H})$ is selected as the model that best approximates the electrode axis,

$$\mathbf{H}^* = \underset{\mathbf{H} \in \mathbb{R}^{12}}{\operatorname{argmin}} C(\mathbf{H}). \quad (7.15)$$

Computing the point-to-curve distance To compute the model quality, the distance $d(c(t; \mathbf{H}), X)$ of a point X from a parametric cubic curve $c(t; \mathbf{H})$ must be found. We define it as the Euclidean distance between the point X and the closest point that is incident with the curve,

$$d(c(t; \mathbf{H}), X) = \min_{t \in \mathbb{R}} \|c(t; \mathbf{H}) - X\|. \quad (7.16)$$

The minimization task, however, leads to calculating the roots of a polynomial equation of the fifth degree that requires to apply an iterative numerical method. Although the set \mathcal{X}_e contains only 5% of the initial number of voxels, evaluating the distance over all voxels in \mathcal{X}_e would markedly increase the computational time. In order to avoid this problem, we implemented an approximation of the point-to-curve distance. Let $\mathcal{D} = (D_1, D_2, D_3, D_4)$ be the control points of $c(t; \mathbf{H})$ and t_1, t_2, t_3, t_4 curve parameters such that $c(t_i; \mathbf{H}) = D_i, i = 1, \dots, 4$. A least mean square line $l(s; L, \mathbf{u})$ is fitted the control points (Figure 7.5). The control point coordinates are used to compute the line point L as the coordinate mean,

$$L = \frac{1}{4} \begin{pmatrix} \sum_{i=1}^4 D_{i,x} \\ \sum_{i=1}^4 D_{i,y} \\ \sum_{i=1}^4 D_{i,z} \end{pmatrix}, \quad (7.17)$$

where $D_{i,x}, D_{i,y}, D_{i,z}$ is the x, y, z coordinate of i -th control point. The unit directional vector \mathbf{u} is determined as the maximal eigenvector (in the sense of corresponding eigenvalue) of the coordinate covariance matrix. Line parameters s_{D_1}, s_{D_4}, s_X of the projections of D_1, D_4, X on the line are computed,

$$s_{D_1} = (D_1 - L) \cdot \mathbf{u}, s_{D_4} = (D_4 - L) \cdot \mathbf{u}, s_X = (X - L) \cdot \mathbf{u}. \quad (7.18)$$

We establish a linear relation between s and t that maps $\langle s_{D_1}, s_{D_4} \rangle \rightarrow \langle t_1, t_4 \rangle$. The objective is to ensure that the distance of a point whose projection on the line

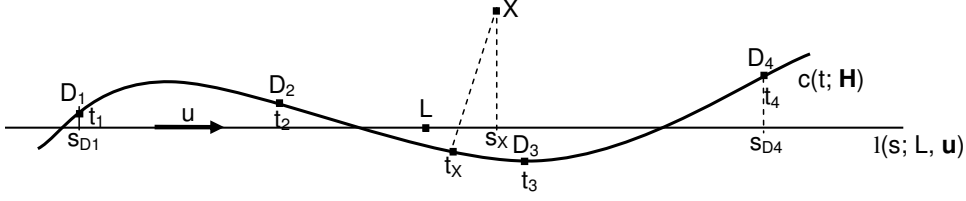


Figure 7.5: Approximation of the curve $c(t; \mathbf{H})$ to the point X distance exploits a least mean square line fitted the curve control points. The curve-to-point distance is computed as the Euclidean distance between the point X and a curve point $c(t_X; \mathbf{H})$ determined from the projection of X on the line.

lies between $l(s_{D_1}; L, \mathbf{u})$ and $l(s_{D_4}; L, \mathbf{u})$, is computed from a curve point located between D_1 and D_4 . Using this function, we compute the curve parameter t_X

$$t_X = \frac{t_4 - t_1}{s_{D_4} - s_{D_1}} \cdot (s_X - s_{D_1}) + t_1, \quad (7.19)$$

that determines a curve point $c(t_X; \mathbf{H})$. Its Euclidean distance from the point X is used to approximate $d(c(t; \mathbf{H}), X)$,

$$d(c(t; \mathbf{H}), X) \approx \|c(t_X; \mathbf{H}) - X\|. \quad (7.20)$$

7.2.2 Model II – Axis shape and intensity priors

Model I and the cost function used to evaluate its quality considers solely the position of voxels \mathcal{X}_e , disregarding their intensity. To exploit the prior information about the intensity distribution of voxels located near the electrode, a second model is proposed. It is composed of the shape model introduced in Model I. Second part of the model incorporates a probability distribution that models the intensity of a voxel located at a certain distance from the axis. The model cost is evaluated from the likelihood that voxels with given intensities fit estimated intensity priors. The model-fitting-axis-localization algorithm that makes use of this model will be referred to by MF2.

The intensity priors were a priori found using a training set of five ultrasound images $V^i: \mathcal{X}^i \rightarrow \mathcal{I}^i, i = 1, \dots, 5$. acquired by scanning a portion of tissue containing an electrode. The electrode axis in this setup was straight without any geometrical distortion. In each image V^i , two points E_I^i, E_T^i on the electrode axis were manually selected. They corresponded to the intercept point of the electrode

with the FOV and the electrode tip. In order to estimate the intensity distribution at a particular position around the electrode, we identified voxels that were located at a predetermined distance r from the axis. Let us define for $i = 1, \dots, 5$, a set of voxels \mathcal{X}_r^i such that

$$\mathcal{X}_r^i = \left\{ \mathbf{x} \in \mathcal{X}^i : r - \frac{\Delta_r}{2} \leq d(l(E_I^i, E_T^i), \mathbf{x}) \leq r + \frac{\Delta_r}{2}, \right. \\ \left. 0 \leq (\mathbf{x} - E_I^i) \cdot \mathbf{u}^i \leq \|E_I^i - E_T^i\| \right\}, \quad (7.21)$$

where $d(l(E_I^i, E_T^i), \mathbf{x})$ is the orthogonal distance of the voxel \mathbf{x} to a line given by the points E_I^i, E_T^i ; \mathbf{u} is the unit directional vector of the electrode axis. The set \mathcal{X}_r^i denotes a set of voxels such that: (i) they belong to the training image V^i , (ii) their distance from the electrode axis given by E_I^i, E_T^i is in the interval $\langle r - \frac{\Delta_r}{2}, r + \frac{\Delta_r}{2} \rangle$, (iii) their orthogonal projection on the axis lies between $\langle 0, \|E_I^i - E_T^i\| \rangle$; this ensures that no voxel in \mathcal{X}_r^i is located beyond E_I^i, E_T^i in the direction of \mathbf{u}^i . The parameter r was varied from 0 to R with a sampling step Δ_r . The upper limit was derived from the electrode diameter in the ultrasound image. Assuming an electrode with a diameter comparable to the wavelength, its diameter in the image is given by the size of ultrasound system PSF, which in our case was 1 mm. To estimate the intensity distribution of voxels located further from the axis the upper limit R was set to 2 mm. The sampling step Δ_r was selected as a half of the ultrasound system axial resolution (0.2 mm). We subsequently determined a union of intensities corresponding to voxels in \mathcal{X}_r^i over all training images,

$$\mathcal{I}_r = \bigcup_{i=1}^5 V^i(\mathcal{X}_r^i); \quad r = 0, \Delta_r, 2\Delta_r, \dots, 2R. \quad (7.22)$$

For given r , the set \mathcal{I}_r is composed of intensities of the voxels that are located at the distance r from the electrode axis. These values can be interpreted as a sample of a random variable that is drawn from an unknown probability density function $P(I|r)$. $P(I|r)$ can be used to model the intensity distribution of voxels at distance r . We decided to use a non-parametric density estimation to construct the probability distribution $P(I|r)$. Unlike the parametric estimators that requires a fixed distribution model to be set, non-parametric estimators provides distribution estimates solely on the given dataset [100]. Among the non-parametric estimators, we selected the kernel density estimator [101] which compared to other non-parametric methods such as histograms provides smooth estimates and there is no need to fix the centers of bin that can have a significant influence on the

resultant distribution. The Gaussian function with the zero mean and the unit variance was selected as the estimator kernel. For fixed r , the intensity distribution $P(I|r)$ was calculated as a weighted sum of Gaussian functions centered at each observation,

$$P(I|r) = \frac{1}{|\mathcal{I}_r|q_r} \sum_{i=1}^{|\mathcal{I}_r|} K\left(\frac{I - I_{r,i}}{q_r}\right), \quad (7.23)$$

where

$$K(x) = \frac{1}{\sqrt{2\pi}} e^{-\frac{x^2}{2}} \quad (7.24)$$

and q_r is the estimator bandwidth (smoothing parameter). The optimal bandwidth for a kernel density estimate can be calculated on the basis of an MISE criterion that is equal to the integral of the squared mean of difference between the ground-truth and the estimated distribution [102], see Equation (7.2). Silverman [103] demonstrated that for the estimator with a Gaussian kernel, the optimal bandwidth can be approximated by

$$q_r = 0.9 \cdot \min \left\{ \sigma_{\mathcal{I}_r}, \frac{1}{1.34} \text{IRQ}(\mathcal{I}_r) \right\} \cdot |\mathcal{I}_r|^{-\frac{1}{5}}, \quad (7.25)$$

where $\sigma_{\mathcal{I}_r}$ is the standard deviation of intensities in \mathcal{I}_r and $\text{IRQ}(\mathcal{I}_r)$ is their interquartile range. Estimated intensity distribution $P(I|r)$ is shown in Figure 7.6. By comparing the intensity priors for $r = 0$ mm and $r = 2$ mm (Figure 7.7), we can notice that the intensity of voxels on the axis are higher than the intensity of more distant voxels. It is also interesting to note the similarity between the intensity distribution $P(I|2)$ and the Gamma distribution estimated in Section 7.1.

Cost function Given a matrix of curve coefficients \mathbf{H} and the intensity priors $P(I|r)$, our task is to determine how well the curve $c(t; \mathbf{H})$ approximates the electrode axis in a segmented image $V: \mathcal{X}_e \rightarrow \mathcal{I}$. The measure $C(\mathbf{H})$ to assess the goodness-of-fit of Model II is based on the probability that the intensity of voxels around the curve follow the estimated distribution $P(I|r)$. Assuming that the voxel intensity are statistically independent, the probability is equal to

$$\prod_{i=1}^{|\mathcal{X}_e|} P(V(\mathbf{x}_i) | d(c(t; \mathbf{H}), \mathbf{x}_i)), \quad (7.26)$$

where $d(c(t; \mathbf{H}), \mathbf{x}_i)$ is the distance of the voxel \mathbf{x}_i from the axis defined by \mathbf{H} , which is approximated by Equation (7.20). We define the cost function $C(\mathbf{H})$ as

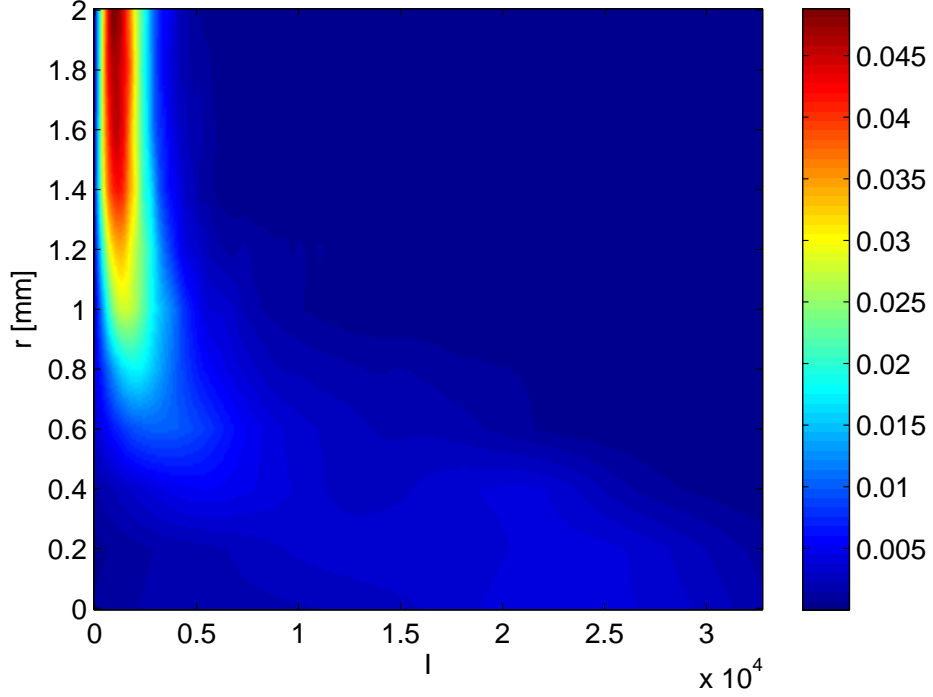


Figure 7.6: *Intensity priors $P(I|r)$ estimated from a training set of images. For fixed r , the function $P(I|r)$ describes the intensity distribution of voxels located at distance r from the electrode axis.*

the negative of the logarithm,

$$C(\mathbf{H}) = - \sum_{i=1}^{|\mathcal{X}_e|} \log P(V(\mathbf{x}_i) | d(c(t; \mathbf{H}), \mathbf{x}_i)). \quad (7.27)$$

The curve corresponding to matrix \mathbf{H}^* that minimizes $C(\mathbf{H})$ is considered to be the best estimate of the electrode axis,

$$\mathbf{H}^* = \underset{\mathbf{H} \in \mathbb{R}^{12}}{\operatorname{argmin}} C(\mathbf{H}). \quad (7.28)$$

7.2.3 Model III – Axis shape and intensity profile

Model II describes intensity priors by means of an estimated distribution $P(I|r)$ that is graphically represented in Figure 7.6. We can observe changes in the intensity distribution with respect to the distance of voxels from the electrode. Note that the intensity mean is low for distant voxels and it increases as the

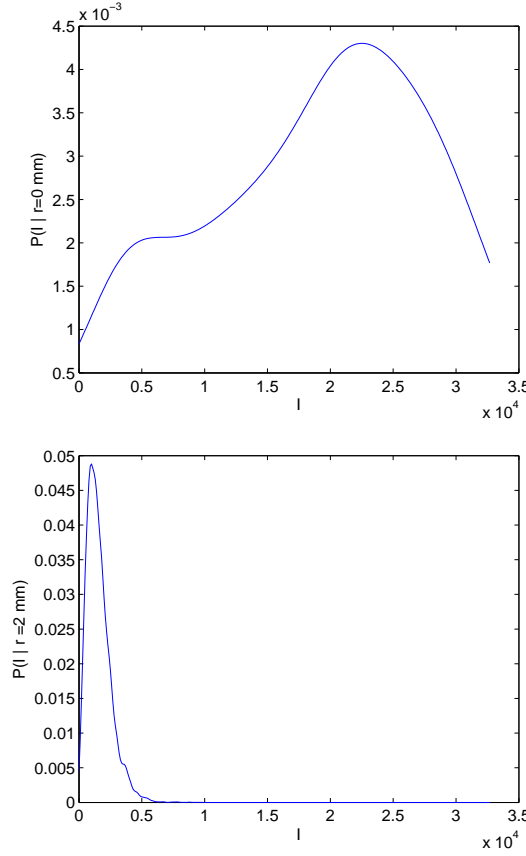


Figure 7.7: Examples of intensity distribution $P(I | r)$ for $r = 0 \text{ mm}$ and $r = 2 \text{ mm}$.

distance diminishes (Figure 7.7). This suggests that there is a relation between the voxel intensity and the voxel location with respect to the electrode. To exploit this information, we propose to construct an a priori function (referred to as the intensity profile) that provides typical voxel intensity as a function of the voxel distance from the electrode. This function together with the axis shape model introduced in Section 7.2.1 constitutes the basis of Model III. A cost of the model reflects the difference between true voxel intensities and the intensities provided by the intensity profile. The model-fitting-axis-localization algorithm that makes use of this model will be referred to by MF3.

The intensity profile models the dependence between the voxel-to-axis distance r and the voxel intensity I by a function $I_{\text{prf}}(r)$. It was constructed using a training set of five images $V^i: \mathcal{X}^i \rightarrow \mathcal{I}^i; i = 1, \dots, 5$. As in Section 7.2.2 describing Model II, sets of voxels \mathcal{X}_r^i (Equation (7.21)) at the distance r from the axis were found and corresponding intensities \mathcal{I}_r (Equation (7.22)) were identified. Contrary to

intensity priors found by means of a non-parametric kernel estimator that requires no a priori hypothesis about the underlying class of distribution, a parametric model fitting was employed to describe the probability distribution of intensities \mathcal{I}_r . Based on the observation that the intensity distribution of all voxels can be modeled by Gamma distribution (Section 7.1), we represent the distribution of intensities \mathcal{I}_r , for a fixed r , also by Gamma distribution,

$$P(I_r; \psi_r, \xi_r) = I_r^{\psi_r-1} \frac{e^{-\frac{I_r}{\xi_r}}}{\xi_r^{\psi_r} \Gamma(\psi_r)}; \quad \forall I_r \in \mathcal{I}_r, \quad (7.29)$$

with shape and scale parameters ψ_r, ξ_r . These parameters were for $r = 0, \dots, R$, determined as the maximum likelihood estimates to fit the Gamma distribution to the sample \mathcal{I}_r [99],

$$\tau_r = \ln \left(\frac{1}{|\mathcal{I}_r|} \sum_{I_r \in \mathcal{I}_r} I_r \right) - \frac{1}{|\mathcal{I}_r|} \sum_{I_r \in \mathcal{I}_r} \ln(I_r), \quad (7.30)$$

$$\psi_r = \frac{3 - \tau_r + \sqrt{(\tau_r - 3)^2 + 24\tau_r}}{12\tau_r}, \quad (7.31)$$

$$\xi_r = \frac{1}{\psi_r |\mathcal{I}_r|} \sum_{I_r \in \mathcal{I}_r} I_r. \quad (7.32)$$

We define the intensity profile $I_{\text{prf}}(r)$ at r as the mean of fitted Gamma distribution $P(I_r; \psi_r, \xi_r)$, that is equal to $\psi_r \xi_r$ [99],

$$I_{\text{prf}}(r) = \mathbb{E}[\mathcal{I}_r] = \psi_r \xi_r. \quad (7.33)$$

Figure 7.8 depicts an intensity profile computed from the training set of images $V^i: \mathcal{X}^i \rightarrow \mathcal{I}^i; i = 1, \dots, 5$. Note that the mean intensity declines from 19000 on the axis to 1800 further from the electrode, which confirms our observation about the dependence of the mean intensity of voxels on their distance from the axis.

Cost function Let $I_{\text{prf}}(r)$ be the intensity profile that we have determined a priori from the set of training images (Equation (7.33)). To quantify the quality of the goodness-of-fit of the curve described by \mathbf{H} , we define a cost function $C(\mathbf{H})$. It is calculated as the difference between the true intensity of voxels \mathcal{X}_e around the curve $c(t; \mathbf{H})$ and the estimated intensity profile $I_{\text{prf}}(r)$,

$$C(\mathbf{H}) = \sum_{\mathbf{x} \in \mathcal{X}_e} \left[V(\mathbf{x}) - I_{\text{prf}}\left(d(c(t; \mathbf{H}), \mathbf{x})\right) \right]^2, \quad (7.34)$$

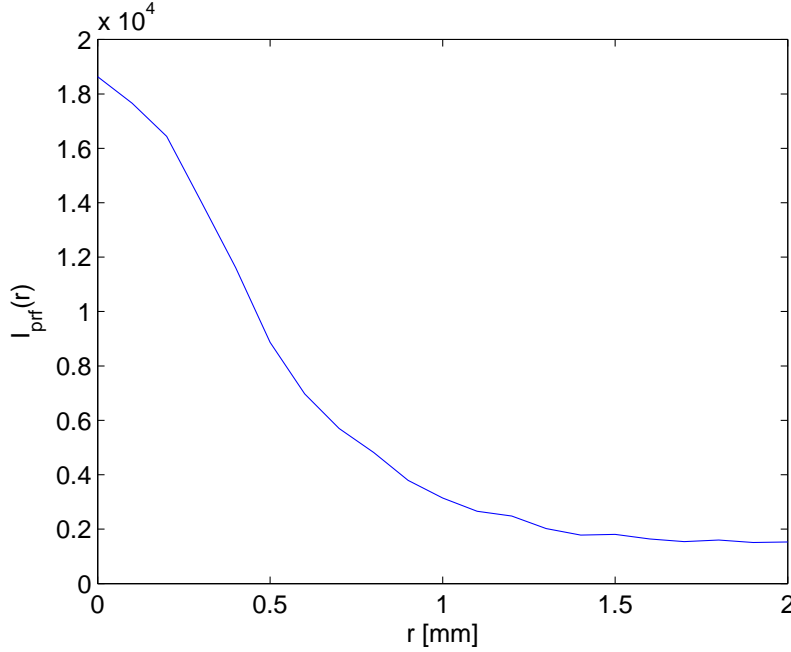


Figure 7.8: *Estimated intensity profile. Using training set of images, we establish a function $I_{\text{prf}}(r)$ that models voxel intensity at distance r from the electrode axis. The graph indicates that the voxel intensity decreases as the distance increases.*

where $d(c(t; \mathbf{H}), \mathbf{x})$ is the approximation (Equation (7.20)) of the distance between the curve $c(t; \mathbf{H})$ and the voxel \mathbf{x} . This criterion penalizes curves that do not approximate the axis well, since the intensity profile of neighbouring voxels does not correspond to the model intensity profile, whereas it is low if the intensity of voxels around $c(t; \mathbf{H})$ agrees with $I_{\text{prf}}(r)$. Therefore, a curve $c(t; \mathbf{H}^*)$ that minimizes $C(\mathbf{H})$ is selected as the best axis approximation,

$$\mathbf{H}^* = \underset{H \in \mathbb{R}^{12}}{\operatorname{argmin}} C(\mathbf{H}). \quad (7.35)$$

7.3 Estimating model with R-RANSAC

In Section 7.2, three distinct models were proposed to characterize the electrode features in an ultrasound image by describing the shape of axis and the statistical properties of voxel intensities. We detailed the process of extracting a priori information such as the intensity priors $P(I | r)$ and intensity profile $I_{\text{prf}}(r)$ from a training set of images. Further, a cost function was defined for each model as a function of the coefficient matrix \mathbf{H} that specifies the cubic curve approximating

the electrode axis. The purpose of this criterion is to quantify how well the model fits the true electrode position in a segmented image $V: \mathcal{X}_e \rightarrow \mathcal{I}$. The problem of localizing the electrode axis can be consequently solved by minimizing the cost function with respect to \mathbf{H} . However, this minimization task has no closed form solution and therefore a numerical method must be implemented. We propose to use a randomized version of the RANSAC estimator [104, 38], which is an iterative, stochastic algorithm permitting to determine the parameters of a model given a set of observed data. The principal advantage is the ability to provide robust estimates of model parameters even when the underlying dataset contains a significant portion of outliers. The principle of the RANSAC estimator [35] and its randomized modification [104, 38] is summarized in Section 3.3. In following paragraphs, we describe in details the implementation of R-RANSAC applied to the problem of estimating electrode model parameters given a segmented ultrasound image.

The algorithm (Table 7.2) takes as the input a segmented ultrasound image $V: \mathcal{X}_e \rightarrow \mathcal{I}$ and one of the Models I,II,III. It returns the coefficients matrix $\hat{\mathbf{H}}_{\text{RNS}}$ and an ordered quadruple of control points $\hat{\mathcal{D}}_{\text{RNS}}$ representing the best model parameters found. Three parameters η , κ_{\max} , ρ are used to control the flow of the algorithm. Their meaning is explained in detail below. At the beginning, C_{RNS} that stores the cost of the best-so-far model is set to infinity or to some large value. The total number of iterations J is calculated adaptively, see step 6(b) of the algorithm. Its initial value is determined from the probability P_{intl} that four randomly selected points from \mathcal{X}_e are all electrode voxels (inliers),

$$P_{\text{intl}} = \frac{\binom{|\mathcal{X}_{\text{intl}}|}{4}}{\binom{|\mathcal{X}_e|}{4}} \approx \zeta^4, \quad (7.36)$$

where $\zeta = \frac{|\mathcal{X}_{\text{intl}}|}{|\mathcal{X}_e|}$ is the fraction of electrode voxels $\mathcal{X}_{\text{intl}}$ in \mathcal{X}_e . By making a non-restrictive assumption that \mathcal{X}_e is composed of 50% of inliers and 50% of outliers, we let $\zeta = 0.5$. Using the probability P_{intl} , the initial number of iterations J (Equation 3.28) is given by

$$J = \frac{\ln \eta}{\ln(1 - P_{\text{intl}})}, \quad (7.37)$$

where η is a control parameter that defines the probability that the best model parameters will not be found.

Each j -th iteration of the R-RANSAC algorithm is composed of several operations:

INPUT

$V: \mathcal{X}_e \rightarrow \mathcal{I}$ – segmented image.

Either of Model I,II,III.

η, κ_{max}, ρ – control parameters.

OUTPUT

$\hat{\mathbf{H}}_{\text{RNS}}$ – coefficients of the curve approximating the electrode axis.

$\hat{\mathcal{D}}_{\text{RNS}}$ – control points on the curve.

INITIALIZATION

$C_{\text{RNS}} := +\infty$.

Compute the initial number of iterations J and set counter j to 1.

ITERATIONS While $j \leq J$ repeat:

1. Select randomly a subset $\mathcal{S}_j \subset \mathcal{X}_e$, $|\mathcal{S}_j| = 4$ and compute $\kappa(\mathcal{S}_j)$. If $\kappa(\mathcal{S}_j) \leq \kappa_{max}$, then continue; otherwise repeat step 1.
 2. Find \mathcal{D}_j by ordering points in \mathcal{S}_j .
 3. Compute coefficient matrix \mathbf{H}_j from the quadruple \mathcal{D}_j .
 4. Check consistency of a randomly selected point \mathbf{x} from \mathcal{X}_e with the model $c(t; \mathbf{H}_j)$. If \mathbf{x} passes, then continue; otherwise increment j and go to step 1.
 5. Determine the model cost $C(\mathbf{H}_j)$.
 6. Compare the cost of current and the best-so-far model. If $C(\mathbf{H}_j) < C_{\text{RNS}}$, then:
 - (a) $\hat{\mathbf{H}}_{\text{RNS}} := \mathbf{H}_j$, $\hat{\mathcal{D}}_{\text{RNS}} := \mathcal{D}_j$ and $C_{\text{RNS}} := C(\mathbf{H}_j)$.
 - (b) Update number of iterations J and reset counter j to 1.
- Otherwise: Increment j and go to step 1.

Table 7.2: *Implementation of the R-RANSAC algorithm that is used to compute the parameters of a model approximating the electrode axis.*

1. A set \mathcal{S}_j of four distinct points $\mathcal{S}_j = \{\mathbf{x}_{1,j}, \mathbf{x}_{2,j}, \mathbf{x}_{3,j}, \mathbf{x}_{4,j}\}$ is selected from \mathcal{X}_e with the uniform distribution. Four is the minimal number of points necessary to determine the coefficients matrix \mathbf{H}_j . Since the computation of the model cost generated by the points in \mathcal{S}_j is time-consuming, we want to select only such subsets \mathcal{S}_j that will likely lead to a good model parameters. First, we require that the selected points generate a curve with a limited curvature. However, the curvature can not be expressed analytically from the control points. We introduce an alternative curvature-like measure $\kappa(\mathcal{S}_j)$. Let $l(s; L_j, \mathbf{u}_j)$ be a parametric equation in a parameter s of a line passing through a point L_j with a unit directional vector \mathbf{u}_j . We choose L_j to be the coordinate mean of points \mathcal{S}_j and let \mathbf{u}_j to be the maximum eigenvector (in the sense of eigenvalues) of the point coordinate covariance matrix. We define $\kappa(\mathcal{S}_j)$ as the maximum orthogonal distance $d(\cdot)$ between the control points \mathcal{S}_j and the line $l(s; L_j, \mathbf{u}_j)$,

$$\kappa(\mathcal{S}_j) = \max_{i=1,\dots,4} d(l(s; L_j, \mathbf{u}_j), \mathbf{x}_{i,j}). \quad (7.38)$$

$\kappa(\mathcal{S}_j)$ is compared to κ_{max} , which is a control parameter used to limit the curvature of generated models. If $\kappa(\mathcal{S}_j) \leq \kappa_{max}$ then the selected points \mathcal{S}_j are accepted; otherwise, a new selection of four points is carried out.

2. The shape of a parametric curve $c(t; \mathbf{H}_j)$ is determined by the order of control points $\mathcal{S}_j = \{\mathbf{x}_{1,j}, \mathbf{x}_{2,j}, \mathbf{x}_{3,j}, \mathbf{x}_{4,j}\}$ with respect to the curve parameter t . Choosing an order of points \mathcal{S}_j arbitrarily would presumably produce a multiple point curve or a curve with an excessive curvature. To avoid this problem, \mathcal{S}_j is ordered to obtain a quadruple of control points $\mathcal{D}_j = (D_{1,j}, D_{2,j}, D_{3,j}, D_{4,j})$ by projecting \mathcal{S}_j on the line $l(s; L_j, \mathbf{u}_j)$ found in the previous step, see Figure 7.9. We compute parameters $s_{i,j}; i = 1, \dots, 4$; that correspond to the projections of points \mathcal{S}_j on $l(s; L_j, \mathbf{u}_j)$,

$$s_{i,j} = (\mathbf{x}_{i,j} - L_j) \cdot \mathbf{u}_j; \quad i = 1, \dots, 4. \quad (7.39)$$

The ordering of \mathcal{S}_j is then defined by the order of \mathcal{S}_j with respect to the parameters $s_{i,j}; i = 1, \dots, 4$. Accordingly \mathcal{D}_j is given by

$$\mathcal{D}_j = (\mathbf{x}_{i_1,j}, \mathbf{x}_{i_2,j}, \mathbf{x}_{i_3,j}, \mathbf{x}_{i_4,j}), \quad (7.40)$$

where (i_1, i_2, i_3, i_4) is a permutation of “1,2,3,4” such that $s_{i_1,j} < s_{i_2,j} < s_{i_3,j} < s_{i_4,j}$.

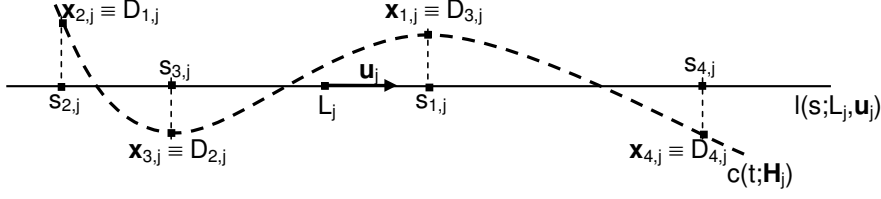


Figure 7.9: Ordering of the set \mathcal{S}_j . Quadruple of curve control points \mathcal{D}_j is obtained by ordering voxels $\mathcal{S}_j = \{\mathbf{x}_{1,j}, \mathbf{x}_{2,j}, \mathbf{x}_{3,j}, \mathbf{x}_{4,j}\}$ according to their projections on the least mean square line $l(s; L_j, \mathbf{u}_j)$.

3. For given quadruple \mathcal{D}_j , the coefficient matrix \mathbf{H}_j is found using the mapping $\Omega: \mathcal{D} \rightarrow \mathbf{H}$, see Equation (7.13) in Section 7.2.1 .
4. As proposed by Chum [104, 38], we determine the consistency of a randomly selected point \mathbf{x} from \mathcal{X}_e with $c(t; \mathbf{H}_j)$ before the model evaluation on the whole data set. If the point is consistent with the model, that is if

$$d(c(t; \mathbf{H}_j), \mathbf{x}) \leq \rho, \quad (7.41)$$

where $d(\cdot)$ is the approximate distance (Equation (7.20)) and ρ is a control parameter, then we continue the verification process. Otherwise, the model is rejected and we proceed to step 1 after incrementing the iteration counter j .

5. To measure how well the model $c(t; \mathbf{H}_j)$ approximates the true electrode axis in the segmented image $V: \mathcal{X}_e \rightarrow \mathcal{I}$, we evaluate the cost function $C(\mathbf{H}_j)$ that corresponds to the selected model (Equations (7.15), (7.28), (7.35)).
6. The cost $C(\mathbf{H}_j)$ is compared to the cost of the best-so-far model C_{RNS} . If a better model has been found, $C(\mathbf{H}_j) < C_{\text{RNS}}$, then the model parameters and the number of iterations are updated:

- (a) The coefficient matrix $\hat{\mathbf{H}}_{\text{RNS}}$, control points $\hat{\mathcal{D}}_{\text{RNS}}$ and the cost C_{RNS} of the best-so-far model are replaced by respective values computed in j -th iteration,

$$\hat{\mathbf{H}}_{\text{RNS}} := \mathbf{H}_j; \quad \hat{\mathcal{D}}_{\text{RNS}} := \mathcal{D}_j; \quad C_{\text{RNS}} := C(\mathbf{H}_j), \quad (7.42)$$

- (b) A better fit model allows us to determine more accurately the number of inliers in \mathcal{X}_e and consequently to update J , which approaches the optimal number of iterations necessary to find the best model parameters

with the probability $1 - \eta$. We define a set of inliers \mathcal{X}_{inl} as voxels \mathcal{X}_e that are consistent with the curve $c(t; \mathbf{H}_j)$,

$$\mathcal{X}_{inl} = \left\{ \mathbf{x} \in \mathcal{X}_e : d(c(t; \mathbf{H}_j), \mathbf{x}) \leq \rho \right\}, \quad (7.43)$$

where $d(\cdot)$ is the approximated curve-to-point distance (Equation (7.20)) and ρ is a control parameter. The control parameter ρ is deduced from the electrode diameter in an ultrasound image. The probability P_{inl} is computed using the ratio ζ of the number of inliers to all voxels, see Equation (7.36) and the total number of iterations J is updated using Equation (7.37). Finally, the iteration counter j is reset to 1.

Values stored in $\hat{\mathbf{H}}_{\text{RNS}}$, $\hat{\mathcal{D}}_{\text{RNS}}$ and C_{RNS} characterize the best model found by the R-RANSAC estimator within j iterations.

Figure 7.10 shows the true electrode axis and the axis found by R-RANSAC procedure for an increasing number of iterations. By a probabilistic minimization of the model cost function, the localization accuracy is improved as the model approaches the true electrode position. Although the initial solution is far from the optimal one, the algorithm progressively makes the estimate more precise until a model that approximates the electrode well is found.

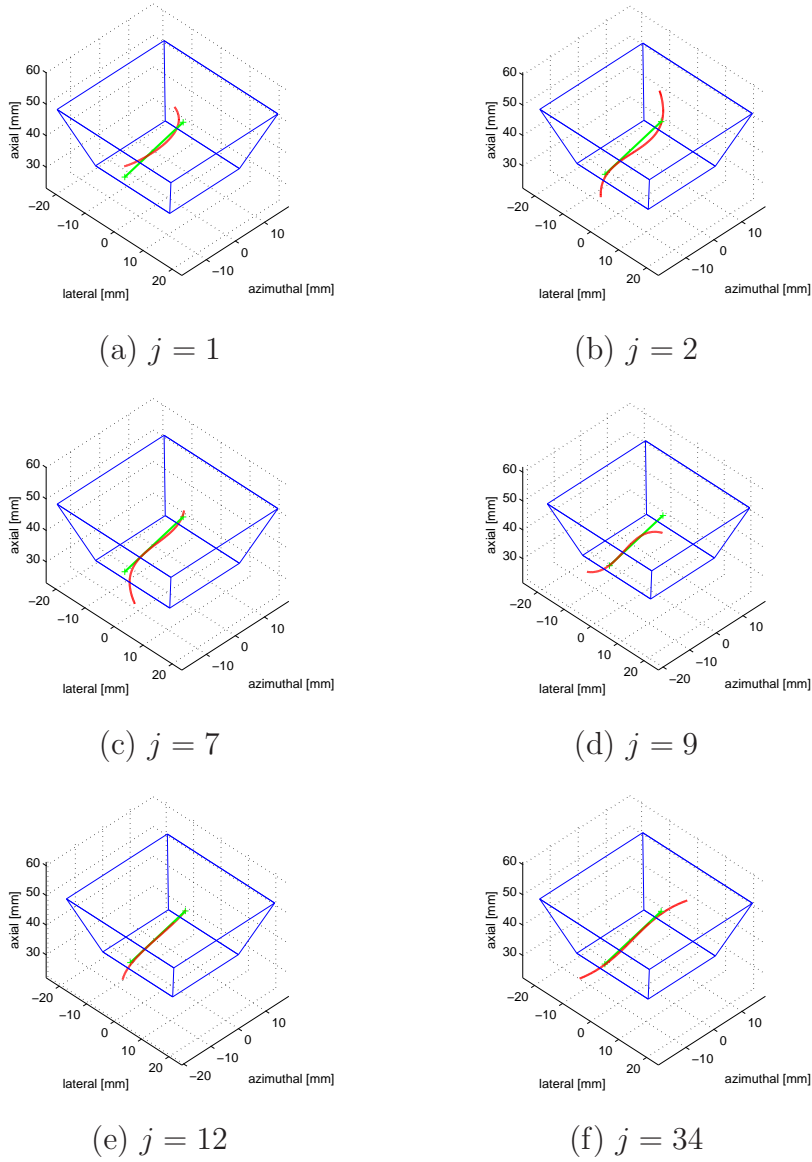


Figure 7.10: *Electrode models found by R-RANSAC for increasing number of iterations j . Selected ROI is delineated by blue lines; true electrode axis is marked by a green line segments; and red curve represents the estimated electrode axis.*

7.4 Improving axis position estimate

In Section 7.3, we describe in detail an implementation of the R-RANSAC estimator that permits to find the parameters of a model that characterizes the electrode position. Here we explain an implemented optimization procedure that further improves the axis estimate. The convergence of the algorithm is enforced by ini-

tiating the algorithm with the solution provided by R-RANSAC, which is already close to the global optimum.

Instead of optimizing the coefficient matrix $\hat{\mathbf{H}}_{\text{RNS}}$, we shall optimize the control points $\hat{\mathcal{D}}_{\text{RNS}}$. This has the advantage in the sense of sensitivity. The matrix \mathbf{H} which is composed of curve coefficients introduces a non-uniform sensitivity of resulting curve to the coefficient variations. For instance, the same change applied to coefficients h_{14}, h_{24}, h_{34} will have greater effect on the electrode shape compared to the change in coefficients h_{11}, h_{21}, h_{31} , since the former are multiplied by the cube of curve parameter t , whereas the latter stand out in $c(t; \mathbf{H})$ as constants, see Equation (7.8). In case of \mathcal{D} , the sensitivity problem is limited, because all elements express the coordinates of control points. This in consequence improves the numerical stability of the optimization algorithm.

The optimization task can be stated in a similar manner as the minimization problem described in the preamble of Section 7.3. Given a segmented image $V: \mathcal{X}_e \rightarrow \mathcal{I}$, an electrode model with respective priors and an initial solution $\hat{\mathcal{D}}_{\text{RNS}}$, we want to determine a quadruple $\hat{\mathcal{D}}_{\text{SMP}}$ that minimizes the model cost function $C(\Omega(\hat{\mathcal{D}}_{\text{SMP}}))$, where $\Omega: \mathcal{D} \rightarrow \mathbf{H}$ is a mapping of control points \mathcal{D} to a coefficient matrix \mathbf{H} , see Equation (7.13). To solve this optimization problem, we selected the downhill simplex method introduced by Nelder and Mead [105]. It is a direct-search, unconstrained optimization method that minimizes a scalar valued function of N variables using only the objective function values, without any derivative information (analytical or numerical).

The optimization is summarized in Table 7.3 and the improvement in the estimate of the electrode axis is shown in Figure 7.11.

INPUT

$V: \mathcal{X}_e \rightarrow \mathcal{I}$ – segmented image.

Either of Model I,II,III.

$\hat{\mathcal{D}}_{\text{RNS}}$ – control points estimated by R-RANSAC.

N_{iter} – number of iterations.

OUTPUT

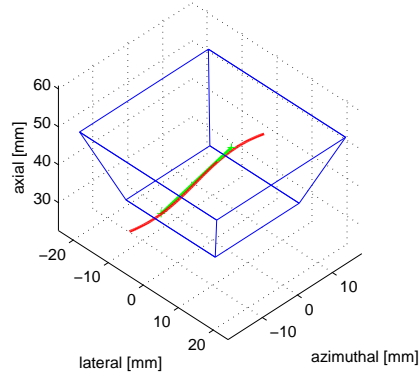
$\hat{\mathcal{D}}_{\text{SMP}}$ – optimized control points of a curve approximating the axis.

$\hat{\mathbf{H}}_{\text{SMP}}$ – optimized curve coefficients.

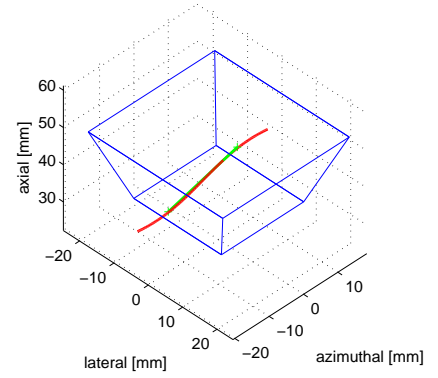
ALGORITHM .

1. Use downhill simplex search to minimize function $C(\Omega(\mathcal{D}))$ for \mathcal{D} in N_{iter} iterations , with initial solution $\hat{\mathcal{D}}_{\text{RNS}}$. Return $\hat{\mathcal{D}}_{\text{SMP}}$.
2. Compute $\hat{\mathbf{H}}_{\text{SMP}}$ given $\hat{\mathcal{D}}_{\text{SMP}}$.

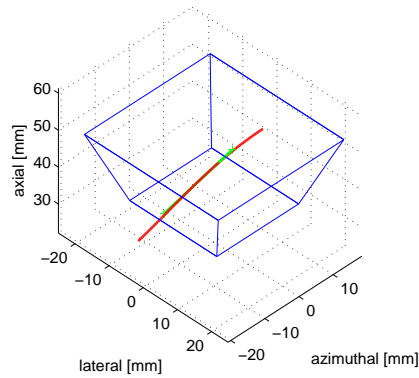
Table 7.3: *Optimization of the electrode axis estimate using the downhill simplex method.*



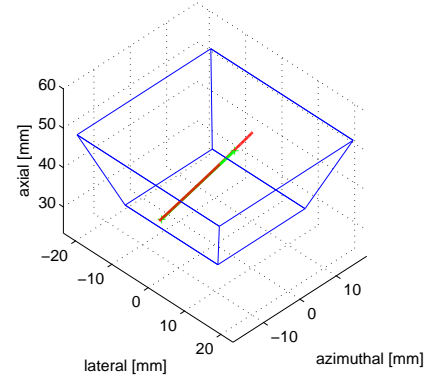
(a) #iterations 0



(b) #iterations 25



(c) #iterations 75



(d) #iterations 150

Figure 7.11: *Improvement of the axis estimates using the downhill simplex optimization. Blue lines delineate selected ROI; green line segment represents true electrode position; and red curve represents estimated electrode axis.*

Chapter 8

Tip localization

In Chapters 6, 7, we proposed two algorithms that estimate the electrode axis. This information does not, however, completely describe the electrode position. We also need to identify the electrode endpoints.

The electrode is not entirely present in the field of view and only two distinct points on the axis are visible: (i) electrode endpoint that penetrates the tissue (electrode tip), (ii) the intersection of the electrode with the FOV (intercept point). Provided that a curve approximating the electrode axis is known, the task of an identification of the intercept point can be trivially solved by finding the intersection of the curve with an image boundary. The localization of the electrode tip is more challenging. Speckle noise and possible signal drop-outs, which result in apparent electrode breaks, make the electrode tip localization difficult.

We propose to estimate the electrode tip by analyzing the intensity along the electrode axis [89, 90, 97, 98, 91]. The voxel intensity along the estimated axis is traced starting from the intercept point (image boundary). Figure 8.1 shows an example of the intensity along the estimated axis as a function of the curve parameter.

Note that in the area of electrode, the intensity is much higher than in the area of background, which is a consequence of a higher echogenicity of the electrode compared to the tissue. We exploit this feature by thresholding the axis intensity with a threshold T_t . The point where the intensity decreases under T_t is marked as the electrode tip. The value of the threshold T_t is set using two a priori estimated distributions $P(bg|I)$, resp., $P(el|I)$ that describes the probability that a voxel belongs to the electrode, resp., the background given its intensity (Section 8.1). Small random scatterers present in tissue cause specular character of ultrasound

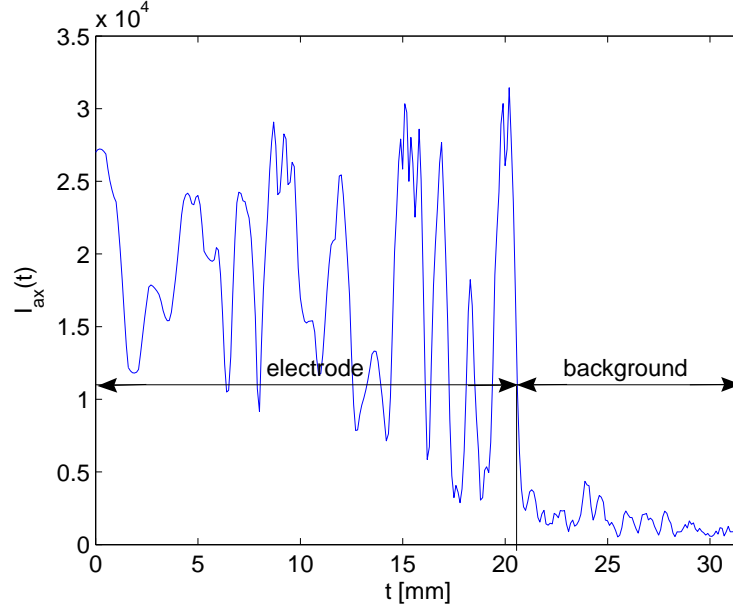


Figure 8.1: *Intensity of voxels located on the electrode axis. We observe large intensity variations in the area of electrode.*

data, which manifests itself as variations of the voxel intensity. The changes in voxel intensity can be observed in Figure 8.1. To avoid marking an electrode point where the intensity falls under T_t as the electrode tip (Figure 8.2), we define a maximum length of a break b_{max} and ignore any breaks shorter than b_{max} . We determine b_{max} using a histogram of break lengths, which is obtained by thresholding a realization of a random process that follows the electrode intensity distribution, see Section 8.2. The tip localization algorithm is summarized at the end of this chapter.

8.1 Estimating the threshold T_t

The detection of the electrode tip, which relies on comparing the axis intensity to a constant T_t can be formulated as an intensity based classification task of labeling a particular voxel as an electrode or background voxel. We determined an optimum value of T_t using prior distributions $P(\text{el} | I)$, $P(\text{bg} | I)$.

The priors $P(\text{el} | I)$, $P(\text{bg} | I)$ were estimated using a training set of N_0 ultrasound images $V^i: \mathcal{X}^i \rightarrow \mathcal{I}^i; i = 1, \dots, N_0$ of a portion of phantom containing a metallic electrode (in our case the number of training images N_0 was 5). The

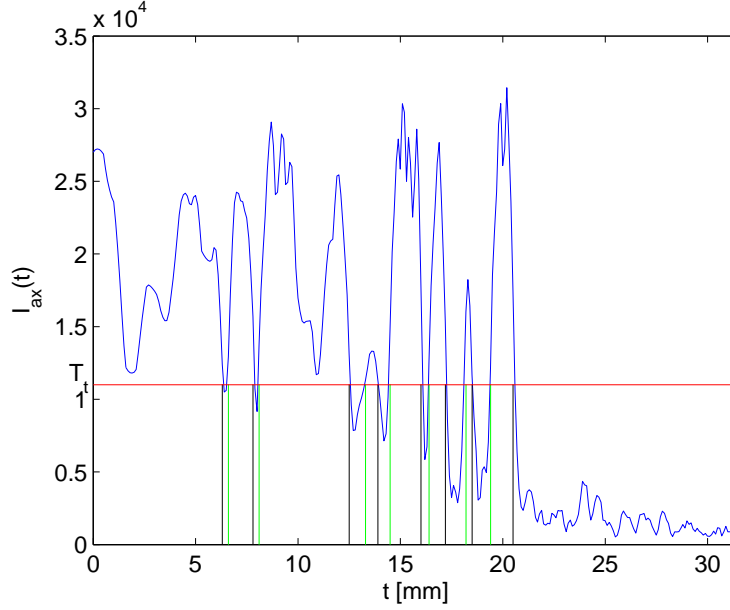


Figure 8.2: *Localization of electrode tip by thresholding the axis intensity. Due to the intensity variations, the intensity is in a number of electrode segments below threshold T_t producing short breaks.*

electrode axis was straight in all cases. We manually selected the coordinates of the intercept point E_I^i and the electrode tip E_T^i to define the true electrode position. In order to find the probability $P(\text{el} | I)$, resp., $P(\text{bg} | I)$ that a voxel with intensity I belongs to electrode, resp., background, we found a set of voxels $\mathcal{X}_{\text{bg}, I_j}^i$ that is given by

$$\begin{aligned} \mathcal{X}_{\text{bg}, I_j}^i = \left\{ \mathbf{x} \in \mathcal{X}^i : d(l(E_I^i, E_T^i), \mathbf{x}) > \rho, \right. \\ \left. 0 \leq (\mathbf{x} - E_I^i) \cdot \mathbf{u}^i \leq \|E_T^i - E_I^i\|, \right. \\ \left. V^i(\mathbf{x}) \in \left\langle I_j - \frac{\Delta_I}{2}, I_j + \frac{\Delta_I}{2} \right\rangle \right\}, \end{aligned} \quad (8.1)$$

where $d(\cdot)$ stands for an orthogonal distance of a voxel \mathbf{x} to a line passing through points E_I^i, E_T^i with the unit directional vector $\mathbf{u}^i = \frac{E_T^i - E_I^i}{\|E_T^i - E_I^i\|}$. $\mathcal{X}_{\text{bg}, I_j}^i$ contains voxels from \mathcal{X}^i such that: (i) their distance from the electrode axis is greater than ρ , (ii) they are located within E_I^i, E_T^i in the direction of \mathbf{u}^i , (iii) their intensities are in the interval $\left\langle I_j - \frac{\Delta_I}{2}, I_j + \frac{\Delta_I}{2} \right\rangle$. For a thin electrode that has a physical diameter of the order of ultrasound wavelength, parameter ρ is set according to the ultrasound PSF (in our case ρ was 1 mm). The range of intensities was discretized with Δ_I .

The sampling step Δ_I was set using the Freedman-Diaconis rule [106],

$$\Delta_I = 2 \cdot \text{IQR}(\mathcal{I}_{tr}) \cdot |\mathcal{I}_{tr}|^{-1/3}, \quad (8.2)$$

where $\mathcal{I}_{tr} = \bigcup_{i=1}^{N_0} \mathcal{I}^i$ is a set of voxel intensities over all training images and $\text{IQR}(\mathcal{I}_{tr})$ is the intensity interquartile range.

The number of background voxels close to the electrode axis is approximately the same as the number of electrode voxels. The probability $P(\text{bg} | I)$ was computed as

$$P(\text{bg} | I) = \frac{\sum_{i=1}^{N_0} |\mathcal{X}_{\text{bg}, I_j}^i|}{\sum_{i=1}^{N_0} |\mathcal{X}^i|}; \quad \forall I \in \left\langle I_j - \frac{\Delta_I}{2}, I_j + \frac{\Delta_I}{2} \right\rangle, \quad (8.3)$$

where the numerator, resp., the denominator is the number of background voxels with intensity I , resp., the number of voxels for all images in the training set (Figure 8.3). The probability $P(\text{el} | I)$ is complementary to $P(\text{bg} | I)$,

$$P(\text{el} | I) = 1 - P(\text{bg} | I). \quad (8.4)$$

The value of T_t was set to minimize the likelihood of an incorrect voxel classification. Its value was computed such that

$$P(\text{bg} | T_t) = P(\text{el} | T_t), \quad (8.5)$$

assuming that $P(\text{el} | I)$ is monotonic and hence there is only one such T_t . From Equation (8.4), we see that

$$P(\text{bg} | T_t) = \frac{1}{2}. \quad (8.6)$$

8.2 Estimating the maximum break length b_{max}

We define a break as a portion of the electrode axis, where the intensity is smaller than the estimated threshold T_t , see Figure 8.2. In order to keep the localization algorithm from marking a break as the electrode tip, we need to determine a maximum break length b_{max} that is still considered as a part of the electrode.

Let us denote by $P(I | \text{ax})$ the probability that a voxel on the axis has intensity I . It was estimated from a training set of the five images by means of the kernel density estimation. This procedure is detailed in Section 7.2.2 that deals with estimating the intensity priors (Equation (7.23)). Using the same notation, we can write that $P(I | \text{ax}) = P(I | r = 0)$, i.e., the probability of intensity on axis is equal to the intensity priors for $r = 0$.

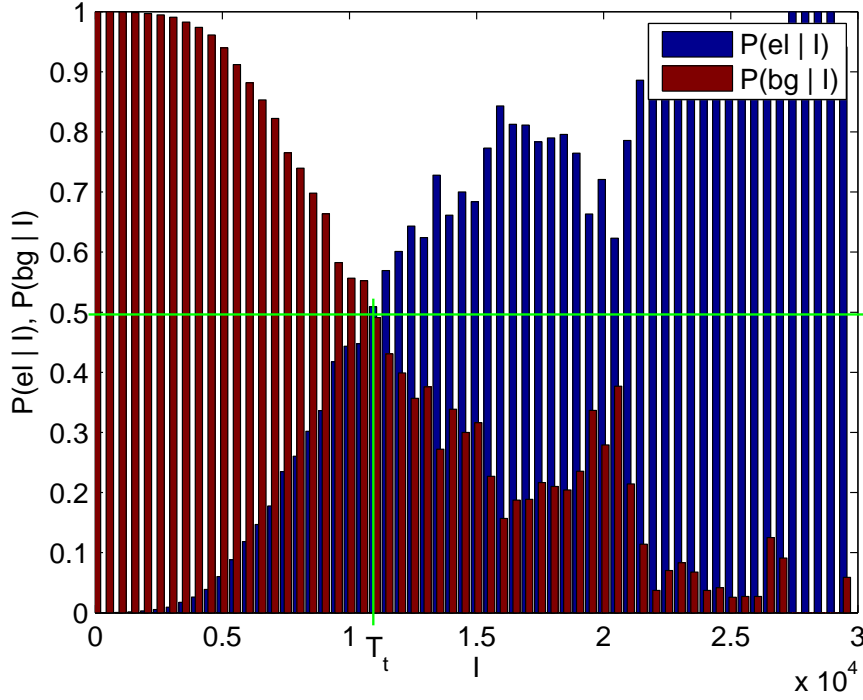


Figure 8.3: *Estimated distributions of electrode $P(\text{el} | I)$, resp., background $P(\text{bg} | I)$ voxels given their intensity I . To minimize the risk of a false voxel classification, threshold T_t is set such that $P(\text{el} | T_t) = P(\text{bg} | T_t)$.*

We made a simulation of the axis intensity. Let Ψ be a discrete function that maps a sequence of points $\mathcal{Z} = \{i\Delta_z\}_{i=1}^{N_\Psi}$ to $\tilde{\mathcal{I}}_{\text{ax}}$, which represents a realization of the random process $P(I | \text{ax})$,

$$\Psi: \mathcal{Z} \rightarrow \tilde{\mathcal{I}}_{\text{ax}}. \quad (8.7)$$

Δ_z was set equal to the distance between two adjacent voxels in the image and the number of realizations N_Ψ was 10^3 . To generate random samples from the distribution $P(I | \text{ax})$, we employed the inverse sampling transform, which transforms uniformly distributed samples using the inverse of the target cumulative distribution [107].

In order to obtain the information about the distribution of break lengths, the simulation of the axis intensity $\Psi(\mathcal{Z})$ was thresholded with T_t and the endpoints

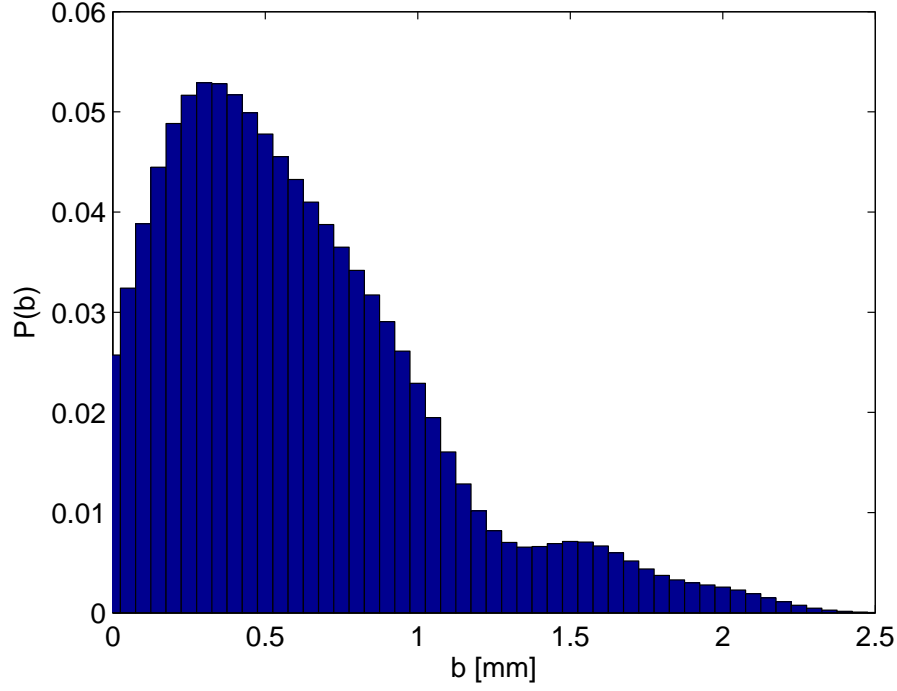


Figure 8.4: *Estimated distribution of break lengths $P(b)$ on electrode axis caused by thresholding the simulated axis intensity $\Psi(\mathcal{Z})$ with the threshold T_t .*

of each break were found. Let us define a set \mathcal{B} by,

$$\mathcal{B} = \left\{ b \in \mathbb{N} : \exists i \in \mathbb{N}, \forall j = i, i+1, \dots, i+b : \begin{aligned} &\Psi(z_{i-1}) \geq T_t, \\ &\Psi(z_{i+b+1}) \geq T_t, \\ &\Psi(z_j) < T_t \end{aligned} \right\}. \quad (8.8)$$

which contains the lengths of breaks. Their distribution $P(b)$ was approximated by a histogram (Figure 8.4) with a bin width Δ_B set using the Freedman-Diaconis rule, see Equation (8.2). From the histogram, the cumulative distribution $F(b)$ was found (Figure 8.5) and the maximum break length b_{max} was set as the 95% quantile of $F(b)$.

Table 8.1 summarizes the tip localization algorithm.

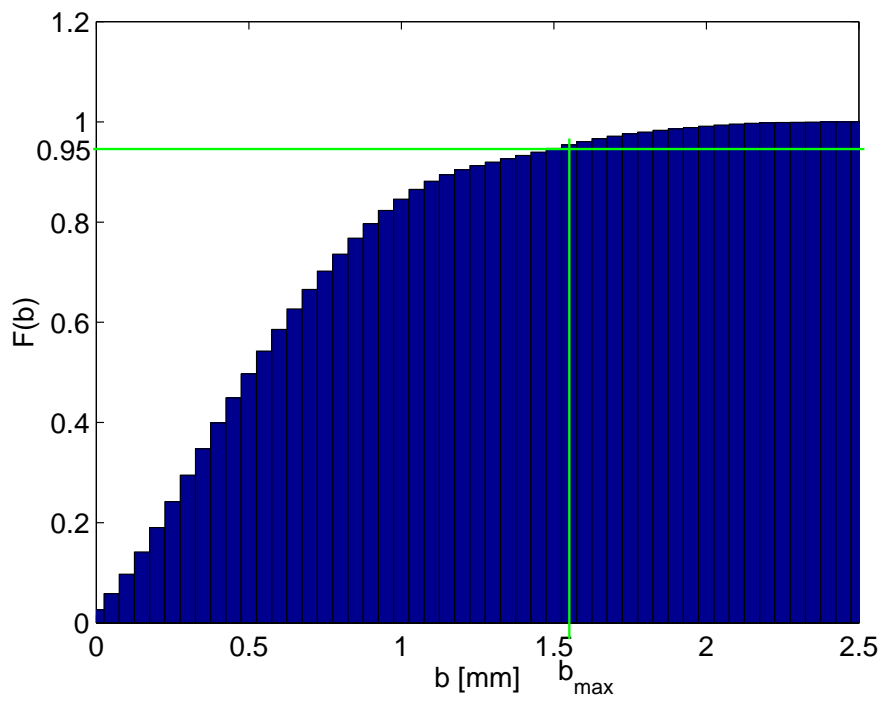


Figure 8.5: Cumulative distribution of break lengths $F(b)$. The maximum length of break b_{\max} that is considered as part of the electrode was set as the 95% quantile.

INPUT

$V: \mathcal{X} \rightarrow \mathcal{I}$ – image.

$c: \mathbb{R} \rightarrow \mathbb{R}^3$ – parametric description of the electrode axis.

E_I – intercept point.

T_t – threshold.

b_{max} – maximum break length.

OUTPUT

E_T – electrode tip.

ALGORITHM .

1. Trace the intensity $I_{ax}(t) = V(c(t))$ for increasing $t \in R, t \geq t_I$, where $c(t_I) = E_I$.
2. Find minimum t^* such that $\forall t \geq t^* : I_{ax}(t) < T_t$, while ignoring breaks shorter than b_{max} .
3. Compute the electrode tip coordinates, $E_T = c(t^*)$.

Table 8.1: *Main steps of the tip localization algorithm.*

Chapter 9

Experiments

In preceding chapters, novel algorithms that permit to determine the position of an electrode in a 3D ultrasound image were presented. We explained the general framework and underlying assumptions made about the input dataset. We also discussed the estimation of a priori information as well as the setting of parameters that control the algorithm behavior. In this chapter, the performance of the algorithms is assessed. A series of experiments on 3D images were carried out to determine the localization accuracy and the computational cost. Two distance measures were used to quantify the localization accuracy of the electrode axis and the tip, see Section 9.1. The proposed methods were initially tested on a number of simulated datasets that imitated a 3D ultrasound image of a portion of tissue with a highly scattering inclusion. The results are summarized in Section 9.2. The methods were subsequently evaluated on real 3D ultrasound images of a cryogel phantom containing a thin metallic electrode, see Section 9.3. The comparison of the proposed methods in term of processing time can be found in Section 9.4.

9.1 Localization accuracy measures

The problem of estimating the electrode position is composed of two subtasks. First, the electrode axis is found by the PIP transform method (Chapter 6) or using the model fitting (Chapter 7). Once the electrode axis is known, we proceed to the localization of the electrode tip (Chapter 8). Accordingly, we have to define two measures to assess the overall accuracy of the estimated electrode position: (i) axis localization accuracy ε_{axis} (Section 9.1.1), (ii) tip localization accuracy ε_{tip} (Section 9.1.2).

9.1.1 Axis accuracy

Let the true electrode position be given by the intercept point E_I , the tip point E_T and a cubic curve $c: \mathbb{R} \rightarrow \mathbb{R}^3$ with the curve parameter $t \in \mathbb{R}$ such that $c(0) = E_I$, $c(1) = E_T$. Let us further denote the estimated parametric curve that approximates the electrode axis by $\hat{c}: \mathbb{R} \rightarrow \mathbb{R}^3$ with the curve parameter $s \in \mathbb{R}$, see Figure 9.1.

We would like to express the axis accuracy as the maximum distance between the true and the estimated electrode axis, which is given by

$$\varepsilon_{axis}^{ideal} = \max_{t,s} \|\hat{c}(s) - c(t)\|. \quad (9.1)$$

Since this problem does not have analytical solution, we use an approximation of the curve-to-curve distance instead. On the curve $\hat{c}(s)$, point $\hat{c}(s_{E_I})$, resp., $\hat{c}(s_{E_T})$, which is closest to the point E_I , resp., E_T is identified with parameters

$$s_{E_I} = \min_{s \in \mathbb{R}} \|\hat{c}(s) - E_I\|, \quad (9.2)$$

$$s_{E_T} = \min_{s \in \mathbb{R}} \|\hat{c}(s) - E_T\|. \quad (9.3)$$

We assume that the mapping

$$s(t) = \operatorname{argmin}_{s \in \mathbb{R}} \|\hat{c}(s) - c(t)\| \quad (9.4)$$

is close to linear and we approximate it accordingly,

$$s(t) = (s_{E_T} - s_{E_I}) \cdot t + s_{E_I}; \quad t \in \langle 0, 1 \rangle. \quad (9.5)$$

The distance $\varepsilon_{axis}^{ideal}$ between curves $c(t)$, $\hat{c}(s)$ is then approximated by

$$\varepsilon_{axis} = \max_{t \in \langle 0, 1 \rangle} \|\hat{c}(s(t)) - c(t)\|. \quad (9.6)$$

9.1.2 Tip accuracy

The accuracy of the tip estimate \hat{E}_T is measured as the Euclidean distance between the true and estimated electrode tip position (Figure 9.1),

$$\varepsilon_{tip} = \|\hat{E}_T - E_T\|. \quad (9.7)$$

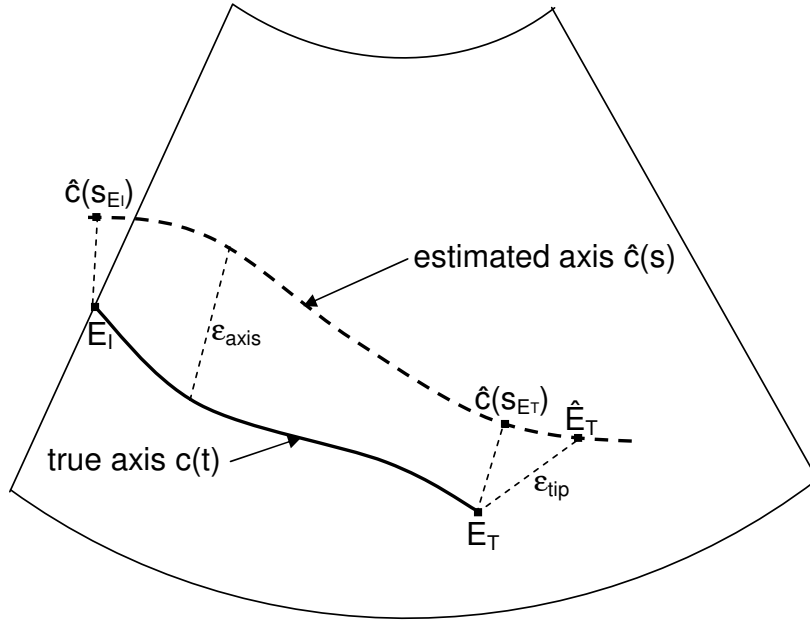


Figure 9.1: *Evaluation of the localization accuracy. The axis localization accuracy ϵ_{axis} is measured as the maximum distance between points with corresponding parameters on the true and estimated axis. Euclidean distance between the true and estimated tip is the tip accuracy ϵ_{tip} .*

9.2 Simulated 3D ultrasound images

In practice, the electrode configuration with respect to the field of view varies as well as the acoustic properties of surrounding tissue. We can observe different electrode positions, orientations, depths of insertion, etc. The characteristic of background such as the noise level is not constant either.

In order to evaluate the performance of the localization methods under various conditions, we decided to make a numerical simulation of ultrasound images and use them to test the algorithms. The significant advantage of simulated images over real data is that the ground truth, e.g., the electrode position, is known precisely and hence it can serve as a reference to compute the axis and the tip localization accuracy.

9.2.1 Numerical simulation of 3D ultrasound images

The images were simulated by means of the simulator FIELD II, which is a package of MATLAB functions developed by Jørgen Arendt Jensen at the Technical University of Denmark [31, 32, 33]. It permits to compute sampled RF signals coming out of a virtual probe that scans a medium represented by a cloud of spatially distributed diffusers. The mathematical background of the simulation is discussed in Section 3.2.1.

There are three main types of settings that must be set to obtain a realistic simulation of an ultrasound image: (i) transducer parameters, (ii) the dimension and the spatial sampling of the field of view, (iii) the parameters of simulated medium. In order to compare the outcome of experiments carried out on simulated images to the results on real ultrasound images, the simulation parameters were adjusted to simulate the ultrasound scanner KRETZ Voluson 530D, that we used to acquire real data.

Transducer settings

Among the parameters defining the transducer characteristics are the physical dimensions of a single piezoelectric crystal, the layout of crystals in the transducer, crystal resonance frequency and impulse response. These parameters have fundamental importance in determining the ultrasound system properties. They specify the shape of the field of view, number and position of focal points, the point spread function which in turns influences the system resolution, etc. We set the FIELD II parameters to simulate a mechanically tilted linear transducer with a sector field of view and electronic focalization with three transmit/receive focal points. Unfortunately, some transducer parameters were not known and had to be set experimentally. Mari [7] studied the distribution of pressure in the field of view of the KRETZ scanner. He used a hydrophone to measure the pressure at equidistant points in front of the ultrasound probe. We have set the unknown simulations parameters of the transducer so that the simulated ultrasound beam approximated the measured pressure field. The transducer parameters set in the FIELD II simulator are summarized in Table 9.1.

parameter	value
number of elements	128
element width [mm]	0.4
element height [mm]	5
element kerf [mm]	0.025
number of focal points (transmit/receive)	3
center focal point [mm]	[0 0 50]
resonance frequency [MHz]	7.5
transducer type	linear
field of view	3D, sector
scan plane deflection	tilted
scan plane angle φ	40°
number of beams N_b	71
title angle θ	40°
number of scan planes N_{sp}	53
depth of penetration [mm]	~ 70
RF signal sampling frequency [MHz]	27

Table 9.1: *Transducer and FOV parameters set in the FIELD II simulator to emulate the scanning characteristics of the KRETZ Voluson 530D scanner.*

Field of view

The simulated transducer sampled the medium with a sector scan plane of angle φ which was composed of N_b beams. The scan plane was in successive N_{sp} steps angularly tilted around the lateral axis with the total angle θ . The resulting 3D field of view of this transducer is depicted in Figure 9.2. To mimic the FOV and spatial sampling of the KRETZ scanner, the scan plane angle φ was set to 40° and the number of beams N_b to 71. The field of view was sampled with 53 planes and tilt angle $\theta = 40^\circ$. The depth of scanning of approximately 7 cm was selected to permit scanning the entire numerical phantom that is discussed in the following paragraph.

Numerical phantom

Under FIELD II, the ultrasound medium is represented by a set of diffusers whose acoustic properties are defined by their spatial arrangement and the coefficients of

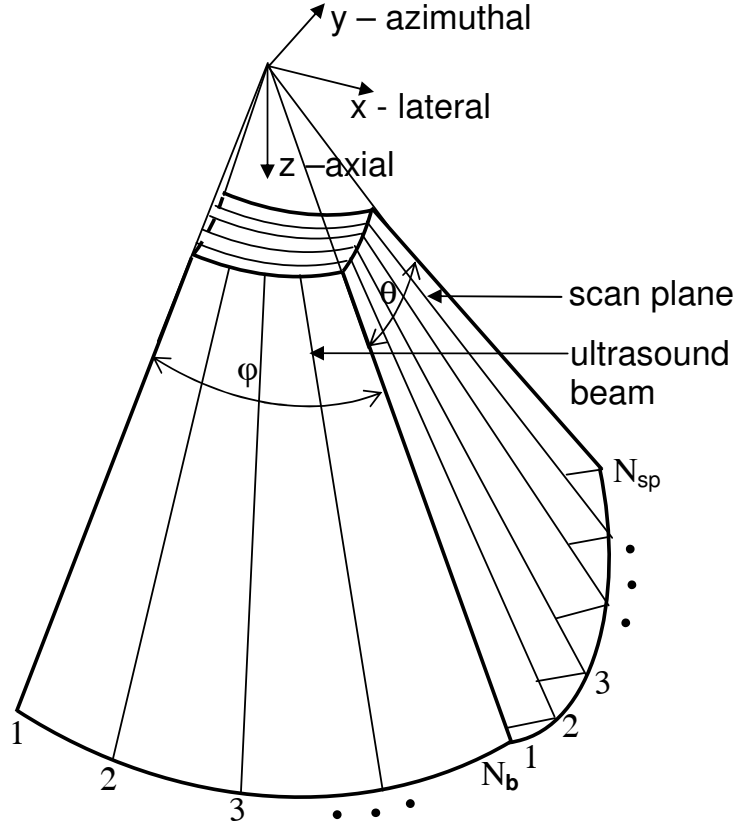


Figure 9.2: *Field of view simulated in FIELD II. The FOV was sampled with $N_{sp} = 53$ sector scan planes each of them composed of $N_b = 71$ ultrasound beams. The tilt angle θ and the scan plane angle φ were both 40° .*

reflection, see Section 3.2.1. The aim of the simulation was to produce 3D ultrasound images that represent a highly scattering metallic electrode located inside a biological tissue. Such medium is composed of two distinct types of diffusers corresponding to the tissue and the electrode. Consequently, two types of diffuser parameters had to be set:

Tissue (background) diffusers. The tissue to scan was modeled by a diffusers distributed in a cuboid with dimensions 50x50x30 mm and the distance from the probe 35 mm, see Figure 9.3. The spatial arrangement and the reflection coefficients of the tissue diffusers were determined from the thesis work of Martin [108]. By minimizing the difference between the simulated and measured RF signals, he determined parameters of tissue diffusers. According to his results, the diffusers were randomly distributed with uniform distribution

and spatial density of 10 diffusers per mm^3 . Their coefficients of reflection were drawn from the K -distribution [43] with density function $P_{cr}(x)$ given by

$$P_{cr}(x) = \frac{2\lambda}{\Gamma(\nu)} \cdot \left(\frac{\lambda x}{2}\right)^\nu \cdot \mathcal{B}_{\nu-1}(\lambda x), \quad (9.8)$$

where $\Gamma(\cdot)$ is the Gamma function, $\mathcal{B}(\cdot)$ is the modified Bessel function of second order and $\nu = 10$, $\lambda = \sqrt{\nu}$ are estimated parameters. To draw a large sample from the K -distribution, we used the Radar Toolbox for MATLAB developed by Glen Davidson¹.

Electrode diffusers The metallic electrode inside the tissue was defined by diffusers located inside a cylinder with diameter 0.3 mm and a linear or curvilinear axis, see Figure 9.3. The cylinder endpoints and its length were modified in the experiments to simulate various electrode lengths and positions. The spatial distribution of electrode diffusers was uniform with the density of 125 diffusers per mm^3 , their coefficients of reflection were 7.5.

The relative position of the FOV and the numerical phantom composed of background and tissue diffusers is depicted in Figure 9.3.

To obtain a simulated 3D ultrasound image, the parameters presented in previous sections were set in the FIELD II functions and the calculation of the radio-frequency signals was executed. Since our FOV was composed of 53 planes each them comprising 71 scan lines, there was a need to compute 3763 signals of approximately 2000 samples. On a standard PC, the computation of RF data took approximately 7 hours. Using the procedure explained in Section 3.1.4, a 3D ultrasound image $V: \mathcal{X} \rightarrow \mathcal{I}$ was reconstructed from the simulated RF signals. The logarithmic compression of the envelope amplitude was omitted to retain the high SNR. In following sections, we present the results of experiments performed on simulated ultrasound images.

9.2.2 Electrode distance from the probe

The electrode is in clinical applications introduced into a specific target place whose distance from the bodily surface varies on case to case basis. The position of the probe changes between acquisitions as well. As a result, the electrode distance from the probe differs.

¹<http://www.radarworks.com>

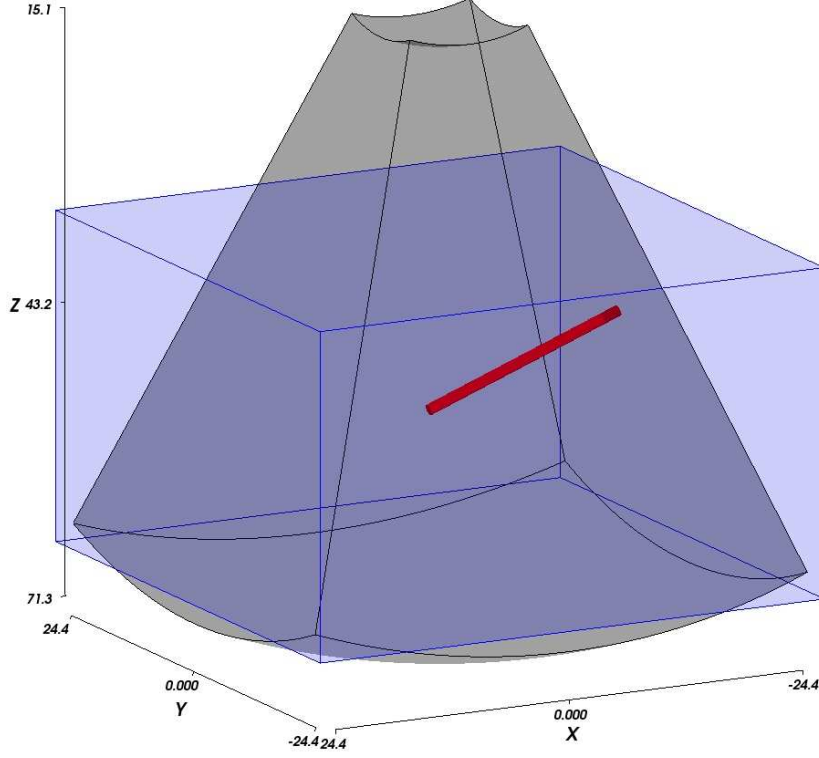


Figure 9.3: *Relative position [in mm] of the simulated components. The numerical phantom is represented as a blue cuboid. Together with the background diffusers, it includes the electrode diffusers located inside the red cylinder. This phantom is scanned with a virtual probe with the FOV marked as a black sphere sector.*

In order to investigate the influence of electrode distance on the localization accuracy, we simulated ultrasound images where the electrode appears at various distance from the probe while keeping the electrode orientation fixed. The electrode position d_I was measured as the Euclidean distance of the intercept point E_I from the probe, that is $d_I = \|E_I\|$. The depth of penetration L of the electrode in the FOV was set 20 mm. The electrode orientation was controlled by the angle ω between the positive half axis z and the directional vector given by $E_T - E_I$, see Figure 9.4. Figure 9.5 depicts an example of such image for $d_I = 61$ mm. We assume that changing d_I should not have significant effect on the algorithm performance.

The electrode axis in the images was found using the PIP method (Chapter 6) and the model fitting algorithms (Chapter 7) with different models (Section 7.2), which are in the text denoted by MF1, MF2 and MF3. Achieved axis accuracy

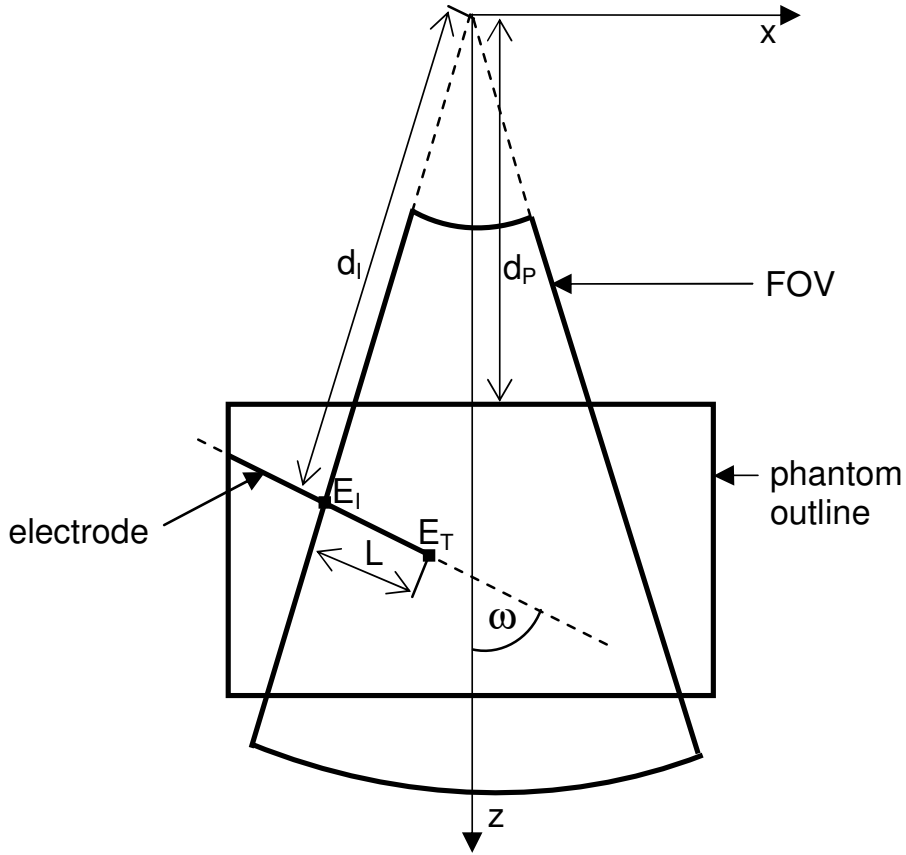


Figure 9.4: *Illustration of the parameters used to control the position of the electrode in the FOV. The angle ω determined the electrode orientation, d_I specified the electrode distance from the probe, L indicated the length of the electrode visible in the image and d_P marked the distance between the probe and the top part of the phantom.*

ε_{axis} with respect to d_I is almost constant for all methods, see Figure 9.6.

Achieved axis accuracy ε_{axis} for each image is depicted in Figure 9.6. We can observe neither method exhibits significant variations, which confirms our hypothesis about the independence of ε_{axis} on the electrode distance from the probe. The electrode axis is most accurately found by MF3 (0.094 ± 0.032 mm) which surpasses the PIP method (0.163 ± 0.028 mm). Let us note the similarity between algorithms the MF1, resp., MF2 where the axis accuracy is 0.410 ± 0.032 mm, resp., 0.397 ± 0.032 mm.

The accuracy of the electrode tip found by the algorithm is shown in Figure 9.7. The results show that ε_{tip} is 0.366 ± 0.036 mm and is independent of the electrode

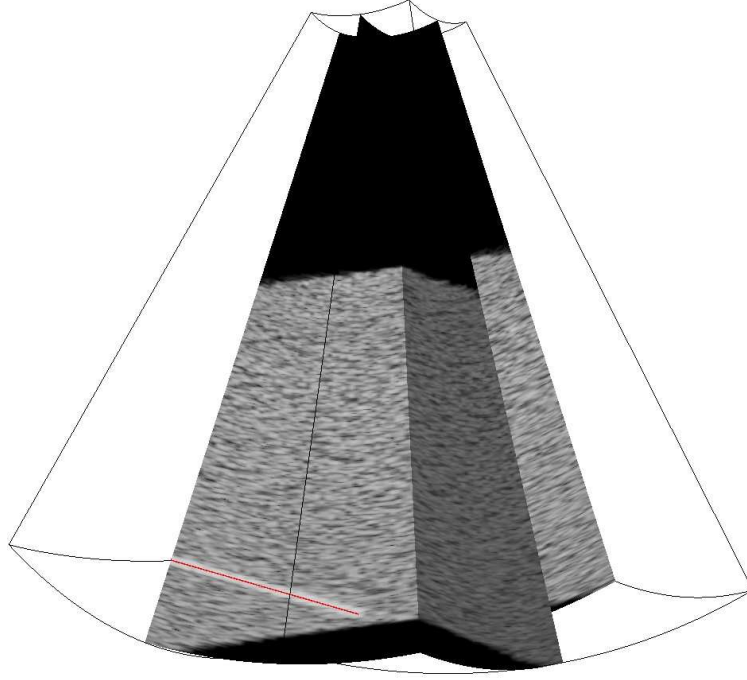


Figure 9.5: *Example of a simulated image, where the distance d_I of the intercept point to the probe is 61 mm.*

distance d_I .

9.2.3 Electrode orientation

In the previous case, we investigated the influence of the distance between the electrode and the axis on the localization accuracy while keeping the electrode angle with respect to the probe fixed. However, the electrode may be introduced into the tissue under different angles and the portion of the tissue may be scanned from several directions.

To experimentally verify the effect of the electrode angle on the localization accuracy, we simulated nine images with a different electrode introduction angle ω (Figure 9.8). The electrode direction was defined by the angle ω between the positive half axis z (probe axis) and the electrode axis given by the intercept E_I and the tip E_T point, see Figure 9.4. The angle ω was varied from 10° to 170° with a 10° increment. In all simulated images, the electrode axis was incident with the plane xz and passed through the focal point located at $[0\ 0\ 50]$ mm; see Figure 9.2 for the specification of the image coordinate system.

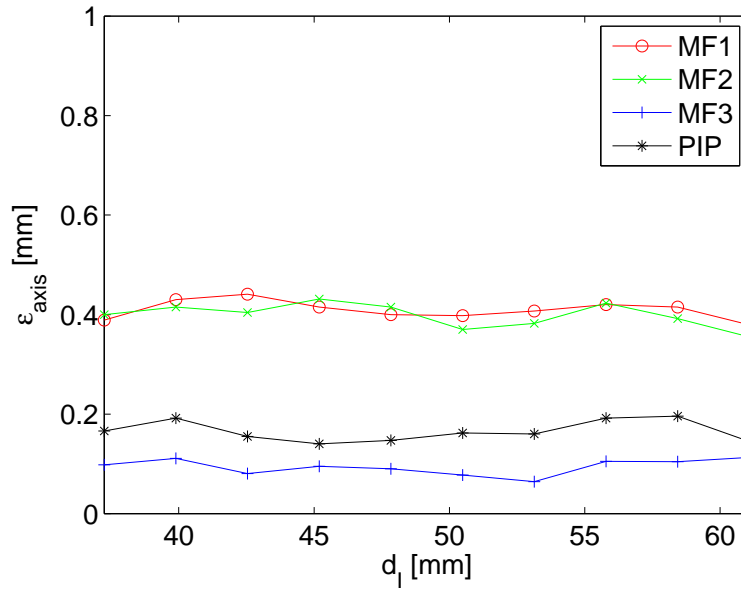


Figure 9.6: *The axis localization accuracy as a function of the intercept-to-probe distance d_I .*

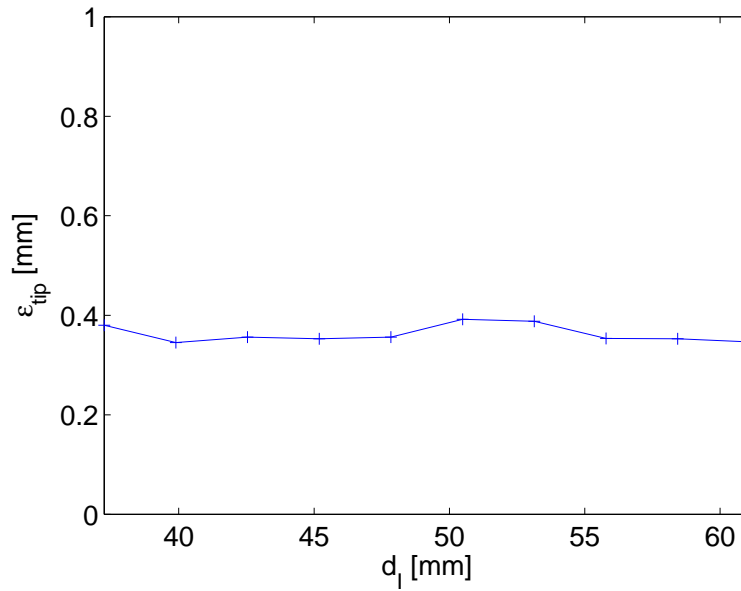


Figure 9.7: *The tip localization accuracy as a function of the intercept-to-probe distance d_I .*

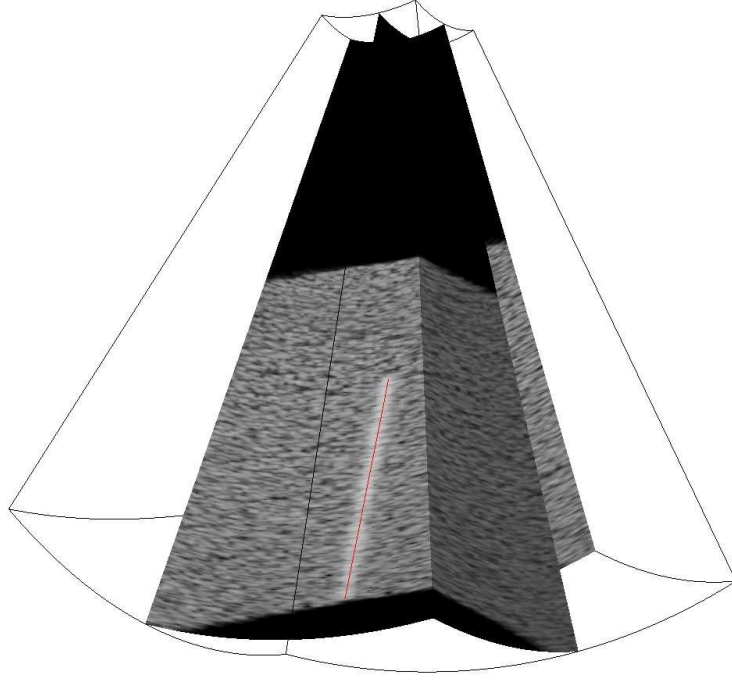


Figure 9.8: An example of a simulated image, where the electrode orientation ω is 170° . Assuming the electrode axis being incident with the plane xz , the angle ω is measured between the positive half-axis z and the vector $E_T - E_I$.

The accuracy of the axis localization algorithms with respect to the angle ω is shown in Figure 9.9. The most accurate estimates of axis position are provided by MF3, resp., the PIP method, where the axis accuracy is 0.1423 ± 0.045 mm, resp., 0.178 ± 0.036 mm. Due to the anisotropic PSF, the resolution of the electrode varies with its orientation. In the case when the electrode axis is perpendicular to the probe axis, e.g., $\omega = 90^\circ$, the edges of the electrode are best defined, because the resolution in the axial direction is superior to the lateral and azimuthal resolution. As a consequence, we can observe the dependence of the axis accuracy ε_{axis} on the angle ω . The best estimates of the electrode axis were obtained for $\omega = 90^\circ$.

The tip localization accuracy ε_{tip} as a function of ω is shown in Figure 9.10. In contrast to axis localization, the tip is most accurately estimated when the electrode axis is parallel with the probe axis.

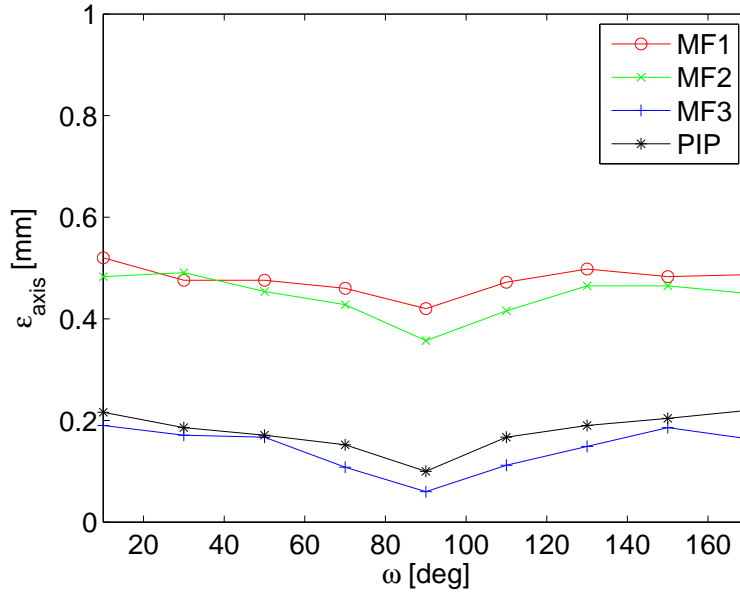


Figure 9.9: *The axis localization accuracy as a function of the electrode orientation ω .*

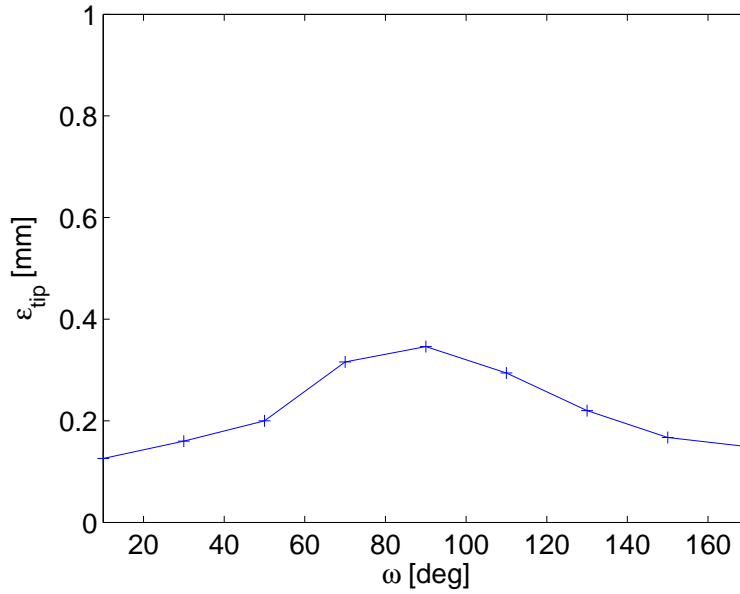


Figure 9.10: *The tip localization accuracy as a function of the electrode orientation ω .*

9.2.4 Electrode length

The length of the electrode segment visible in acquired images varies, which may also influence the localization accuracy. We simulated a number of images where

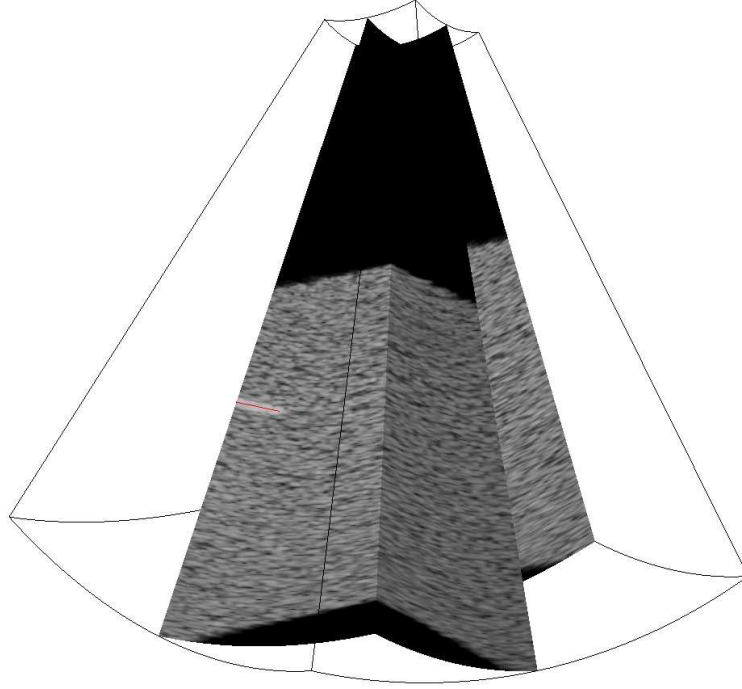


Figure 9.11: *An example of a simulated image, where the visible length L of the electrode in the FOV is 5 mm.*

the electrode length L was varied from 1 to 6 mm with a 0.5 mm increment, see Figure 9.11. The electrode was positioned in the xz plane. The distance d_I of the intercept point from the probe was set to 47 mm and the electrode angle ω was fixed to 70° , see Figure 9.4.

The axis accuracy with respect to L is depicted in Figure 9.12. It shows that the axis accuracy improves as the electrode is introduced into the tissue. For the depth of insertion above 5 mm, the axis accuracy remains the same and is not influenced by the electrode length L . Let us note, that for small L , the MF algorithms give more accurate estimates than the PIP method. The experiments also indicate that the tip accuracy is independent of L , see Figure 9.13.

9.2.5 Background noise

The axis localization algorithms based on model fitting (Chapter 7) and the tip algorithm (Chapter 8) make use of a priori estimated models describing the statistical properties of voxel intensities. However, different ultrasound scanner settings as well as tissue types make the background noise and the electrode voxel intensi-

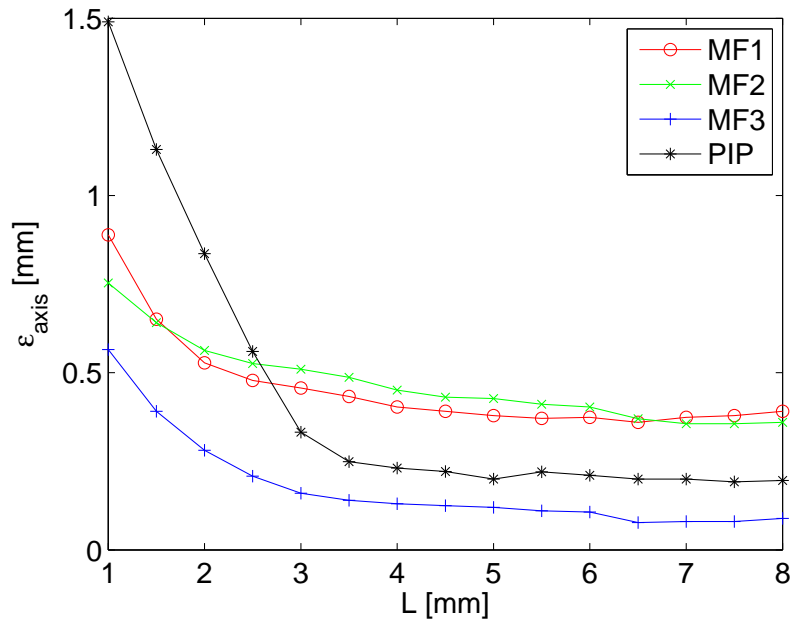


Figure 9.12: *The axis localization accuracy as a function of the electrode length L in the FOV.*

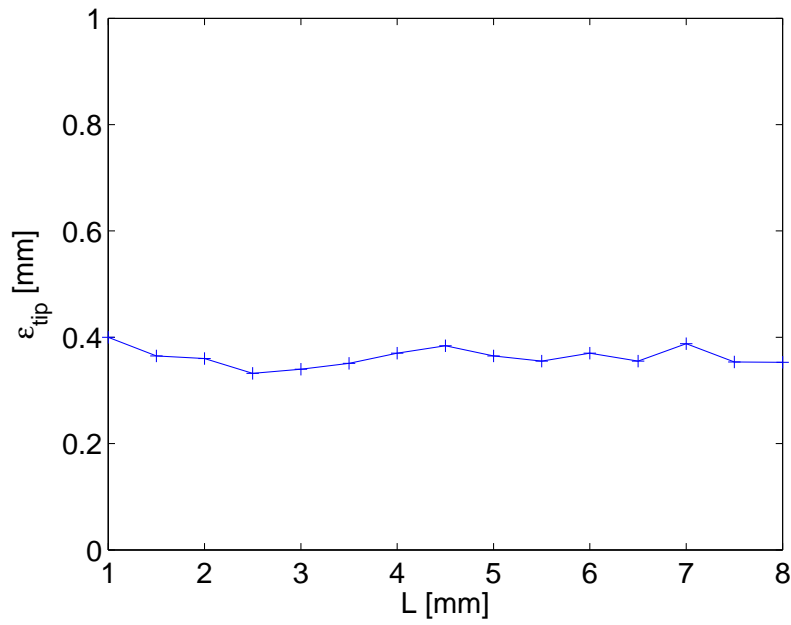


Figure 9.13: *The tip localization accuracy as a function of the electrode length L in the FOV.*

ties vary.

In order to determine, their influence on the localization accuracy, we simulated several ultrasound images with increasing amount of background noise. This was achieved by gradually increasing the parameter λ of the K -distribution that models the reflection coefficients of background diffusers, see Equation (9.8). The signal-to-noise (SNR) ratio was calculated as

$$\text{SNR} = 10 \log_{10} \frac{\frac{1}{|\mathcal{X}_{el}|} \sum_{\mathbf{x} \in \mathcal{X}_{el}} V^2(\mathbf{x})}{\frac{1}{|\mathcal{X}_{bg}|} \sum_{\mathbf{x} \in \mathcal{X}_{bg}} V^2(\mathbf{x})} \text{ [dB]}, \quad (9.9)$$

where the numerator, resp., the denominator is the intensity power of the electrode voxels \mathcal{X}_{el} , resp., the background voxels \mathcal{X}_{bg} . Voxels were classified into \mathcal{X}_{el} , resp., \mathcal{X}_{bg} based on whether their distance from the true axis were smaller, resp., greater than ρ which was set to 1 mm. The reflection coefficients of electrode diffusers were set to 7.5 for all simulated images. An electrode of length $L = 20$ mm was positioned in the plane xz , with the intercept point distance $d_I = 47$ mm and the orientation angle $\omega = 40^\circ$, see Figure 9.14.

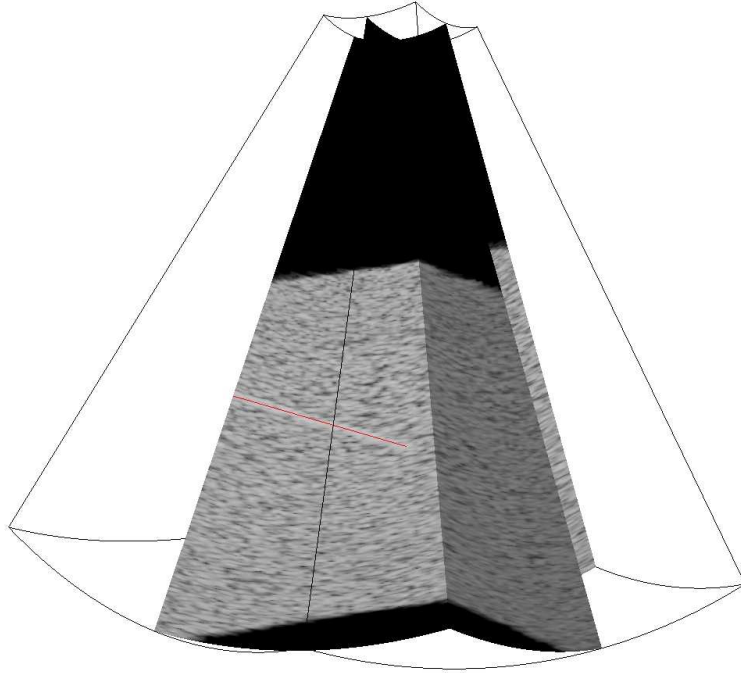


Figure 9.14: *An example of a simulated image, where the SNR is 12.1 dB.*

Figure 9.15 and 9.16 shows the axis and the tip localization accuracy as a function of the image SNR. The accuracy of the MF algorithms deteriorates sharply

as the image SNR decreases under certain value: 13 dB for MF1, 16 dB for MF2 and 12.5 dB for MF3. The accuracy of PIP is not significantly influenced by the background noise intensity.

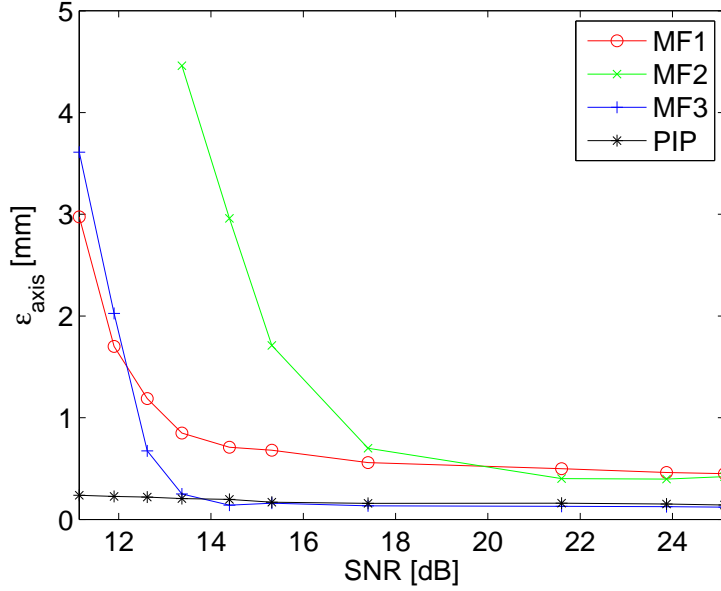


Figure 9.15: *The axis localization accuracy as a function of the image SNR.*

9.2.6 Curved electrode

The model fitting methods (Chapter 7) were developed to estimate the axis of a curved electrode. In this section, we examine the localization accuracy of the MF methods on a curved electrode and compare it to the results obtained by PIP (Chapter 6), which assumes the axis to be straight.

For this purpose, we simulated several images while increasing the curvature of the electrode axis modeled by a parabolic curve. The parabola was determined by the intercept point E_I , the electrode tip E_T and a bending offset o_{axis} that controlled the axis curvature, see Figure 9.17. o_{axis} was varied from 0 to 3 mm with a 0.2 mm increment. Figure 9.18 shows an example of a curved electrode for $o_{axis} = 3$ mm. The electrode length L was fixed to 20 mm and the intercept point distance $d_I = 55$ mm. The angle ω between the z -axis and the tangent to the axis at the intercept E_I was set to 70° .

Figure 9.19 and 9.20 illustrates the dependence of the localization accuracy

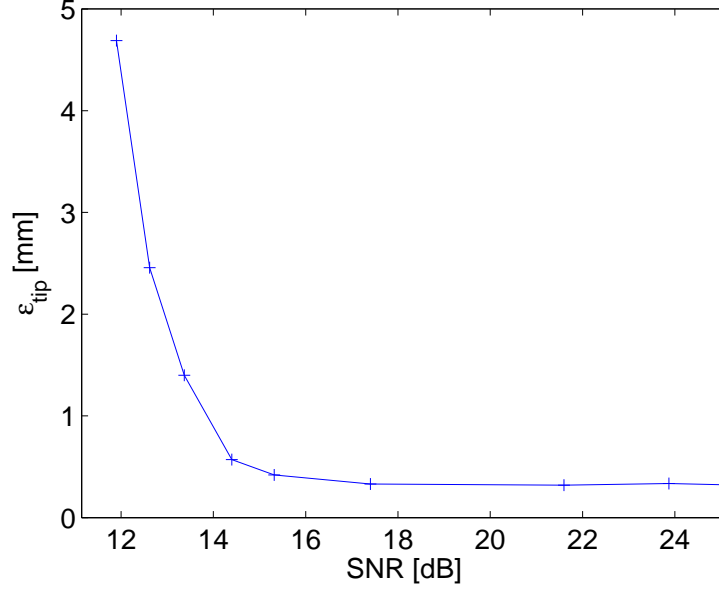


Figure 9.16: *The tip localization accuracy as a function of the image SNR.*

on the bending offset o_{axis} . The MF algorithms designed to localize a curved electrode provide good axis estimates in the whole range of o_{axis} . However, the PIP algorithm is not suitable for localizing curved electrode.

9.3 Real 3D ultrasound images

The proposed methods were tested on real ultrasound data as well. An ultrasound system was employed to scan a tissue mimicking phantom that contained a thin metallic electrode, see Section 9.3.1. Acquired images were consequently processed by the localization algorithms to estimate the electrode position with respect to the image coordinate system. Results of the experiments are summarized in Section 9.3.2.

9.3.1 Acquisition of ultrasound images

The experimental setup used to acquire ultrasound images is depicted in Figure 9.21. It was composed of an ultrasound scanner with a 3D ultrasound probe, a water tank containing the phantom and a computer connected to the scanner.

Ultrasound scanner. The phantom was scanned by the scanner KRETZ Volu-

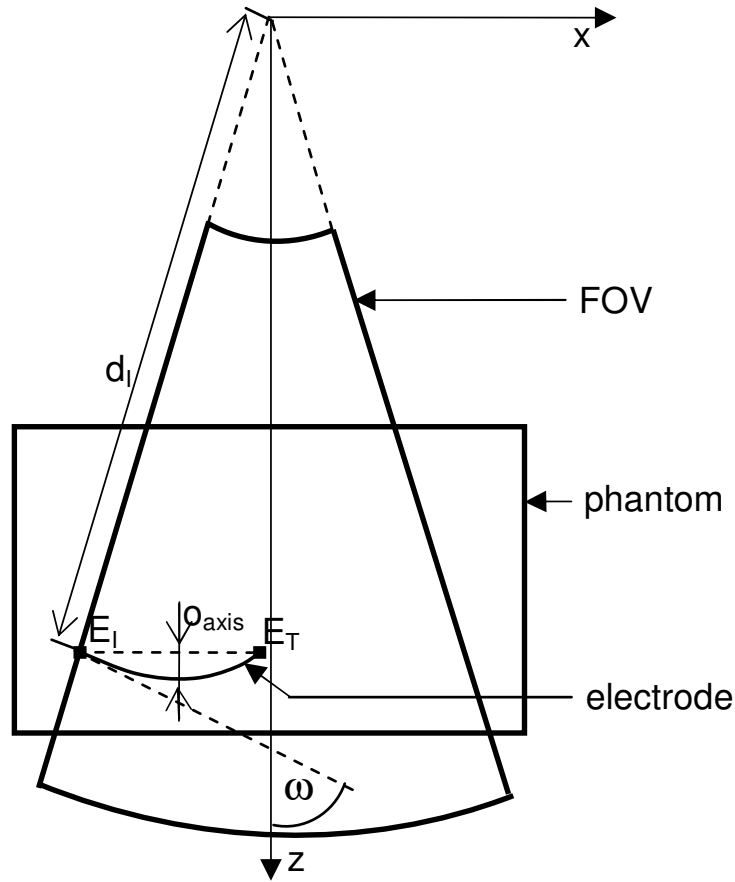


Figure 9.17: *Illustration of the parameters that controlled the electrode position and the axis shape in the FOV. The parameter d_I specified the distance of the electrode from the probe, ω determined the electrode orientation and o_{axis} determined the bending of the electrode axis.*

son 530D (GE Medical Systems², Kretz Ultrasound, Zipf, Austria), which is a medical diagnostic system that combines 2D and 3D imaging capabilities. In addition to the visualization, it possesses a number of operation modes to help the diagnostic of internal body structures such as the tissue harmonic imaging, spectral Doppler, color flow imaging. Mari [7] developed a built-in card that provides access to the discretized RF signal that comes out of the ultrasound probe. The RF signal is discretized at 27 MHz and transferred to the computer connected to the scanner for further processing.

²<http://www.gehealthcare.com/usen/ultrasound>

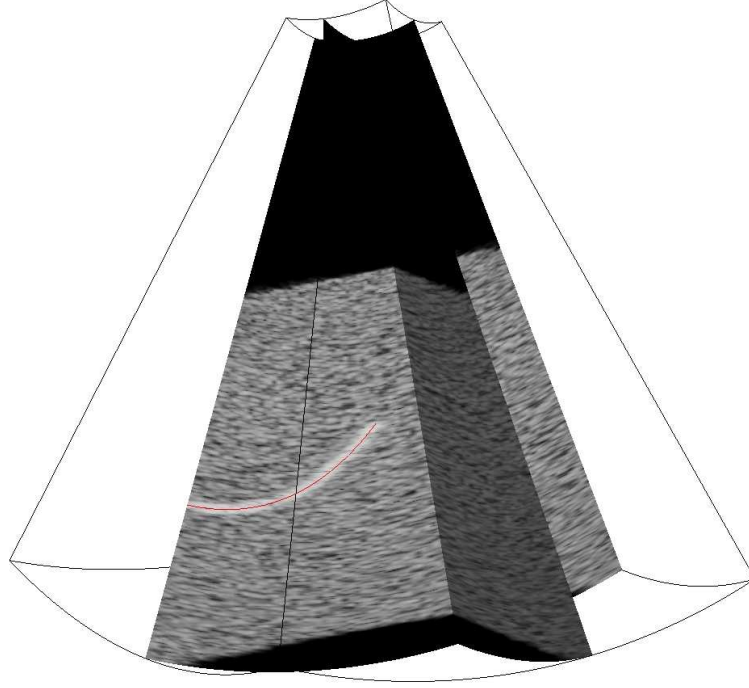


Figure 9.18: An example of a curved electrode with the bending offset $o_{axis} = 3 \text{ mm}$.

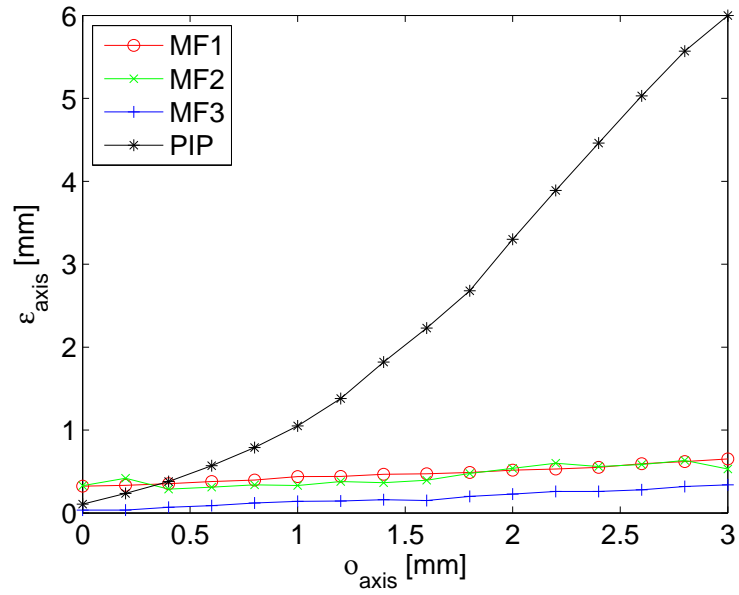


Figure 9.19: The axis localization accuracy as a function of the electrode axis curvature o_{axis} .

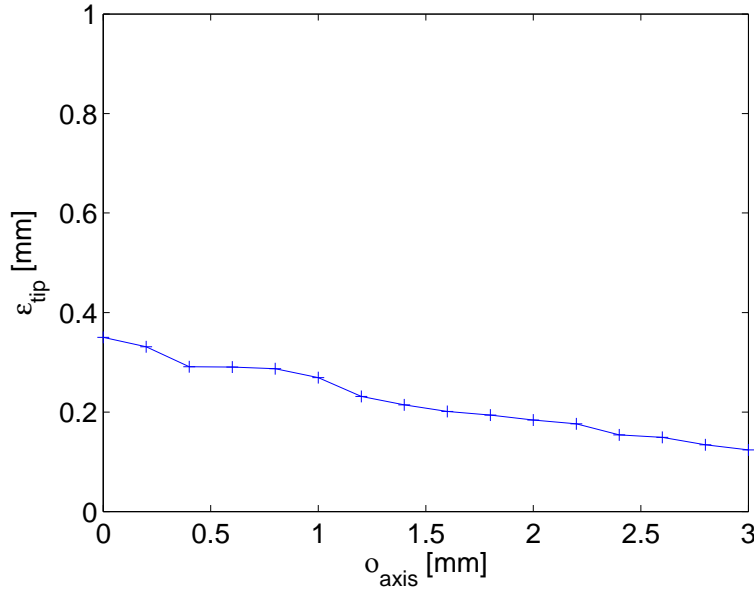


Figure 9.20: *The tip localization accuracy as a function of the electrode axis curvature o_{axis} .*

Ultrasound probe. The scanner is equipped with a 3D transvaginal probe S-VDW5-8B. It is a sector probe composed of 128 elements with a mechanically tilted scan plane. The probe can operate in the frequency range from 4 to 10.5 MHz. We have used the central frequency 7.5 MHz. The field of view is determined by the scan angle and the tilt angle that are both adjustable. The maximum scan, resp., tilt angle is 140° , resp., 95° . The depth of scanning is limited to 80 mm and the scanner can provide frames (scan planes) with rate of up to 50 per second.

Phantom. Biological tissue was simulated by a polyvinyl alcohol (PVA) cryogel phantom with dimensions 45x45x55 mm, see Figure 9.22. The phantom was made from a 10% polyvinyl alcohol diluted in water and solidified through a freeze-thaw process. After the solidification, this material exhibits acoustic properties similar to a biological tissue. Experiments show [109] that the speed of sound in a PVA phantom is from 1520 to 1540 $\text{m}\cdot\text{s}^{-1}$ and the attenuation coefficients are in the range from 0.075 to 0.28 $\text{dB}\cdot\text{cm}\cdot\text{MHz}^{-1}$.

Electrode. A thin metallic electrode was introduced inside the phantom into the depth of approximately 20 mm. We used the microelectrode 96 MM/NO

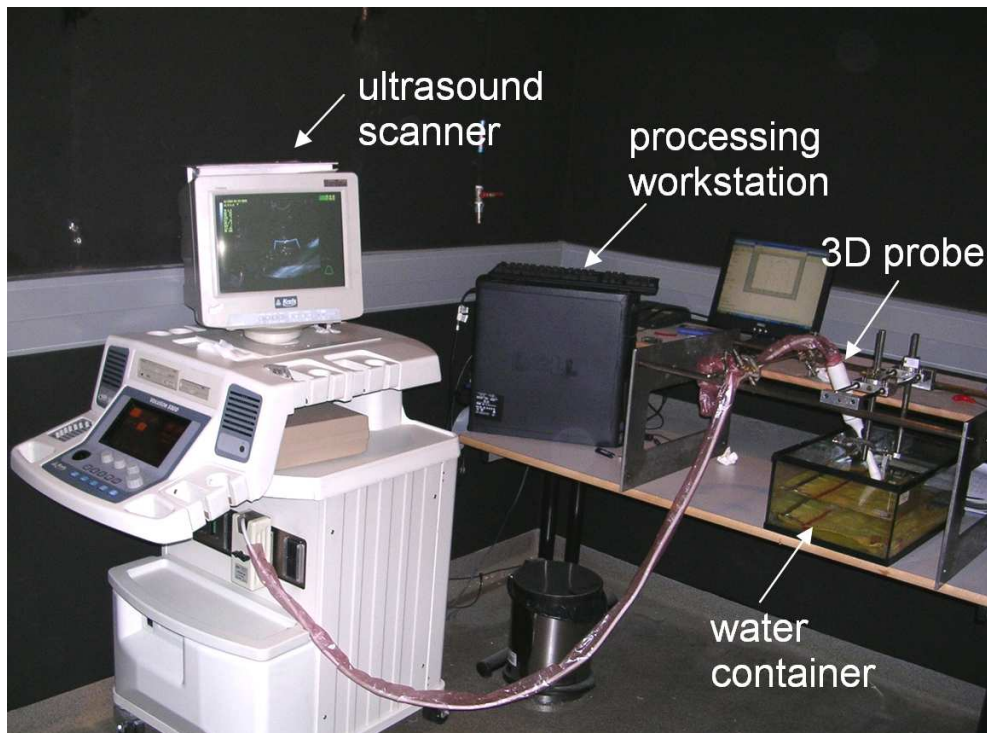


Figure 9.21: *The hardware setup used to acquire real ultrasound data. The cryogel phantom containing a metallic electrode was placed into a water filled container and scanned with a 3D ultrasound scanner KRETZ Voluson 530D. Ultrasound images were reconstructed from received RF signals on a computer connected to the scanner.*

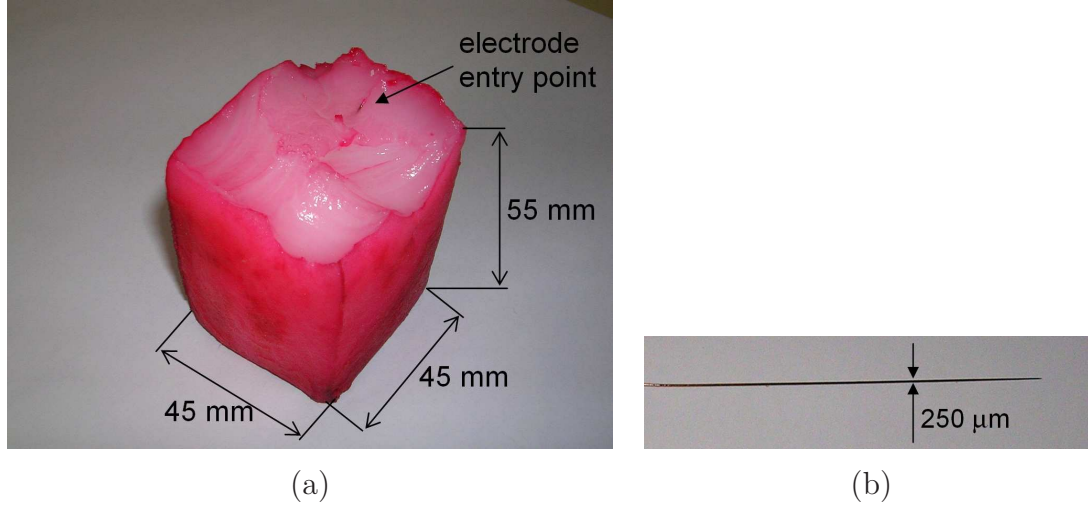


Figure 9.22: (a) Polyvinyl alcohol cryogel phantom used to imitate the acoustic properties of biological tissue. (b) A tungsten electrode that was introduced into the phantom prior to scanning.

ZAP³, which is employed in neurological research for a single cell recording. The electrode is made of tungsten with glass insulation and a short, concave shaped tip. The electrode is 120 mm long and has 250 μm diameter, Figure 9.22.

Prior to scanning, a water container was filled with water and the phantom was placed inside, see Figure 9.23. The head of the ultrasound probe was placed into the water to ensure the acoustic impedance matching between the probe and the phantom. The probe was positioned so that the FOV covered the phantom. The total tilt angle θ and scan plane angle φ were both set on the ultrasound scanner to 40°. The depth of penetration was 7 cm. After the initiation of scanning, we acquired 3763 RF signals corresponding to 53 scan planes each composed of 71 scan beams. They were transferred to the computer and stored on the disk. Using the procedure explained in Section 3.1.4, an ultrasound image $V: \mathcal{X} \rightarrow \mathcal{I}$ was reconstructed. As well as in the case of image reconstruction from simulated RF data, the logarithmic compression of the envelope amplitude was omitted to retain high SNR.

³<http://www.fh-co.com>

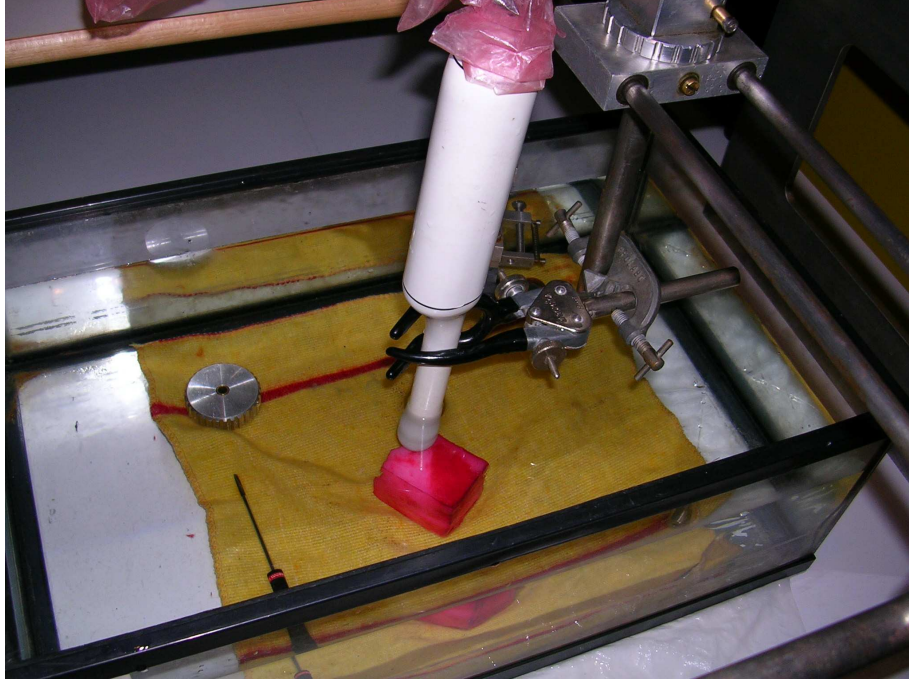


Figure 9.23: *The head of the ultrasound probe and the phantom were placed into a water filled container to ensure acoustic impedance matching.*

9.3.2 Localization results

Using the procedure described in Section 9.3.1, we acquired 3D images (Figure 9.24) for different phantom orientations and distances from the probe. The true electrode position in real images is not known. Assuming that the electrode is straight in the phantom, we defined its position by the intercept and tip point that were manually identified in each dataset. These endpoints served as the reference to evaluate the axis and the tip localization accuracy. Parameters that characterize the position of the phantom and the electrode with respect to the FOV are summarized in Table 9.2.

The axis was most accurately found by the PIP method (0.285 ± 0.019 mm) and the MF3 algorithm (0.346 ± 0.016 mm), see Figure 9.25. The localization accuracy of the axis estimated by MF2, resp., MF1 was 0.346 ± 0.016 mm, resp., 0.528 ± 0.025 mm. The electrode tip localization accuracy was 0.325 ± 0.035 mm, see Figure 9.26.

image ID	d_I [mm]	ω [deg]	L [mm]	d_P [mm]
1	39.5	73.5	20.6	31.1
2	48.0	73.0	20.9	41.3
3	41.3	70.0	22.2	35.1
4	48.8	68.2	20.5	43.8
5	41.6	80.0	20.3	33.5
6	51.8	80.0	21.1	43.1
7	48.3	80.3	21.8	24.1
8	54.4	80.3	21.4	30.4

Table 9.2: *Specification of the electrode and phantom position in acquired 3D images. d_I distance of the intercept point from the probe; ω angle between the electrode axis and the probe axis; L electrode length visible in the FOV; d_P distance of the upper part of the phantom from the probe.*

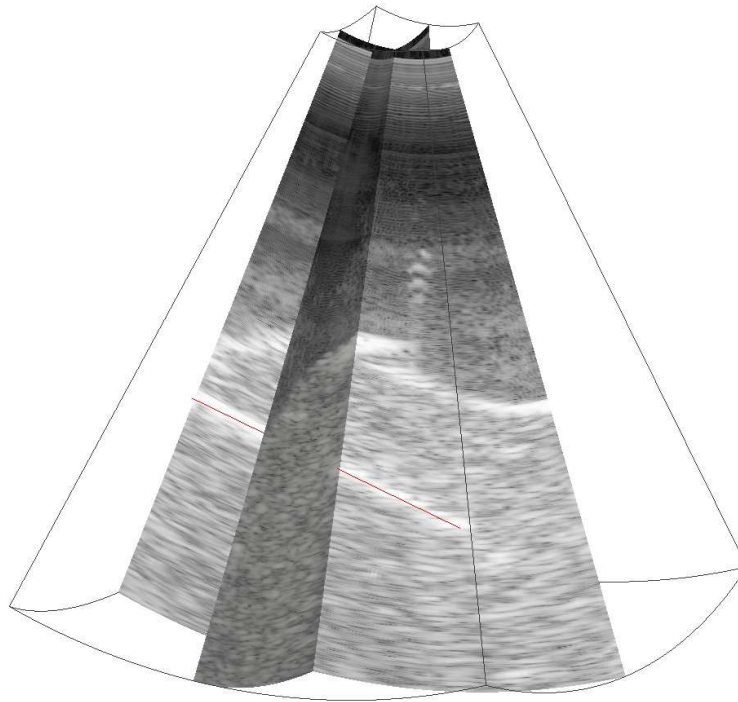


Figure 9.24: *Ultrasound image acquired by scanning the cryogel phantom. From the speckle pattern, we can distinguish the region of water, the phantom and the electrode.*

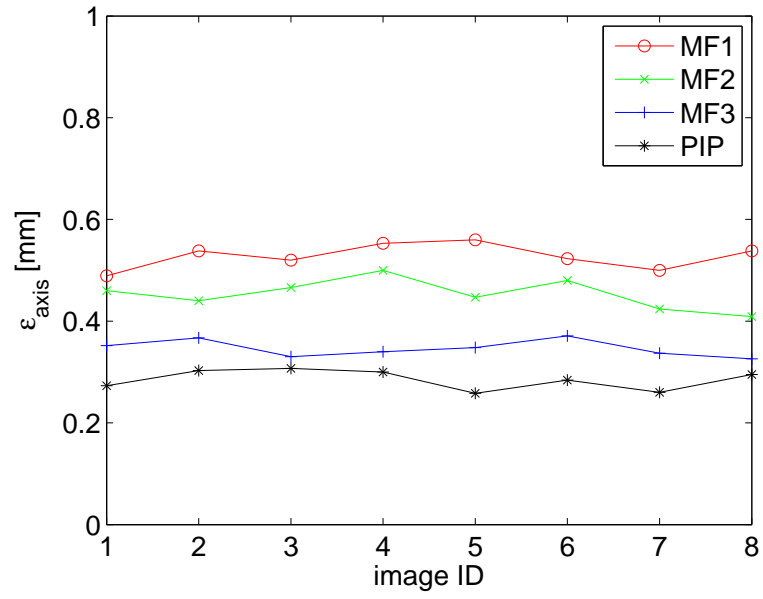


Figure 9.25: *The accuracy of the estimated electrode axis on a set of real 3D ultrasound images.*

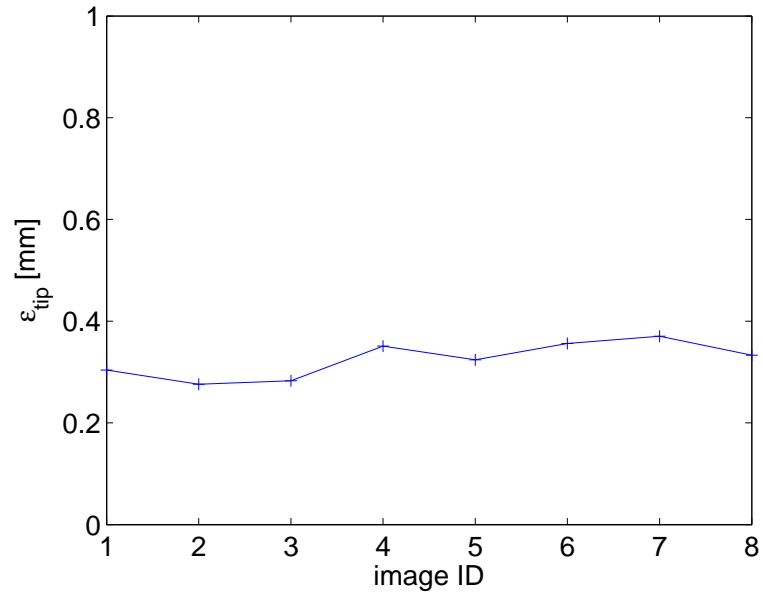


Figure 9.26: *The accuracy of the estimated electrode tip on a set of real 3D ultrasound images.*

9.4 Implementation and computational time

In order to specify the processing time, the localization methods were implemented in MATLAB and the real ultrasound images described in Section 9.3 were used as testing data. The size of each image was 53x71x2500 voxels and the testing was done on a standard computer with a 1.7 GHz processor and 1.5 GB memory. The amount of time needed to identify the electrode in each image is summarized in Table 9.3. It indicates that the processing time of the methods based on the model fitting is of the order of seconds. These methods are faster than the PIP algorithm with an average processing time of about 20 minutes.

However, it should be noted that the algorithms were executed in MATLAB and significant reduction in processing time should be achieved by an implementation in a procedural language such as C++.

image ID	MF1 [s]	MF2 [s]	MF3 [s]	PIP [s]
1	3.8	7.8	8.2	1212
2	2.7	6.6	10.9	1272
3	4.6	9.4	7.1	1392
4	2.2	7.6	8.8	1206
5	4.9	12.3	9.1	1470
6	2.3	8.9	7.9	1194
7	3.9	11.0	12.6	1362
8	3.7	10.6	8.1	1278
	3.5±1.0	9.3±2.0	9.1±1.8	1298±100

Table 9.3: *Processing time. The proposed methods were implemented in MATLAB and tested on real ultrasound images described in Section 9.3.*

Chapter 10

Conclusions

In this thesis, we addressed the problem of robustly estimating the position of an electrode-like object in a 3D ultrasound image. This research was motivated by the development of an ultrasound imaging system whose goal is to automatically identify an electrode inside the tissue. The task of localizing the electrode was decomposed into the detection of the electrode axis and the tip. Three algorithms were proposed to solve these subtasks.

The axis of a straight electrode can be found by maximizing the parallel projection, which we described by the Parallel Integral Projection transform (Chapter 6). To accelerate the search for the maximum, a hierarchical mesh-grid method was implemented. The experiments showed that the localization accuracy is comparable to the axial resolution of the ultrasound system and is better than the accuracy of the state of the art algorithms. We further demonstrated that this approach, which does not require any prior information about the voxel intensities, is very robust against the background noise. However, the computational cost does not permit real-time localization. In order to reduce the processing time, we consider to improve this method by processing smaller datasets that are obtained by sub-sampling the original image at different scales.

An algorithm based on the model fitting paradigm was implemented to determine the axis of a curved electrode (Chapter 7). Three distinct models were tested to model the geometrical shape of the electrode and the intensity distribution. The model parameters were robustly estimated by the R-RANSAC estimator. Final optimization based on the Nelder-Mead simplex method further improved the axis accuracy. This method represents a contribution to the state of the art by permitting to identify a curved electrode in a 3D ultrasound image with a very high

accuracy. A low computational cost permits to perform the localization task in near real-time. To avoid the need of establishing prior intensity distributions, we shall further study the possibility of an automatic retrieval of the models in an iterative manner.

The electrode tip is found by thresholding the intensity along the estimated axis with an optimized threshold while taking into account high intensity variations that cause apparent electrode interruptions (Chapter 8).

To conclude, we have developed three algorithms that serve for the localization of a straight or curved electrode in a 3D ultrasound image. The experiments carried out on simulated and real ultrasound images showed that the accuracy of the methods is comparable to the axial resolution of the ultrasound system. Low computational cost of the order of seconds permits fast data processing.

Appendix A

Author's publications

1. Martin Barva, Jan Kybic, Jean-Martial Mari, Jean René Duhamel, Christian Cachard, and Václav Hlaváč. Parallel integral projection transform for electrode localization in 3D ultrasound images. *IEEE Transactions on Ultrasonics, Ferroelectrics and Frequency Control*, 2007. (submitted).
2. Martin Barva, Jan Kybic, and Václav Hlaváč. Localization of surgical instruments in biological tissue from 3D ultrasound images. In *CTU 2007: Proceedings of the Czech Technical University Workshop 2007*, volume 11, pages 480–481, Technická 2, Prague, Czech Republic, February 2007. Czech Technical University in Prague, Czech Technical University.
3. Martin Barva, Jan Kybic, Hervé Liebgott, Christian Cachard, and Václav Hlaváč. Comparison of methods for tool localization in biological tissue from 3D ultrasound data. In *Proceedings of IEEE Ultrasonics Symposium*, pages 1983–1986, October 2006.
4. Martin Barva, Jan Kybic, Jean-Martial Mari, Christian Cachard, and Václav Hlaváč. Localizing metal electrode from 3D ultrasound data using RANSAC and intensity priors. In Jiří Hozman and Peter Kneppo, editors, *IFMBE: Proceedings of the 3rd European Medical and Biological Engineering Conference - EMBEC*, volume 11, pages 1–6, Prague, Czech Republic, November 2005. IFMBE.
5. Martin Barva, Jan Kybic, Jean-Martial Mari, Christian Cachard, and Václav Hlaváč. Automatic localization of curvilinear object in 3D ultrasound images. In William F. Walker and Stanislav Y. Emelianov, editors, *Medi-*

- cal Imaging 2005: Ultrasonic Imaging and Signal Processing*, volume 6 of *Progress in Biomedical Optics and Imaging*, pages 455–462, Washington, USA, July 2005. SPIE.
6. Martin Barva, Jan Kybic, and Václav Hlaváč. Automatic object localization from 3D ultrasound data (Ph.D. thesis proposal). Research Report CTU–CMP–2005–04, Center for Machine Perception, K13133 FEE Czech Technical University, Prague, Czech Republic, February 2005.
 7. Martin Barva, Jan Kybic, Jean-Martial Mari, and Christian Cachard. Radial Radon transform dedicated to micro-object localization from radio frequency ultrasound signal. In Marjorie Passini Yuhas, editor, *Proceedings of IEEE Ultrasonics, Ferroelectrics and Frequency Control Symposium*, pages 1836–1839, New York, USA, August 2004. IEEE.
 8. Martin Barva, Jean-Martial Mari, Jan Kybic, and Christian Cachard. Radial Radon transform for electrode localization in biological tissue. In Jiří Jan, Jiří Kozumplík, and Ivo Provazník, editors, *BIOSIGNAL: Analysis of Biomedical Signals and Images*, pages 299–301, Brno, Czech Republic, June 2004. EURASIP, VUTIU Press.

Bibliography

- [1] V. Horsley, , and R. H. Clarke. The structure and functions of the cerebellum examined by a new method. *Brain*, 31:45–124, 1908.
- [2] P. L. Gildenberg. *Stereotactic Surgery: Present and Past*. Williams and Wilkins, Baltimore, 1988.
- [3] L. S. Scott, P. Douglas, G. H. Baltuch, and J. L. Jaggi. Error analysis of MRI and Leksell stereotactic frame target localization in deep brain stimulation surgery. *Stereotactic and functional neurosurgery*, 83(1):1–5, 2005.
- [4] H. Zhang, F. Banovac, R. Lin, N. Glossop, B. J. Wood, D. Lindisch, E. Levy, and K. Cleary. Electromagnetic tracking for abdominal interventions in computer aided surgery. *Computer Aided Surgery*, 11(3):127–136, May 2006.
- [5] M. Felber. *Optical measurement system for medical applications*. PhD thesis, Swiss Federal Institute of Technology, Lausanne, Switzerland, 2002.
- [6] A. Pascual-Leone, N. Davey, J. Rothwell, E. Wasserman, and B. K. Puri. *Handbook of Transcranial Magnetic Stimulation*. Hodder Arnold Publication, 2002.
- [7] J. M. Mari and C. Cachard. Acquire real-time RF digital ultrasound data from a commercial scanner. *Electronic Journal “Technical Acoustics”*, 3, 2007.
- [8] M. P. Wells and M. Bradley. *Surgical Instruments: A Pocket Guide*. W.B. Saunders Company, 1998.
- [9] H. Gharib and J. R. Goellner. Fine-needle aspiration biopsy of the thyroid: An appraisal. *Annals of Internal Medicine*, 118(4):282–289, February 1993.

- [10] H. J. Wanebo, P. S. Feldman, M. C. Wilhelm, J. L. Covell, and R. L. Binns. Fine needle aspiration cytology in lieu of open biopsy in management of primary breast cancer. *Annals of Surgery*, 199(5):569–579, May 1984.
- [11] G. S. Merrick, W. M. Butler, K. E. Wallner, R. W. Galbreath, and E. Adamovich. Monotherapeutic brachytherapy for clinically organ-confined prostate cancer. *West Virginia Medical Journal*, 101(4):168–171, August 2005.
- [12] D. C. Brooks. *Current Review of Minimally Invasive Surgery*. Springer, 1998.
- [13] A. S. Mandir, L. H. Rowland, P. M. Dougherty, and F. A. Lenz. Microelectrode recording and stimulation techniques during stereotactic procedures in the thalamus and pallidum. *Advances in Neurology*, 74:159–165, 1997.
- [14] R. L. Alterman, D. Sterio, A. Beric, and P. J. Kelly. Microelectrode recording during posteroventral pallidotomy: impact on target selection and complications. *Neurosurgery*, 44(2):315–321, February 1999.
- [15] L. Bernays and H. G. Imhof. *Intraoperative Imaging in Neurosurgery: MRI, CT, Ultrasound*. Springer, 2002.
- [16] E. C. Pua, M. P. Fronheiser, J. R. Noble, E. D. Light, P. D. Wolf, D. von Allmen, and S. W. Smith. 3-D ultrasound guidance of surgical robotics: a feasibility study. *IEEE Transactions on Ultrasonics, Ferroelectrics, and Frequency Control*, 53(11):1999–2008, November 2006.
- [17] J. Stoll, P. Novotny, R. Howe, and P. Dupont. Real-time 3D ultrasound-based servoing of a surgical instrument. In *Proceedings of the IEEE International Conference on Robotics and Automation*, pages 613–618, 2006.
- [18] G. Eggers, T. Salb, H. Hoppe, L. Kahrs, S. Ghanai, G. Sudra, J. Raczowsky, R. Dillmann, H. Worn, S. Hassfeld, and R. Marmulla. Intraoperative augmented reality: the surgeons view. *Studies in Health Technology and Informatics*, 111:123–125, 2005.
- [19] B. A. J. Angelsen. *Ultrasound Imaging – Waves, Signals, and Signal Processing*, volume I. Emantes, Norway, 2000.

- [20] P. M. Morse and K. U. Ingard. *Theoretical Acoustics*. Princeton University Press, 1986.
- [21] S. Gefen, O. Tretiak, C. W. Piccoli, and K. Donohue. ROC analysis of ultrasound tissue characterization classifiers for breast cancer detection. *IEEE Transactions on Medical Imaging*, 22(2):170–177, January 2003.
- [22] U. R. Abeyratne, A. P. Petropulu, and J. M. Reid. Higher-order statistics for tissue characterization from ultrasound images. In *IEEE Signal Processing Workshop on Higher-Order Statistics*, pages 72–76, Washington, DC, USA, July 1997. IEEE Computer Society.
- [23] J. M. Girault, F. Ossant, and A. Ouahabi. Time-varying autoregressive spectral estimation for ultrasound attenuation in tissue characterization. *IEEE Transactions on Ultrasonics, Ferroelectrics and Frequency Control*, 45(3):650–659, May 1998.
- [24] P. Shanker, P. Krishna, and L. Newhouse. Advantages of subharmonic over second harmonic backscatter for contrast to tissue echo enhancement. *Ultrasound in Medicine and Biology*, 24(3):395–399, 1998.
- [25] F. Forsberg and W. Shi. Implementation of subharmonic imaging. In *IEEE Ultrasonics Symposium*, volume 2, pages 1673–1676.
- [26] F. Tranquart, N. Grenier, V. Eder, and L. Pourcelot. Clinical use of ultrasound tissue harmonic imaging. *Ultrasound in Medicine and Biology*, 25(6):889–894, 1999.
- [27] B. A. J. Angelsen. *Ultrasound Imaging – Waves, Signals, and Signal Processing*, volume II. Emantes, Norway, 2000.
- [28] J. A. Jensen. User’s guide for the Field II program. Research Report 2.86, Technical University of Denmark, August 2001.
- [29] M. L. Skolnick. Estimation of ultrasound beam width in the elevation (section thickness) plane. *Radiology*, 180:286–288, 1991.
- [30] B. Richard and B. Robert. Elevation beam profile measurement : a simple test object for evaluation of arrays and 3D imaging performance. In *Proceedings of IEEE Ultrasonic Symposium*, volume 2, pages 1857–1860, 1998.

- [31] J. A. Jensen and Munk P. Computer phantoms for simulating ultrasound B-mode and CFM images. *Acoustical Imaging*, 23:75–80, 1997.
- [32] J. A. Jensen. Field: A program for simulating ultrasound systems. *Medical and Biological Engineering and Computing*, 34(1):351–353, 1997.
- [33] J. A. Jensen. Linear description of ultrasound imaging systems. Research Report 1.01, Technical University of Denmark, June 1999.
- [34] P. R. Stepanishen. Pulsed transmit/receive response of ultrasonic piezoelectric transducers. *Journal of the Acoustical Society of America*, 69(6):1815–1827, June 1981.
- [35] M. A. Fischler and R. C. Bolles. Random sample consensus: A paradigm for model fitting with applications to image analysis and automated cartography. *Communications of the ACM*, 24(6):381–395, June 1981.
- [36] P. H. S. Torr and A. Zisserman. MLESAC: A new robust estimator with application to estimating image geometry. *Computer Vision and Image Understanding*, 78(1):138–156, April 2000.
- [37] J. Matas and O. Chum. Randomized ransac with $t(d,d)$ test. *Image and Vision Computing*, 22(10):837–842, September 2004.
- [38] O. Chum. *Two-view geometry estimation by random sample and consensus*. PhD thesis, Czech Technical University in Prague, Prague, Czech Republic, 2005.
- [39] B. Bijmens. *Exploiting radiofrequency information in echocardiography*. PhD thesis, Katholieke Universiteit te Leuven, Leuven, Belgium, 1997.
- [40] B. Bijmens, M. V. Hamme, J. Vandekerckhove, M. C. Herregods, J. Nuyts, P. Suetens, and F. V. Werf. Segmentation of echocardiographic images using classification in the radiofrequency feature space. In *Proceedings Computers in Cardiology*, pages 733–736, September 1995.
- [41] D. Boukerroui, O. Basset, A. Baskurt, and G. Gimenez. A multiparametric and multiresolution segmentation algorithm of 3D ultrasonic data. *IEEE Transactions on Ultrasonics, Ferroelectrics, and Frequency Control*, 48(1):64–77, 2001.

- [42] I. Dydenko, D. Friboulet, J. M. Gorce, J. D'hooge, B. Bijnens, and Magnin. I. E. Towards ultrasound cardiac image segmentation based on the radiofrequency signal. *Medical Image Analysis*, 7:353–367, 2003.
- [43] O. Bernard, J. Dhooge, and D. Friboulet. Statistics of the radio-frequency signal based on K distribution with application to echocardiographic images. *IEEE Transactions on Ultrasonics, Ferroelectrics, and Frequency Control*, 53:1689–1694, 2005.
- [44] O. Bernard, J. Dhooge, and D. Friboulet. Segmentation of echocardiographic images based on statistical modelling of the radio-frequency signal. In *Proceeding of the 14th European Conference on Signal and Image Processing*, 2006.
- [45] R. F. Wagner, S. W. Smith, J. M. Sandrik, and H. Lopez. Statistics of speckle in ultrasound B-scans. *IEEE Transactions on Ultrasonics, Ferroelectrics, and Frequency Control*, 30(3):156–163, 1983.
- [46] C. B. Burckhardt. Speckle in ultrasound B-mode scans. *IEEE Transactions on Ultrasonics, Ferroelectrics, and Frequency Control*, 25(1):1–6, 1978.
- [47] E. Jakeman. K-distributed noise. *Journal of the Optical Society of America*, 1:784–789, 1999.
- [48] M. F. Insana, R. F. Wagner, B. S. Garra, D. G. Brown, and T. H. Shawker. Analysis of ultrasound image texture via generalized Rician statistics. In *Proceeding of the International Conference on Speckle*, volume 25, pages 743–748, 1986.
- [49] V. Dutt and J. F. Greenleaf. Ultrasound echo envelope analysis using a homodyned K-distribution signal model. *Ultrasonic Imaging*, 16(4):265–287, 1994.
- [50] V. Dutt and J. F. Greenleaf. Speckle analysis using signal to noise ratios based on fractional order moments. *Ultrasonic Imaging*, 17(4):251–268, 1995.
- [51] P. M. Shankar. A general statistical model for ultrasonic backscattering from tissues. *IEEE Transactions on Ultrasonics, Ferroelectrics, and Frequency Control*, 47(3):727–736, May 2000.

- [52] O. Bernard, J. Dhooge, and D. Friboulet. Statistical modeling of the radio-frequency signal in echocardiographic images based on generalized gaussian distribution. In *Proceeding of the 3rd IEEE International Symposium on Biomedical Imaging*, pages 153–156, 2006.
- [53] P. M. Shankar, V. A. Dumane, T. George, C. W. Piccoli, J. M. Reid, F. Forsberg, and B. B. Goldberg. Classification of breast masses in ultrasonic B scans using Nakagami and K-distributions. *Physics in Medicine Biology*, 24(4-5):659–675, July 2003.
- [54] P. M. Shankar. Ultrasonic tissue characterization using a generalized nakagami model. *IEEE Transactions on Ultrasonics, Ferroelectrics, and Frequency Control*, 48(6):2229–2240, 2001.
- [55] B. Potocnik and D. Zazula. Automated analysis of a sequence of ovarian ultrasound images. *Journal of Image and Vision Computing*, 20:217–225, 2002.
- [56] A. Mishra, P. K. Dutta, and M. K. Ghosh. A GA based approach to boundary detection of left ventricle with echocardiographic image sequences. *Journal of Image and Vision Computing*, 21:967–976, 2003.
- [57] A. Achim and P. Bezerianos. Novel Bayesian multiscale method for speckle removal in medical ultrasound images. *IEEE Transactions on Medical Imaging*, 20(8):772–783, August 2001.
- [58] S. Gupta, R. C. Chauhan, and S. C. Sexana. Wavelet-based statistical approach for speckle reduction in medical ultrasound images. In *Proceeding of Midwest Biomedical Engineering Conference*, volume 42, pages 189–192, 2004.
- [59] J. K. Huat. *Restoration of medical pulse-echo ultrasound images*. PhD thesis, University of Cambridge, 2006.
- [60] D. Kaplan and M. Qinglin. On the statistical characteristics of log-compressed rayleigh signals: theoretical formulation and experimental results. In *Proceedings of IEEE Ultrasonics Symposium*, volume 2, pages 961–964, October 1993.

- [61] V. Dutt and J. F. Greenleaf. Statistics of the log-compressed echo envelope. *Journal of the Acoustical Society of America*, 99(6):3817–3825, June 1996.
- [62] D. Boukerroui, A. Baskurt, J. A. Noble, and O. Basset. Segmentation of ultrasound images - multiresolution 2-D and 3-D algorithm based on global and local statistics. *Pattern Recognition Letters*, 24(4-5):779–790, February 2003.
- [63] N. Paragios, M. P. Jolly, M. Taron, and R. Ramaraj. Active shape models and segmentation of the left ventricle in echocardiography. In *Proceeding of the International Conference on Scale Space Theories PDEs Methods and Computer Vision*, volume 3459, April 2005.
- [64] Z. Tao, C. C. Jaffe, and H. D. Tagare. Tunneling descent: A new algorithm for active contour segmentation of ultrasound images. In *Information Processing in Medical Imaging*, volume 2732, pages 246–257, 2003.
- [65] C. Baillard and C. Barillot. Robust 3-D segmentation of anatomical structures with level sets. *Lecture Notes in Computer Science*, 1935:236–245, 2000.
- [66] M. Mignotte, J. Meunier, and J. C. Tardif. Endocardial boundary estimation and tracking in echocardiographic images using deformable template and Markov random fields. *Pattern Anal. Appl.*, 4(4):256–271, 2001.
- [67] V. Hlavac, M. Sonka, and R. Boyle. *Image Processing: Analysis and Machine Vision*. Thomson Learning Vocational, September 1998.
- [68] S. D. Pathak, V. Chalana, D. R. Haynor, and Y. Kim. Edge-guided boundary delineation in prostate ultrasound images. *IEEE Transactions on Medical Imaging*, 19(12):1211–1219, December 2000.
- [69] K. D. Donohue, M. Rahmati, L. G. Hassebrook, and P. Gopalkrishnan. Parametric and nonparametric edge detection for speckle degraded images. *Optical Engineering*, 32(8):1935–1946, 1993.
- [70] R. N. Czerwinski, D. L. Jones, and W. D. O’Brien. Detection of lines and boundaries in speckle images – applications to medical ultrasound. *IEEE Transactions on Medical Imaging*, 18(2):126–136, February 1999.

- [71] Y. Chen, H. Tagare, S. Thiruvankadam, F. Huang, D. Wilson, K. S. Gopinath, R. W. Briggs, and E. A. Geiser. Using prior shapes in geometric active contours in a variational framework. *International Journal of Computer Vision*, 50(3):315–328, December 2002.
- [72] L. X. Gong, S. D. Pathak, D. R. Haynor, P. S. Cho, and Y. Kim. Parametric shape modeling using deformable superellipses for prostate segmentation. *IEEE Transactions on Medical Imaging*, 23(3):340–349, March 2004.
- [73] L. Tao, U. Castellani, A. Fusiello, and V. Murino. 3D acoustic image segmentation by a RANSAC-based approach. In *Proceedings of Oceans 2003 Marine Technology and Ocean Science Conference, San Diego, USA*, volume 2, pages 1098–1101, September 2003.
- [74] D. Shen, Y. Zhan, and C. Davatzikos. Segmentation of prostate boundaries from ultrasound images using statistical shape model. *IEEE Transactions on Medical Imaging*, 22(4):539–551, April 2003.
- [75] T. F. Cootes, C. J. Taylor, D. H. Cooper, and J. Graham. Active shape models – their training and application. *Computer Vision and Image Understanding*, 61(1):38–59, January 1995.
- [76] J. A. Noble and D. Boukerroui. Ultrasound image segmentation: a survey. *IEEE Transactions on Medical Imaging*, 25(8):987–1010, August 2006.
- [77] G. Jacob, J. A. Noble, C. Behrenbruch, A. D. Kelion, and A. P. Banning. A shape-space-based approach to tracking myocardial borders and quantifying regional left-ventricular function applied to echocardiography. *IEEE Transactions on Medical Imaging*, 21(3):226–238, March 2002.
- [78] M. Mulet-Parada and J. A. Noble. 2D + T acoustic boundary detection in echocardiography. *Medical Image Analysis*, 4(1):21–30, March 2000.
- [79] K. J. Draper, C. C. Blake, D. B. Gowman, L. nad Downey, and A. Fenster. An algorithm for automatic needle localization in ultrasound-guided breast biopsies. *Medical Physics*, 27:1971–1979, 2000.
- [80] P. M. Novotny, J. W. Cannon, and R. H. Howe. Tool localization in 3D ultrasound images. In *Proceedings of Medical Image Computing and Computer-Assisted Intervention*, volume 2879, pages 969–970, 2003.

- [81] M. Ding, H. N. Cardinal, W. Guan, and A. Fenster. Automatic needle segmentation in 3D ultrasound images. In *Proceedings of the SPIE*, volume 4681, pages 65–76, May 2002.
- [82] B. Lichtenbelt, R. Crane, and S. Naqvi. *Introduction to Volume Rendering*. Prentice Hall, March 1998.
- [83] M. Ding, H. N. Cardinal, and A. Fenster. Automatic needle segmentation in three-dimensional ultrasound images using two orthogonal two-dimensional image projections. *Medical Physics*, 30(2):222–234, February 2003.
- [84] M. Ding and A. Fenster. Projection-based needle segmentation in 3d ultrasound images. *Computer Aided Surgery*, 9(5):193–201, 2004.
- [85] M. Ding and A. Fenster. A real-time biopsy needle segmentation technique using hough transform. *Medical Physics*, 30(8):2222–2233, August 2003.
- [86] F. Solina and R. Bajcsy. Recovery of parametric models from range images: The case for superquadrics with global deformations. *IEEE Transactions on Pattern Analysis and Machine Intelligence*, 12(2):131–147, February 1990.
- [87] A. Leonardis, A. Jaklic, and F. Solina. Superquadrics for segmenting and modeling range data. *IEEE Transactions on Pattern Analysis and Machine Intelligence*, 19(11):1289–1295, November 1997.
- [88] E. Trucco and A. Verri. *Introductory Techniques for 3-D Computer Vision*. Prentice Hall, March 1998.
- [89] Martin Barva, Jean-Martial Mari, Jan Kybic, and Christian Cachard. Radial Radon transform for electrode localization in biological tissue. In Jiří Jan, Jiří Kozumplík, and Ivo Provazník, editors, *BIOSIGNAL: Analysis of Biomedical Signals and Images*, pages 299–301, Brno, Czech Republic, June 2004. EURASIP, VUTUM Press.
- [90] Martin Barva, Jan Kybic, Jean-Martial Mari, and Christian Cachard. Radial Radon transform dedicated to micro-object localization from radio frequency ultrasound signal. In Marjorie Passini Yuhas, editor, *Proceedings of IEEE Ultrasonics, Ferroelectrics and Frequency Control Symposium*, pages 1836–1839, New York, USA, August 2004. IEEE.

- [91] Martin Barva, Jan Kybic, Hervé Liebgott, Christian Cachard, and Václav Hlaváč. Comparison of methods for tool localization in biological tissue from 3D ultrasound data. In *Proceedings of IEEE Ultrasonics Symposium*, pages 1983–1986, October 2006.
- [92] F. Natterer. *The Mathematics of Computerized Tomography*. Society for Industrial and Applied Mathematics, classics in applied mathematics edition, 2001.
- [93] P. Toft. *The Radon Transform - Theory and Implementation*. PhD thesis, Technical University of Denmark, 1996.
- [94] S. Helgason. *The Radon Transform*. Birkhauser Boston, 2007.
- [95] E. Heitz, P. Perez, and P. Bouthemy. Multiscale minimization of global energy functions in some visual recovery problems. *Computer Vision Graphics and Image Processing*, 59(1):125–134, 1994.
- [96] R. Bulirsch and J. Stoer. *Introduction to Numerical Analysis*. Springer-Verlag, New York, 1991.
- [97] Martin Barva, Jan Kybic, Jean-Martial Mari, Christian Cachard, and Václav Hlaváč. Automatic localization of curvilinear object in 3D ultrasound images. In William F. Walker and Stanislav Y. Emelianov, editors, *Medical Imaging 2005: Ultrasonic Imaging and Signal Processing*, volume 6 of *Progress in Biomedical Optics and Imaging*, pages 455–462, Washington, USA, July 2005. SPIE.
- [98] Martin Barva, Jan Kybic, Jean-Martial Mari, Christian Cachard, and Václav Hlaváč. Localizing metal electrode from 3D ultrasound data using RANSAC and intensity priors. In Jiří Hozman and Peter Kneppo, editors, *IFMBE: Proceedings of the 3rd European Medical and Biological Engineering Conference - EMBEC*, volume 11, pages 1–6, Prague, Czech Republic, November 2005. IFMBE.
- [99] S. C. Choi and R. Wette. Maximum likelihood estimation of the parameters of the gamma distribution and their bias. *Technometrics*, 11(4):683–690, November 1969.

- [100] R. O. Duda, P. E. Hart, and D. G. Stork. *Pattern Classification*. Wiley-Interscience, 2000.
- [101] E. Parzen. On estimation of a probability density function and mode. *Annals of Mathematical Statistics*, 33(3):1065–1076, September 1962.
- [102] D. W. Scott. *Multivariate Density Estimation: Theory, Practice, and Visualization*. Wiley-Interscience, 2001.
- [103] B. W. Silverman. *Density Estimation for Statistics and Data Analysis*. Chapman and Hall/CRC, 1986.
- [104] O. Chum and J. Matas. Randomized RANSAC with T(d,d) test. In *Proceedings of the British Machine Vision Conference, Cardiff, UK*, pages 448–457, 2002.
- [105] J. A. Nelder and R. Mead. A simplex method for function minimization. *The Computer Journal*, 7:308–313, 1965.
- [106] D. Freedman and P. Diaconis. On the histogram as a density estimator: l_2 theory. *Probability Theory and Related Fields*, 57(4):453–476, December 1981.
- [107] L. Devroye. *Non-Uniform Random Variate Generation*. Springer, July 1986.
- [108] J. C. Martín. Statistique du signal RF: comparaison entre simulations et mesures expérimentales. Master’s thesis, INSA de Lyon, Lyon, France, March 2007.
- [109] K. J. M. Surry, H. J. B. Austin, A. Fenster, and T. M. Peters. Polyvinyl alcohol cryogel phantoms for use in ultrasound and MR imaging. *Physics in Medicine and Biology*, 49(24):5529–5546, 2004.

TITRE: Localisation des outils chirurgicaux dans des images échographiques 3D.

RÉSUMÉ: On propose des approches robustes pour trouver la position d'un objet de la forme d'électrode dans une image échographique 3D. Son axe est estimé par la maximisation de la projection parallèle que l'on décrit par une transformée de la Projection Intégrale Parallèle. La maximisation est accélérée par une approche multi-échelle, hiérarchique. Deuxième algorithme basé sur le recalage de modèle identifie une électrode courbée. Trois modèles différents décrivent sa forme et la densité d'intensité. Ses paramètres sont établis par R-RANSAC. La position estimée est optimisée par la méthode simplex. L'extrémité de l'électrode est trouvée des intensités le long de l'axe. Des images échographiques 3D ont été simulées afin de déterminer la précision sous des conditions différentes. Les méthodes ont été testées sur des images réelles 3D d'un fantôme comprenant une électrode. Les résultats montrent une précision de 0.2 mm. Le temps de calcul en secondes permet une localisation rapide.

TITLE: Localization of surgical instruments in 3D ultrasound images.

ABSTRACT: Robust methods are proposed to determine the position of an electrode-like object in a 3D ultrasound image. The axis is found by maximizing the parallel projection described by a Parallel Integral Projection transform. The maximization is accelerated by a hierarchical mesh-grid method. A second algorithm, based on the model fitting paradigm is introduced to identify a curved electrode. Three distinct models are suggested to describe its shape and intensity distribution. Their parameters are estimated by the R-RANSAC algorithm. The axis estimate is optimized using the simplex method. The electrode tip is found from the intensity along the axis. 3D ultrasound images were simulated to assess the localization accuracy under various conditions. The algorithms were also verified on real 3D ultrasound images of a cryogel phantom containing a thin metallic electrode. The experiments show an accuracy of 0.2 mm. The processing time in seconds permits fast electrode localization.

DISCIPLINE: Acoustic, signal and image processing.

KEYWORDS: ultrasound, image, 3D, volume, localization, segmentation, electrode, needle, projection, RANSAC.

LABORATORIES: CREATIS, CNRS UMR 5515, INSERM U630; Bâtiment Blaise Pascal, 7 Avenue Jean Capelle, 69621 Villeurbanne CEDEX, France. **Center for Machine Perception**, Department of Cybernetics, Faculty of Electrical Engineering, Czech Technical University in Prague; Karlovo náměstí 13, 121 35 Prague 2, Czech Republic.